Realisation and Optimisation of Novel Topological Materials

Joshua Gretton

University of Leeds

School of Physics and Astronomy

Submitted in accordance with the requirements for the degree of

Doctor of Philosophy

August, 2022

Intellectual Property Statement

The candidate confirms that the work submitted is his own and that appropriate credit has been given where reference has been made to the work of others.

Acknowledgements

Many people have helped this thesis come together, offering a total combination of many talents and qualities that I can only aspire too.

First, Satoshi Sasaki is who I have much of my scientific development to thank for. His expertise and knowledge have been invaluable, helping to develop my own knowledge, understanding and approach, whilst offering a fine balance of patience and encouragement.

Mannan Ali has aided most of my experimental endeavours, particularly the growth of thin film superconductors, helping troubleshoot many cryogenic road-blocks, and more generally encouraging me to wake up earlier and walk to work more often.

Gavin Burnell has given numerous suggestions for smarter experimental work, also helping develop my work in most of my formal assessments. Chris Marrows has been the principal panel member in all of my annual review meetings, offering wisdom and guidance over the course of this project.

Truly all of the academics in the CM group have contributed: all of the questions, comments, and explanations are greatly appreciated.

A particular thank you to Bryan Hickey and Geetha Balakrishnan. They ensured a supportive environment for me to defend this work in, and their comments have undoubtedly lead to a more coherent thesis and confident student.

David Chapman and Adam Foster have skilfully negotiated my ever increasing demands for cryogenics, and thank you to everyone in the mechanical and electronic workshops for various building and repair jobs.

I am deeply grateful for the friends I have made during this project. Thank you for all of the help in and out of the labs, training on equipment, hallway chats, pub visits, squash games, pool games, Christmas parties, and overall the many benefits of being surrounded by such a bright and hard-working group.

A special thank you to my friends and family in Scarborough, Leeds, Pulborough, and beyond. In particular my grandparents, sister, and parents, whose support has propelled me from the beginning.

Finally, thanks to Francesca, for all the encouragement and support, and for somehow managing to stop me thinking about physics all the time.

Abstract

This thesis details work in two topological materials, with the overall aim of producing candidates for the next generations of computational technologies.

Sb_2Te_3 single crystals have been grown with p-type carrier densities in the range 2 - 12 $\times 10^{19}$ cm^{-3} using a modified Bridgman method with excess Te in the melt. Magnetotransport up to 8 T reveals a non-linear Hall resistivity with field and a saturating magnetoresistance in the high-field limit across the carrier density range, which are both explained by a semi-metallic two carrier band model with a majority hole and minority electron band. Shubnikov de Haas Oscillations are observed below 30 K for all samples and a carrier-density dependent beating envelope caused by the convolution of multiple frequencies is found for reduced carrier density samples. Fitting the oscillations directly, non-trivial Berry phases are extracted for each Fermi branch for carrier densities in the range 4.1 - 7.9 $\times$ 10^{19} cm^{-3}. Rather than originating from non-trivial Rashba or Dirac surface states, linearly dispersive bulk states are found to be responsible for the beating and non-trivial Berry phase. Overall a carrier density range required for observing the Rashba surface states in thin samples is confirmed.

$RhPb_2$ thin films have been grown using a DC sputtering and annealing procedure, where films annealed at 450°C for 24 hours show a clear superconducting onset close to 1.4 K, though a complete transition to a zero resistance state is not observed down to 380 mK. The emergence of superconductivity shows an acute sensitivity to the annealing conditions: T_c is suppressed with higher annealing temperatures, and annealing in a ultra high vacuum environment gives an increase in the total reduction of resistance by 380 mK. Despite this, the upper critical field dependence on temperature is well described by the conventional WHH theory for dirty spin-singlet superconductors, and a positive correlation of T_c with increasing amounts of structural disorder suggest a spin-singlet superconducting state. These changes in T_c are found to be related to a reduction of the electron-phonon coupling strength, characterised by analysis of the normal state resistivity dependence on temperature.

Contents

List of Figures

List of Tables

Abbreviations

2DEG	2 Dimensional Electron Gas	ABS	Andreev Bound States
AC	Alternating Current	BCS	Bardeen-Cooper-Schrieffer
BdG	Bougouliobov-de Gennes	BG	Bloch-Gruneisen
BSTS	$(Bi_{1-x}Sb_x)_2(Se_{1-y}Te_y)_3$	BVB	Bulk Valence Band
CSA	Cross Sectional Area	DC	Direct Current
DoS	Density of States	DSM	Dirac Semimetal
FET	Field Effect Transistor	FFT	Fast Fourier Transforms
FWHM	Full Width at Half Maximum	GL	Ginzburg Landau
LK	Lifshitz-Kosevich	MJZM	Majorana Zero Mode
MR	Magnetoresistance	PHS	Particle Hole Symmetry
PSU	Power Supply Unit	RRR	Residual Resistance Ratio
SdHO	Shubnikov-de Haas Oscillations	SOC	Spin Orbit Coupling
(SR)-ARPES	(Spin Resolved) Angle Resolved Photo-Emission Spectroscopy	SLD	Scattering Length Density
TI	Topological Insulator	TSM	Topological Semimetal
TRIM	Time Reversal Invariant Momentum	TRP	Time Reversal Polarisation
TRS	Time Reversal Symmetry	TSC	Topological Superconductor
UHV	Ultra-High Vacuum	VdP	Van der Pauw
VdW	Van der Waals	VTI	Variable Temperature Insert
WAL	Weak Anti-Localisation	WHH	Werthamer, Helfand and Hohenberg
WSM	Weyl Semimetal	XRD	X-Ray Diffraction
XRR	X-Ray Reflectivity	ZBCP	Zero Bias Conductance Peak

Common Symbols

B	Applied Magnetic Field ($\mu_0 H$)	Δ	Superconducting Gap Parameter
E_F	Fermi Energy	e	Elementary Charge
ϵ_0	Permittivity of Free Space	F	Frequency
Γ	Bulk Time Reversal Invariant Momentum Point	h	Planck's Constant
$\hbar$	$h/2\pi$	$\hat{H}$	Hamiltonian
I_c	Critical Current	I	Current
$\boldsymbol{k}$	Wavevector	k_F	Fermi Wavevector
k_B	Boltzmann Constant	λ_{BG}	Bloch-Gruneisen Electron Phonon Coupling Parameter
λ_{McM}	McMillan Electron Phonon Coupling Parameter	λ_L	London Penetration Depth
λ	Effective Penetration Depth	Λ	Surface Time Reversal Invariant Momentum Point
l	Mean Free Path	m^*	Effective Mass
m_c	Cyclotron Effective Mass	m_D	Density of States Effective Mass
m_0	Electron Rest Mass	μ	Carrier Mobility
μ^*	Renormalised Coulomb Potential Parameter	n	Carrier Density (electrons)
$(\nu_0;\, \nu_1\nu_2\nu_3)$	$Z2$ Invariants	ω_c	Cyclotron Frequency
ω_p	Drude Plasma Frequency	p	Carrier Density (holes)
ρ	Resistivity	ρ_0	Residual Resistivity
R_H	Hall Coefficient	σ	Conductivity
S	Maximal Fermi Surface Cross Sectional Area	T	Temperature
T_c	Critical Temperature	T_F	Fermi Temperature
Θ_D	Debye Temperature	v_F	Fermi Velocity
ξ_0	BCS Coherence Length	ξ	Effective Coherence Length

Chapter 1

Introduction

In the last few decades a new paradigm in condensed matter physics has surged, one focussing on the classification of materials based on the topology of the electronic state. Principally, topology is a field of mathematics that considers the classification of systems based on some invariant property or feature, one that is unchanged under smooth, continuous deformation, and which therefore separates systems into classes which share the same topological invariant. A popular example is that of the mug and the doughnut, shown in Figure 1.1, where the hole in both acts as a topological invariant, sorting them into the same topological class where the shapes could be smoothly connected to one another.

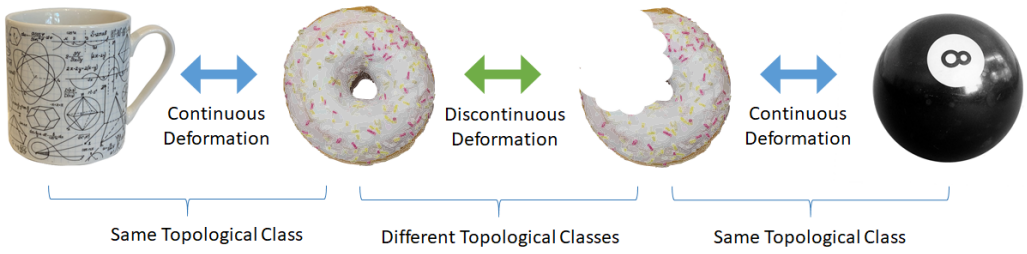

Figure 1.1: Schematic representation of topological classifications. The hole in the mug and the doughnut acts as a topological invariant, meaning it is preserved under continuous deformation and sorts these objects into the same topological class. A discontinuous deformation changes the number of topological invariants in this example, changing the topological class of the object.

The definition of topological matter most generally means any material system whose electronic state has a non-trivial topological index associated with it, which separates it from the topologically trivial limit of an atomic insulator. In 3D crystalline materials, these topological indices are intimately linked to the underlying symmetries of the electronic state, and the detailed topological classification of materials has been subject to much research [1, 2]. From this, Topological Insulators (TIs), Topological Semimetals (TSMs), and Topological Superconductors (TSCs) have all emerged as novel phases of matter, where Hamiltonians describing the electronic states of systems in the same classes may be smoothly connected to one another without the need to, for example in Figure 1.2 for a TI, reverse non-trivial band orderings, an analogous process to the bite in Figure 1.1. These material classes present novel physics to explore as the physical manifestation of topological phases, and are highly sought-after based

on proposed functionalities arising from the properties they possess as a result of the underlying non-trivial topology of the electronic state.

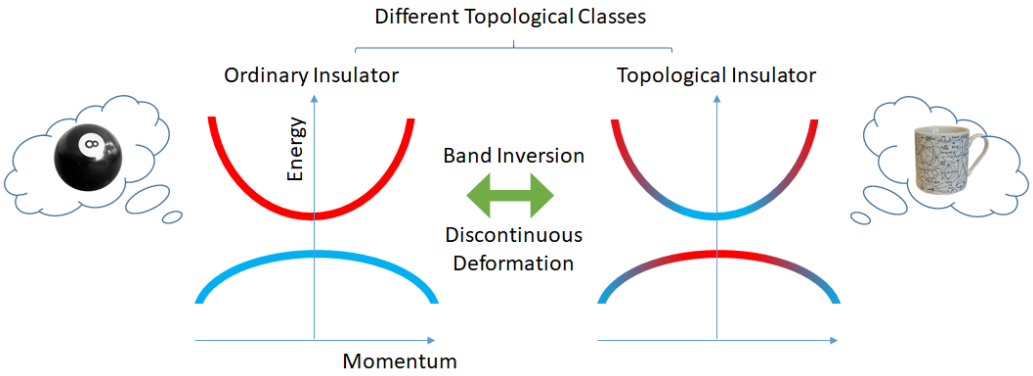

Figure 1.2: Schematic representation of the discontinuous deformation, or band inversion, that sorts ordinary and topological insulators into different topological classes which are no longer represented by a topologically equivalent Hamiltonian.

The key emergent property of these systems is the requirement to have a topologically protected surface state with a peculiar energy band structure, with bands that are enforced to be degenerate at high-symmetry points in the Brillouin zone. This requirement is intimately linked to the topological properties and underlying symmetries of the bulk crystal: the peculiar form of the surface states only arises due to the non-trivial topology of the bulk, so is called the bulk-boundary correspondence, and the degeneracies are enforced by symmetry constraints that define the topological protection. This is often visualised as the unwinding of the bulk non-trivial topology at the boundary with a topologically trivial phase, shown in Figure 1.3. The surface states are described as topologically protected, since they should remain stable as long as the underlying topological properties are preserved meaning these features are robust against certain perturbations. The interest in many topological materials is related to the properties of these surface states.

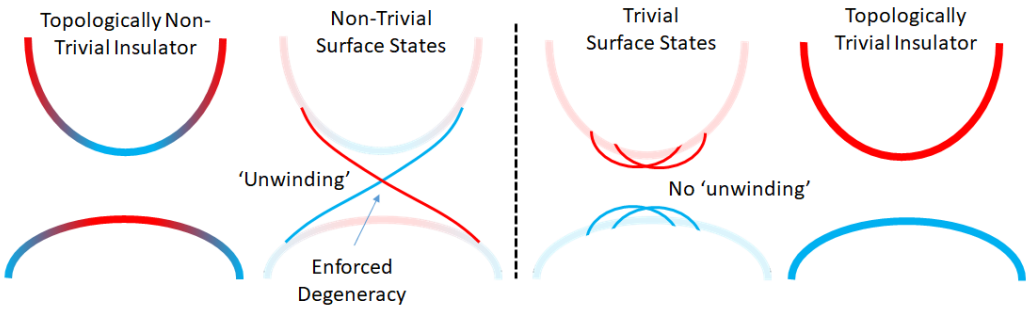

Figure 1.3: Schematic representation of the emergence of peculiar topologically protected surface states from the unwinding of the non-trivial bulk topology, with the contrasting case shown for a topologically trivial material with ordinary surface states.

For example, 3D strong TIs whose electronic states obey time reversal symmetry (TRS) an inversion symmetry (IS) present a single, linearly dispersive gapless Dirac cone on each surface, where an underlying strong spin-orbit coupling interaction leads to a spin-momentum locked structure, and overall a protected metallic surface state on an ideally insulating bulk [3, 4]. In an analogous fashion, 3D TSCs obeying TRS and IS present exotic linearly dispersive Majorana zero-modes [5–7], where both of these surface states are enforced to be degenerate at special points in the Brillouin Zone by the underlying TRS. The key here is that symmetry-obeying perturbations to the electronic states that would generally lift any accidental degeneracies of surface electronic states in topologically trivial materials, would not lift the degeneracy of the electronic states in a topological non-trivial material: the gapless nature of the surface states is protected by an underlying symmetry, in this case TRS, meaning the surface states and their intriguing properties are generally robust against non-magnetic disorder.

These systems are seeing a surge of interest due to both the novel underlying physics and the possible technological applications, where the overall intent is to produce devices capable of utilising the unusual surface states and mark an improvement from current technologies. In part, this is motivated by seeking advancements in the energy efficiency of conventional logic-circuit devices, where the spin-momentum locking in 3D TIs leads to ballistic spin-polarised charge transport to form the basis of low-power, high-frequency, spin-based field effect transistors (FETs) [8–10]. On the other hand, the Majorana-zero modes found on the surfaces of TSCs may facilitate the implementation of topologically protected quantum computation, providing an avenue for quantum op-

erations with a natural resilience to de-coherence effects, unlocking the next-generation of computational power and the ability to tackle problems beyond the capabilities of classical computers [11, 12].

Of course, these high-level goals rely on detailed experimental work to produce continual improvements in materials and systems design, which is important on two fronts: clearly uncovering the features of these materials related to the non-trivial topology, and for tuning the basic properties of the systems to maximise the efficiency of any technological implementation. The main motivation for this thesis then is to identify and experimentally realise novel topological materials that should lead to improvements in functionality compared to current examples of topological materials.

1.1 Proposed Investigation for Topological Insulators

Some of the fundamental problems surrounding 3D TIs and their implementation in spin-FETs is related to bulk conduction channels that short circuit the surface state transport: this is typically countered by alloying between similar material end-members and by reducing the physical dimensions of the samples to use, which has lead to the successful detection of spin-polarised transport in many 3D TI materials [13–15]. Another part of the functionality in devices is related to the ability to switch the direction of the spin-polarisation by electrostatic tuning of the chemical potential position, this sign change requires the existence of a second set of surface bands with a Rashba spin structure, that so far have been achieved by 'accidental' surface doping [16].

To this end, Sb_2Te_3 has been identified as a strong materials candidate for future application. It is a 3D TI with a single Dirac cone on the hexagonal (001) cleavage surface that is well separated from the bulk band structure [4]. It presents the highest surface charge carrier mobility (2.5×10^4 cm^2/Vs) of any 3D TI found to date with successful depletion of bulk transport channels in thin samples [17], lending itself to spin-dependent device applications on account of the long ballistic transport regime. It also possesses an *intrinsic* set of Rashba surface bands pending full electronic characterisation [18–21], which should presumably lead to greater control over the degree of spin-polarisation compared to states arising from surface doping.

As it stands there are some significant barriers before being able to seek applications of Sb_2Te_3. Primarily, only one example of surface dominant transport with such high mobility exists [17], and confirmation of whether the Rashba surface states can also

contribute significantly to the surface transport alongside the Dirac surface state, and so affect the degree of spin-polarisation switching, is also required.

The aim of this work is to first investigate whether the bulk carrier density of Sb_2Te_3 can be reduced as far as reported previously utilising a modified Bridgman method to produce high-quality single crystals, which should later allow for ex-foliation and further adaptation into device architectures [10, 16]. By tuning the growth stoichiometry, the overall goal is to produce low bulk carrier density, high surface carrier mobility samples where contributions to the transport are identified from the Dirac and Rashba surface states. After this, further work in the system would include the ex-foliation of very thin samples, which would in turn lead to higher surface state contribution and easier identification of the surface contributions, and then also allow for electrostatic gating and nano-pattern device fabrication to illuminate and control the spin-polarised transport behaviour.

1.2 Proposed Investigation for Topological Superconductors

So far, many of the examples of TSCs are based on TIs with induced superconductivity. The first experimental evidence for TSCs came from Cu-intercalated Bi_2Se_3 and In-doped SnTe, where the superconductivity is an emergent property of the doped material [22, 23]. The requirement for doping presents significant challenges in the preparation of samples that are definitely and reproducibly TSCs [23].

In other cases, the superconducting proximity effect has been used to induce superconductivity in the topological surface states [24], leading to the emergence of protected Majorana modes at, for example, the ends of 1D nano-wires [25], or within the constricted regimes of planar Josephson Junctions [26–28].

Recently, there has been a surge of interest in the topological properties of already superconducting compounds [29–31]. Ultimately, the emergence of intrinsically topologically non-trivial superconductivity in a material that requires no doping or additional processing may ultimately lead to easier implementation in devices.

In line with this, the second material identified as a promising candidate for study in this thesis is the intrinsically superconducting 3D Dirac semi-metal $RhPb_2$ [32–39]. The material holds the pre-requisite ingredients for a TSC phase, and the intrinsic

superconductivity and Dirac nature will in any case lead to protected surface Majorana modes to be identified [40]. A novel structural polymorph of $RhPb_2$ is also predicted to have one of the highest superconducting critical temperatures found in a topologically non-trivial material so far, close to 10 K [30].

So far there is minimal characterisation of $RhPb_2$ in the literature: only the values of T_c are quoted in studies from 50 years ago [38, 39], and only recently has the material been re-synthesized for re-determination of the structural parameters [41].

Considering this, the proposed investigation of this material system here has the primary key objectives: synthesize the base compound $RhPb_2$ and characterise the basic properties of the system, including confirming the presence of Dirac semi-metal behaviour and characterising the emergent superconductivity in more detail, searching for any signatures of unconventional TSC behaviour. After this, seeking experimental verification of the proposed structural polymorph is highly desirable to further explore the possibility of topological superconductivity in this material system.

Since thin-film TSCs may be more desirable for future implementation of Josephson Junction devices and this material cannot be easily exfoliated into thin samples from bulk, DC sputtering is targeted as the first synthesis method, since many of the well-established nano-fabrication techniques can be utilised after thin-films showing the desired properties are obtained.

1.3 Order of this Thesis

Chapter 2 first reviews some of the key theoretical ideas underlying Topological Insulators and Superconductors, focussing on the physical mechanisms related to the emergence of the topologically non-trivial states. The surface states of these materials are discussed, and the key experimental signatures used to identify the states of interest are reviewed.

Chapter 3 introduces the experimental methods used in this thesis, highlighting some of the physical concepts relevant to these and detailing the apparatus used. Details of the electronic measurement techniques are considered to ensure accurate determination of the properties of superconducting films, and the magnetotransport effects observed in this thesis are introduced and discussed to provide more context to the fitting and extraction of material parameters applied later.

Chapter 4 presents a study of the material system Sb_2Te_3, detailing an investigation

into reducing the bulk transport contributions in attempts to uncover signatures from the Dirac and Rashba surface states of interest. Varying amounts of excess Te are used to grow single crystals covering an order of magnitude range of carrier densities. This allows a detailed investigation of the electronic properties of the system.

Chapter 5 presents a study of the material system $RhPb_2$, reporting the first successful observation of superconductivity in textured thin-films of this material. From this, the superconducting properties of the system grown in thin-film form are characterised, and the observed properties are probed for signatures of unconventional behaviour.

Finally, Chapter 6 reports the main conclusions of this work.

Chapter 2

Background Theory and Review

This chapter explores some of the underlying physical mechanisms responsible for the emergence of non-trivial Topological Insulators and Superconductors, and introduces the non-trivial surface states. The key physical features that can be observed in experiments are also reviewed.

2.1 3D Topological Insulators

Topological Insulators still posses a conduction band, a valence band and a band gap in the bulk: they are however distinct from trivial insulators as they have non-trivial topological indices that characterise the bulk electronic state. This non-trivial bulk topology generally arises due to changes in the electronic structure of the material, specifically a reversal in the ordering of some of the bulk energy bands relative to a topologically trivial material. The non-trivial topology requires the existence of an odd number of topologically protected gapless surface states, which in the cases of 3D TIs with strong spin-orbit coupling (SOC) obeying TRS and IS are 2D Dirac cones with a spin-momentum locked structure.

2.1.1 Z2 Topology and Band Inversion Mechanism

The topological invariants defined for a 3D TI obeying TRS are called the $Z2$ invariants, which are defined based on the properties of the Bloch Hamiltonians describing the electron wave-functions in a periodic crystal lattice. The invariants are $(\nu_0;\ \nu_1\nu_2\nu_3)$, where $\nu_0 = 0$ or 1 defines the trivial or strong non-trivial topology respectively [42, 43]. The remaining $\nu_1\nu_2\nu_3$ are the weak topological indices, which are so called because they depend on lattice translation symmetry and so break down in the presence of disorder. The $Z2$ invariants reflect how a quantity called the time reversal polarization (TRP) changes when an electron completes a Fermi arc between special Time Reversal Invariant Momentum (TRIM) points in the Brillouin zone.

In any spin-1/2 system obeying TRS, the energy eigenstates must be doubly degenerate: an eigenstate with spin-up and momentum $\boldsymbol{k}$ has an equal energy time-reversed partner with spin-down at $-\boldsymbol{k}$, this property is called the Kramer's degeneracy [42–44].

For electrons in a crystal the energy bands therefore exist in Kramer's pairs, where $E(\boldsymbol{k}) = E(-\boldsymbol{k})$, shown schematically in Figure 2.1a. At special points of the Brillouin Zone, those defined by exactly the reciprocal lattice vectors, $\boldsymbol{k} = -\boldsymbol{k}$ due to the trans-

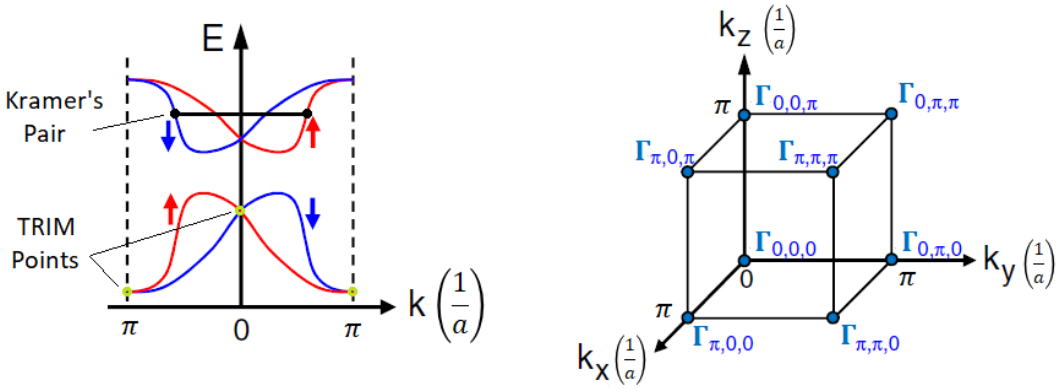

Figure 2.1: (a) Schematic of Kramer's energy band pairs and enforced band degeneracy at the TRIM points $\boldsymbol{k} = 0, \frac{\pi}{a}$ [44]. (b) The TRIM points of a 3D Cubic Brillouin Zone [44]. The $Z2$ invariant characterises how properties related to the TRS of a system change between these TRIM points.

lation symmetry of the lattice and the time-reversed Kramer's partners are degenerate at the same crystal momentum [44]. These points are called TRIM points, and the energy band degeneracy remains intact at these points as long as TRS is obeyed. The TRIM are highlighted in Figure 2.1a at $\boldsymbol{k} = 0, \frac{\pi}{a}$, and shown for a cubic Brillouin Zone with lattice constant a in Figure 2.1b labelled Γ_i.

The ν_0 $Z2$ invariant in inversion symmetric systems is defined by the relation [42, 43]:

$$(-1)^{\nu_0} = \prod_i \delta_i \tag{2.1}$$

$$\delta_i = \prod_{m=1}^{N} \xi_{2m}\left(\Gamma_i\right) \tag{2.2}$$

Here $\xi_{2m}\left(\Gamma_i\right)$ is the parity eigenvalue of the $2m$-th occupied band at the TRIM point Γ_i, which shares a parity eigenvalue with the Kramer's partner $\xi_{2m-1}\left(\Gamma_i\right)$.

Parity defines whether the wave-function is unchanged (even-parity or symmetric) or reverses sign (odd-parity or anti-symmetric) under spatial inversion, with the parity operator giving eigenvalues ± 1 for even and odd wave-functions respectively. The term δ_i then is the product of the band-parity eigenvalues over $2N$ occupied bands ($\delta_i = \pm 1$) assessed at the i-th TRIM point Γ_i, and the term $\prod_i \delta_i$ is the product of this value

from all the TRIM points present in the Brillouin zone ($\prod_i \delta_i = \pm 1$).

In short, the ν_0 $Z2$ invariant becomes non-trivial if the value $\prod_i \delta_i = -1$. For atomic orbitals the parity eigenvalue is $(-1)^l$ where l is the orbital angular momentum quantum number [45]. The parity eigenvalues for hybridized bands in materials are known from band-structure theory [42, 43]. This allows for simple assessment of the terms above and identification of an overall odd parity product and non-trivial $Z2$ invariant.

The approach for identifying TIs comes directly from this definition by identifying the presence of a band inversion between the upper most occupied band and a lowest unoccupied band with opposite parity eigenvalue, around an odd number of TRIM points, shown schematically in Figure 2.2. First, inversions between occupied bands produce no change in the overall parity product $\prod_i \delta_i$. With an even parity product in conventional insulators at all the TRIM points, the inversion of the parity of the uppermost occupied band at an *odd* number of TRIM points will lead to an overall negative product of the parity eigenvalues, therefore giving a $\nu_0 = 1$ topological insulator.

Such band inversions between the highest occupied and unoccupied energy levels in materials are visualised by following the evolution of the orbital energy levels of a single atomic element as it undergoes the effects of chemical bonding into a crystal structure, which are then shifted in energy by the presence of any spin-orbit interaction [4]. Typically, the crucial point of inversion is brought about by this strong spin-orbit coupling interaction, naturally leading to the identification of TIs in heavy-element (high-Z) semi-conductors with narrow band gaps, which in the ideal case would be insulating at low temperature [4, 44].

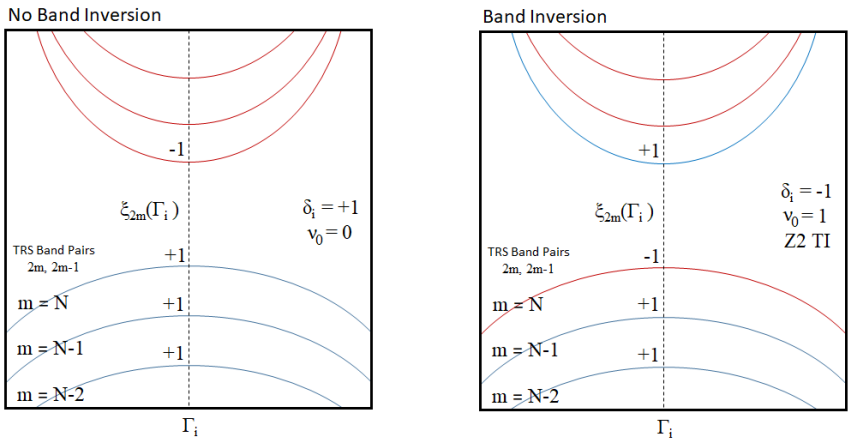

Figure 2.2: Schematic representation of: (a) non-inverted band structure and topologically trivial material. (b) The bulk band inversion mechanism producing a 3D TI. Often strong spin orbit coupling interactions lead to a orbital dependent shift in the energy levels, producing a band inversion. If such band inversions occur between orbitals with opposite spatial parity at an odd number of TRIM points, the band inverted compound will be a strong $Z2$ TI.

2.1.2 Surface States of 3D Topological Insulators

At the boundary of *any* crystal the periodic potential of the lattice is terminated, which leads to the emergence of discrete energy levels within the energy gap of the crystal [46]. The amplitude of the wave-functions describing these states is damped exponentially moving further outside or inside the crystal, meaning they are localised to the crystal surface and so are called surface states [46]. Thus, there is a spectrum of electronic states in between the conduction and valence bands of the bulk, which may only be occupied by electrons on the surface [46].

Figure 2.3a shows an example of such generic surface states residing in the band gap of a topologically trivial material. In this case, generally expected for a trivial semi-conductor, there are regions where the chemical potential would still reside in a complete band gap, one where the surface states are not partially occupied, and the surface remains insulating.

The physical implication of a $\nu_0 = 1$ topological insulator is that the surface band

energy spectrum takes a different form, shown schematically in Figure 2.3b, where there is no longer any region where the chemical potential could reside in a complete band gap to give insulating behaviour. This form of the surface state is generally referred to as metallic, or gapless, and conduction is expected from the surface states for any chemical potential in the band gap. This gapless nature is enforced by the underlying Kramer's degeneracy.

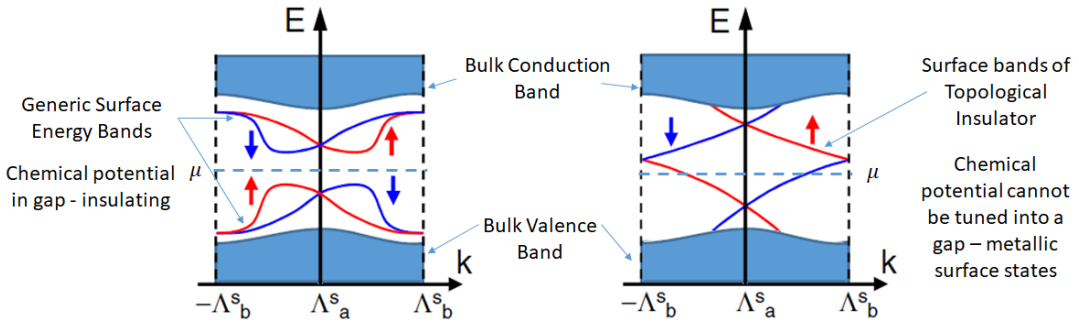

(a) (b)

Figure 2.3: Schematic representation, adapted from [44], of the difference in the surface band dispersion between (a) a trivial insulator with generic surface bands residing in the gap and (b) a non-trivial insulator with topologically protected surface bands. In (a), there are regions where completely insulating behaviour could be found. In (b), there is no region within the band gap where the surface states will not be partially occupied.

Formally, the $\nu_0 = 1$ $Z2$ invariant represents that there must be a change in the TRP between the surface TRIM points, the projection of the bulk TRIM onto the surface, labelled Λ_a and Λ_b in Figure 2.3. Physically this is represented by any surface energy band 'switching partner' at the TRIM points Λ_a and Λ_b. For the trivial $\nu_0 = 0$ case there is no change in TRP and this is physically represented by the surface energy bands not switching partner.

The key distinction is that a trivial insulator may have surface states residing in the bulk band gap, however there can still be fully gapped regions of energy between the surface bands and changes to the Hamiltonian may shift the energy bands out of the gap completely [44]. It is also likely that two surface bands are intersected for

any coincidental intersection between Λ_a and Λ_b. For the non-trivial case, a chemical potential in the bulk band gap is guaranteed to intersect only *one* surface band between Λ_a and Λ_b given the structure in Figure 2.3. Further, generic shifts to the energies of the bands will not change this consequence: a single band is guaranteed to be intersected.

This summarises the physical consequence of a non-trivial $Z2$ invariant: $\nu_0 = 1$ guarantees that a chemical potential in the band gap will always intersect a surface band, and that only one surface band is intersected.

In general, the details of the surface state electronic spectrum depend on the form of the Hamiltonian near to the surface of the material [42]. Ultimately the surface states are derived from solutions to the bulk Hamiltonian when the periodic potential of the lattice breaks down [47]. In practice, the form of the surface state can be determined by the projection of the bulk Hamiltonian onto surface subspaces [4].

The key relevant modification to the bulk Hamiltonian in the high-Z materials showing the TI phase arises from a strong SOC interaction. Including the relativistic SOC terms in the Hamiltonian leads to being able to represent the electronic states of the crystal by a form of the relativistic Dirac Hamiltonian, where the energy disperses linearly with momentum [4, 5, 48, 49]. On the surface then, the projection of this Hamiltonian leads to a Dirac-like form of the surface state [3, 4], which coupled with the strong non-trivial topological $Z2$ index leads to the emergence of a single linearly dispersive Dirac cone on the surface that is enforced to extend across the band-gap and be gapless at the surface TRIM points.

Since there is an enforced degeneracy at the TRIM point due to the TRS, this surface state in a TI is defined as a gapless Dirac cone, which is enforced to be gapless as long as TRS and underlying $Z2$ topology is preserved. These gapless Dirac cones have a linear dispersion relation: $E = \hbar k v_F$, which is equivalent to the electrons being described by the *massless* Dirac equation, or that with rest mass set to zero, leading to them being called massless Dirac fermions [44, 50]. The opening of a band gap in the Dirac spectrum when the topological protection is broken leads to a gap in the Dirac cone, and the electrons are then instead described by a massive form of the Dirac equation.[44]

Importantly, the actual *effective* mass of the charge carriers would diverge for the common $m^* = \left(\frac{\partial^2 E}{\partial k^2}\right)^{-1}$ form. In fact, this form is only valid for parabolic band dispersions, and instead the more general form, valid for any dispersion, is given by

$m^* = \frac{p}{v_g} = \hbar k^2 \left(\frac{\partial E}{\partial k}\right)^{-1}$ with momentum p and group velocity v_g [51]. The cyclotron mass is given by $m_c = \frac{\hbar^2}{2\pi}\left[\frac{\partial A(E)}{\partial E}\right]_{E=E_F}$ where $A(E)$ is the cyclotron orbit area in k-space [47, 50, 51], and is equivalent to the general form for an isotropic Fermi surface [51], and overall the effective/cyclotron mass of a Dirac fermion is given by: $m_c = \frac{\hbar k}{v_F}$ [50, 51].

Another important consequence of the strong SOC interaction is the emergence of spin-momentum locking in the surface band structure. As a relativistic correction to the Schrödinger Hamiltonian the spin-orbit interaction Hamiltonian is given by: $\hat{H}_{SOC} = \frac{\hbar}{4mc^2}(\nabla V \times \overrightarrow{p}) \cdot \overrightarrow{\sigma}$, where ∇V is the gradient of the electrostatic potential, $\overrightarrow{p}$ is the particle momentum, and $\overrightarrow{\sigma}$ is the Pauli spin operator [52].

On the surface of an inversion symmetric crystal, this is modified due to the dominant out-of-plane electric potential gradient from the planar surface termination. For out-of-plane ∇V and in-plane crystal momentum $\hbar\overrightarrow{k}$, the cross-product leads to an in-plane spin-direction perpendicular to the momentum [52]. This is encapsulated by a Rashba-like spin-orbit term: $\hat{H}_{SOC} = v\sigma_z(k_x s_y - k_y s_x)$, where v is the velocity, s is the Pauli matrix in spin space, and $\sigma_z = \pm 1$ now defines an orbital component usually leading to an opposite spin-helicity for each surface band arising from a single bulk band with double spin degeneracy [5, 23, 53].

The $\nu_0 = 1$ topological property of the bulk dictates the partner switching nature of the surface state, and the two values of σ_z now describe a switching of the spin-helicity above and below the band crossing at the surface TRIM point. The surface state is then referred to as a 2D topologically protected helical Dirac cone, shown in Figure 2.4, and the surface TRIM is referred to as a Dirac point.

Another facet of the non-trivial topology is that an electron within a surface Dirac cone has a non-trivial π Berry phase. In surface bands this is physically apparent from the spin-structure of the Dirac cone: a spin-1/2 electron completing a orbit in momentum space around the Dirac cone must have a 2π spin rotation, leading to the accumulation of geometric Berry phase factor of π [42–44]. Formally however, the non-trivial Berry phase arises due to the linearly dispersive nature of the bands [54–56], and a non-trivial phase may also appear from linearly dispersive 3D Dirac bulk bands [54, 57].

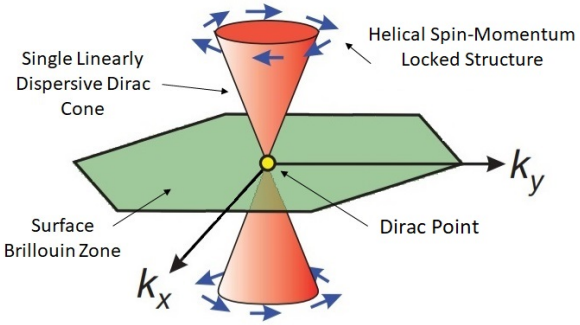

Figure 2.4: Schematic representation of 2D Dirac cone band structure, with energy projected vertically [44]. The Dirac nature results from strong spin-orbit coupling, the degeneracy at the TRIM point is enforced by TRS. The non-trivial topology enforces an odd number of these gapless surface states. The Helical spin structure originates from a Rashba-like SOC Hamiltonian for the 2D surface state.

2.1.3 Experimental Signatures

Theoretical consideration is of course paramount for assessing the topological invariants of a material, where the non-trivial inversion of the bands must be confirmed for firm confirmation of the topologically non-trivial nature. Most of the experimental challenges revolve around clearly discerning signatures of the surface states, since the non-trivial band ordering looks practically identical to that of a trivial insulator. Some of the techniques often employed for characterising TI materials are reviewed here.

Surface State Spectroscopy

An incredibly important tool for recognising TIs is by directly observing the surface band dispersion by Angle Resolved Photo-Emission Spectroscopy (ARPES), which is based on the photo-emission of electrons from the energy bands near the surface of a material. By measuring the kinetic energy and emission angle of emitted electrons, the binding energy and crystal momentum can be reconstructed using energy and momentum conservation principles, allowing visualisation of the electronic band structure [58].

The first proposed 3D TI phase was predicted in the $Bi_{1-x}Sb_x$ alloy system, based on the inversion of bands around the L TRIM point between the end members, Bi

and Sb. Sb was found to have the inherent $\nu_0 = 1$ band-inverted structure, however possessed a semi-metal band structure with partial band overlap [42]. A full gap was found with alloying into $Bi_{0.9}Sb_{0.1}$, where the single Dirac surface band was directly imaged by ARPES, providing the first experimental evidence of a 3D TI [58]. On the basis that the Dirac surface band should also be spin-momentum locked Spin Resolved (SR)-ARPES was also employed to directly measure the spin polarisation of the surface bands in $Bi_{1-x}Sb_x$ alloys, confirming the non-trivial nature of the material [59].

After this confirmation of the 3D TI phase different material systems were proposed for study. Inherently $Bi_{1-x}Sb_x$ alloys are the result of random substitutional disorder which generally result in high defect levels, and the electronic structure is complicated: as well as the surface Dirac bands there are bulk 3D Dirac bands and trivial surface bands close to the non-trivial states for an overall complex surface dispersion [3, 4]. To overcome these issues, the topological properties of the stoichiometric, layered materials Bi_2Se_3, Bi_2Te_3, and Sb_2Te_3 were considered, which were found to be strong TIs with simple, single Dirac band surface states on the natural cleavage plane of the materials [4]. The non-trivial surface states in this material class were confirmed by ARPES [53, 60], and alloying between different members of the material class was found to produce samples with Dirac points well-separated from the bulk conduction bands [61].

Electronic Properties

Studying the electronic transport properties of these materials to uncover the surface states is another powerful tool for characterisation, which should also lead to implementation in electronic devices. Topological Insulators ideally present bulk semi-conducting or insulating behaviour and gapless metallic surface states. In the simplest case of a fully insulating bulk, the transport properties of a TI should be completely dominated by the gapless (metallic) surface states at low temperatures. Typically however, the TI candidates in the Bi_2Se_3 class have significant numbers of intrinsic defects which lead to high bulk carrier densities [62]. In these cases the surface state contributions to the transport are more subtle, and must be dis-entangled from any bulk contribution.

Significant efforts to reduce the bulk carrier densities with altered growth stoichiometry in the strong TI compounds and alloying into crystals of the $(Bi_{1-x}Sb_x)_2(Se_1-_yTe_y)_3$ (BSTS) type have been largely successful [63–66]: reducing the bulk carrier densities in BSTS alloys led to samples with a dominant 70% transport contribution from

the surface [67]. Reducing the dimensions of the samples to be measured also increases the surface to volume ratio and leads to surface dominant transport [68].

Since there is usually surface and bulk conduction in parallel and the conductive properties of the different bands are not degenerate, the transport effects must generally be considered by multiple-band models. In TIs, this leads to looking for signatures of multiple band transport in both the Hall effect and the magnetoresistance (MR) [44]. Multiple transport bands may also arise from complicated bulk band structure with multiple Fermi pockets contributing to the transport as is the case in many semi-metallic materials [57, 69, 70], or from trivial surface bands [44, 69, 70].

Changing the thickness of a sample will reduce the bulk contribution relative to a surface state and can help disentangle surface contributions more clearly, however to complement this multi-band transport analysis some probes of the non-trivial nature are required.

Weak Anti-Localisation

Due to the Dirac spin-momentum locked band structure of the surface state many TIs with significant surface contributions to the transport show a feature in the MR caused by weak anti-localisation (WAL). There is an decrease in the zero-field resistivity due to quantum interference effects related to the spin-momentum locked structure and a V-like feature with increasing field as this interference is perturbed by the application of a magnetic field [44, 71, 72].

In a disordered system, there is a possibility of an electron undergoing many low-angle scattering events and returning to its initial position, drawing out a circular path which may be traversed in both directions by partial waves ϕ_1 and ϕ_2 [73]. If phase coherence is kept around the loop, there are quantum interference terms ($I = \phi_1\phi_2^* + \phi_2\phi_1^*$) to consider that will alter the probability from the classical result, in total $P = |\phi_1|^2 + |\phi_2|^2 + \phi_1\phi_2^* + \phi_2\phi_1^*$.

In the absence of spin-orbit coupling, the two partial waves interfere constructively at the origin, and the probability of the electron being found there is doubled: this is the origin of weak localisation [73, 74].

With the addition of strong spin-orbit coupling, the spin directions of the electron partial waves need to be considered. Now, the interference terms are expressed in terms of the two-spin system [75–77] which either take a singlet ϕ_{00} or triplet form ϕ_{11}, ϕ_{10},

ϕ_{1-1}, leading to $I = \frac{1}{2}\left(|\phi_{11}|^2 + |\phi_{10}|^2 + |\phi_{1-1}|^2 - |\phi_{00}|^2\right)$. Since the spins are parallel for the triplets and their velocities are opposite around the loop, each scattering event changes the angle of each in the opposite sense, dephasing them over a scattering time τ_{so} leading to destructive interference and ϕ_{11}, ϕ_{10}, $\phi_{1-1} = 0$. The spin singlet state retains phase coherence since the spin *and* velocity directions are opposite, leading to constructive interference and $I = -\frac{1}{2}|\phi_{00}|^2$, reducing the probability of the electron returning to the origin to half the classical result, giving the WAL effect.

Shubnikov de Haas Oscillations

Many TI materials grown as single crystals show high bulk and surface mobilities, in the presence of a magnetic field this leads to carriers completing many cyclotron orbits before scattering and the formation of Landau energy levels in the energy spectrum [78]. These are essentially a quantisation of the density of states and lead to quantised Landau tubes in momentum space, where the energy level spectrum is dependent on the magnetic field strength. Changing the magnetic field strength leads to oscillatory effects in many physical properties of materials as these Landau tubes sweep through the edge of the Fermi surface [78]. A powerful tool for characterising the electronic states are oscillations in the MR of a material, Shubnikov de Haas Oscillations (SdHO). Importantly, the π Berry phase of the Dirac surface bands leads to an observable phase shift in the SdHO [54, 56, 79].

The surface and so 2D origins of the SdHO should also lead to a distinct angular dependence where the SdHO frequency, which is proportional to the Fermi surface Cross Sectional Area (CSA), should show a $1/\cos\theta$ dependence on the angle θ between the applied field and the out of plane direction [44]. The confirmation of a non-trivial Berry phase and 2D surface nature in the SdHO are strong indications of a 3D TI phase. Comparison of the carrier properties extracted from the SdHO to those extracted from the Hall resistivity can also confirm the surface nature of contributions to the semi-classical transport.

2.2 3D Topological Superconductors

Topological Superconductors are most generally defined as the topologically non-trivial counterpart to a conventional superconductor described by the Bardeen-Cooper-Schrieffer

(BCS) theory of superconductivity. Differences in the underlying electronic structure of the superconducting state lead to the non-trivial topology. Specifically, the electrons forming a Cooper pair to enter the superconducting state join in a spin-triplet with odd-spatial parity, where the odd-spatial parity is the key to the non-trivial topology. The surface state in a TSC with TRS takes the form of a gapless Majorana zero mode.

2.2.1 Topology and Odd-Parity Pairing

The many-body mean-field Bougouliobov-de Gennes (BdG) Hamiltonian most often used to describe the superconducting state is fully gapped, and is constructed to inherently reflect the particle-hole symmetry (PHS) of the superconducting state [80]. The topological index defined for such a system, with both TRS and PHS, is the topological winding number n, where it may generally take on any integer non-zero value for a topologically non-trivial system [49]. The topological phase for a TSC is then protected as long as TRS is preserved.

Exhaustive topological classification of various systems subject to different symmetry constraints has shown that the value of n can only take a non-trivial value for superconductors with Cooper pairs that have *odd* spatial parity, those where the superconducting pair potential $\Delta_{\boldsymbol{k}}$ obeys $P\Delta_{\boldsymbol{k}}P^{\dagger} = -\Delta_{-\boldsymbol{k}}$, where P is the spatial inversion operator [2, 49].

Fu and Berg [49] realised there can be an extension of the $Z2$ topological invariant ν to superconducting systems, which implies a non-zero value of n. From this, they found that superconductors with odd-parity Cooper pairs will be TSCs if the Fermi surface of the normal state encloses an odd-number of TRIM points in the Brillouin Zone.

Overall, this leads to an identification scheme of looking for odd-parity pairings in materials with a Fermi surface enclosing or close to the TRIM points in the Brillouin Zone. Some previously studied unconventional spin-triplet p-wave superconductors are therefore expected to be TSC candidates, such as $SrRuO_4$ [81–83]. Often these spin-triplet pairings are heavily susceptible to disorder which ultimately destroys the superconducting phase [80, 83–85].

Since TI materials often show Fermi surfaces close to an odd number of TRIM points, they also emerge as TSC candidates if superconductivity can be induced. The non-trivial topological superconductors of focus here arise due to the strong spin-

momentum locking effects in the bulk of these materials, leading to inter-orbital spin-triplets that are inherently protected against strong disorder [86, 87].

2.2.2 Spin-Triplets, Odd-Parity Pair Potentials and Spin-Orbit Coupling

The basic two-electron spatial wave function describing a Cooper pair of two electrons above the Fermi sea is given by [80]:

$$\psi_0\left(\boldsymbol{r_1}, \boldsymbol{r_2}\right) = \sum_{\boldsymbol{k}} g_{\boldsymbol{k}} e^{i\boldsymbol{k}\cdot\boldsymbol{r}_1} e^{-i\boldsymbol{k}\cdot\boldsymbol{r}_2} \tag{2.3}$$

with weighting coefficient $g_{\boldsymbol{k}}$ which is proportional to the effective interaction potential $V_{\boldsymbol{k}\boldsymbol{k}'}$ [80].

Here, using $e^a \times e^b = e^{a+b}$ and Euler's formula, and the fact that the spatial wave function should have a well-defined parity parity in inversion symmetric systems, we can define a symmetric ψ_s and anti-symmetric ψ_a spatial wave function dependent on the separation of the electrons [23, 80]:

$$\psi_s = \sum_{\boldsymbol{k}} g_{\boldsymbol{k}s} \cos \boldsymbol{k}(\boldsymbol{r}_1 - \boldsymbol{r}_2) \tag{2.4}$$

$$\psi_a = \sum_{\boldsymbol{k}} g_{\boldsymbol{k}a} \sin \boldsymbol{k}(\boldsymbol{r}_1 - \boldsymbol{r}_2) \tag{2.5}$$

The total wave function Ψ of the two-electron state must include a spin wave-function $\chi(s_1, s_2)$, which may also be anti-symmetric (spin-singlet), or symmetric (spin-triplet) [88]:

$$\chi_a = \frac{1}{\sqrt{2}}(|\uparrow\downarrow\rangle - |\downarrow\uparrow\rangle) \tag{2.6}$$

$$\chi_s = |\uparrow\uparrow\rangle,\ \frac{1}{\sqrt{2}}(|\uparrow\downarrow\rangle + |\downarrow\uparrow\rangle),\ |\downarrow\downarrow\rangle \tag{2.7}$$

If the two electrons are exchanged, the requirement of the two-Fermion wave-function to be anti-symmetric leads to two scenarios [88]:

$$\Psi_S = \psi_s \chi_a \tag{2.8}$$

$$\Psi_T = \psi_a \chi_s \tag{2.9}$$

where in the BCS theory only the spin-singlet state Ψ_S is considered, that is mediated by a spatially isotropic and constant attractive potential $V_{\boldsymbol{k}\boldsymbol{k}'} = -V$ [80].

The odd spatial parity required for non-trivial topology depends on the formation of Cooper pairs in the triplet state Ψ_T with a sinusoidal dependence on the electron separation, implying the pair probability amplitude reduces to zero at small separation. An attractive interaction then should fundamentally lead to a suppression of spin-triplet pairing [80, 84].

In the BdG mean-field formalism, the BCS superconducting state wave-function is defined by a pair potential described in terms of creation and annihilation operators of the electrons:

$$\Delta_{\boldsymbol{k},s} \propto \langle c_{-\boldsymbol{k}\downarrow} c_{\boldsymbol{k}\uparrow} \rangle \tag{2.10}$$

This describes the internal structure of the Cooper pair [80], where electrons with opposite momentum and opposite spin are paired together, corresponding to Ψ_S.

The proposal of the novel emergence of TSC was identified based on the non-trivial bulk Hamiltonians in TI materials, where the strong SOC leads to a Dirac-like bulk Hamiltonian containing a Rashba-like orbital dependent spin-momentum locked structure [49]. The key to realising a *stable* odd-parity pair and so TSC in these materials, without the requirement of an unconventional attractive interaction/pairing mechanism, is to include the possibility of an orbital degree of freedom in the superconducting pair potential [49].

An example of the orbital dependent spin-structure that may arise in a strong SOC material is shown in Figure 2.5, described by the Rashba-like Hamiltonian defined earlier: $\hat{H}_{SOC} = v\sigma_z \left(k_x s_y - k_y s_x\right)$ where the change in $\sigma_z = \pm 1$ between two orbitals leads to an opposite spin helicity [23, 49]. If an attractive interaction between orbitals is favoured rather than one within orbitals, a spin-triplet pairing with odd spatial parity will arise, described by a pair potential of the form [23, 49]:

$$\Delta_{\boldsymbol{k},\sigma_z,s} = c_{\boldsymbol{k},+1,\uparrow} c_{-\boldsymbol{k},-1,\downarrow} + c_{\boldsymbol{k},+1,\downarrow} c_{-\boldsymbol{k},-1,\uparrow} \tag{2.11}$$

This kind of spin-structure is naturally found in many 3D TI materials and 3D Dirac and Weyl semi-metals (DSM, WSM) on account of the strong SOC, leading to the search for TSC in superconducting TIs, WSMs, and DSMs [23, 40, 49, 89].

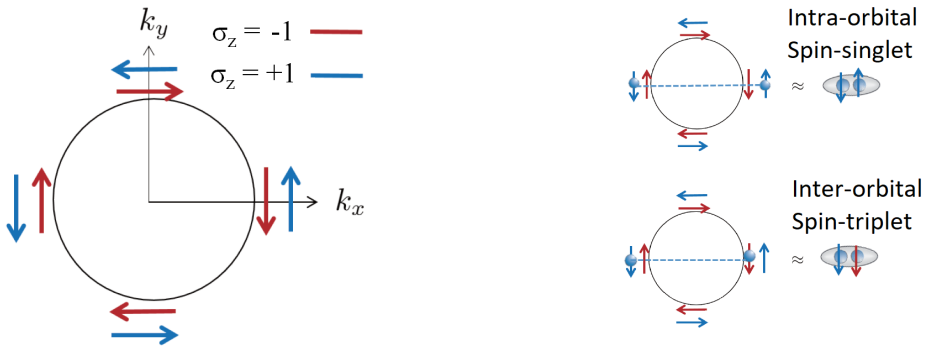

Figure 2.5: Schematic representation of the non-trivial spin-texture arising from orbital dependent SOC direction [23]. If an inter-orbital attractive interaction is preferred over an intra-orbital attractive interaction, then an odd-parity spin-triplet will form instead of an even-parity spin-singlet.

The key advantage of inter-orbital TSCs relative to intra-orbital spin-triplet pairings is related to the required pairing mechanism and the stability of the state against disorder. As mentioned, spin-triplet states are fundamentally suppressed with an attractive interaction due to the odd spatial wave-function. To prevent the suppression additional components in the interaction potential $V_{\boldsymbol{kk'}}$ between two electrons are generally required to stabilize the Cooper pairing. Some possibilities include strong repulsive components at small electron separations in strongly correlated systems [80, 83], or systems with strong spin-exchange interactions [84, 90].

Overall, the interaction potential and so superconducting gap-function may become spatially anisotropic in momentum space and spin-dependent [80, 84]. High levels of scattering ultimately average out any anisotropy and lead to a decoherence of the pair potential [86, 91], giving suppression of the spin-triplet superconducting state where a conventional BCS-like superconductor is largely unaffected [83, 85, 86, 92].

For the TSCs forming an inter-orbital spin-triplet, same spin direction and opposite momentum states can only exist in separate orbitals due to the orbital dependent spin-momentum locked structure. The suppression of the anti-symmetric spatial wave function now relies on the scattering of electrons between orbitals, which is suppressed compared to intra-orbital scattering due to the spin-orbit locked structure [86]. Formally an emergent chiral symmetry related to the spin-momentum locked structure protects the superconducting state, though the pairing is still eventually suppressed with

strong disorder [86, 87]. So far, spatially isotropic attractive interactions arising from the conventional electron-phonon coupling are also expected to be able form the Cooper pairs [49, 86].

2.2.3 Majorana Zero Mode Surface States

From the bulk-boundary correspondence, the non-trivial topological nature of the bulk superconducting state must produce a gapless surface state. In the case of a 3D TSC obeying TRS, PHS, and breaking SU(2) spin-rotation symmetry, this surface state takes the form of a 2D Majorana Zero Mode (MJZM) [5].

Generic surface states are not unusual for superconductors: systems with spatially anisotropic pair potentials give Andreev bound states (ABS) on the surface [93]. At the surface of a superconductor the Cooper pair must break down, leading to energy levels within the superconducting gap that are populated by electron-hole quasi-particles bound to the surface. The energy level of such an ABS reflects the internal symmetries of the pair potential [94]. In the specific pair-potentials describing the odd-parity spin-triplet inter-orbital pairing of TSCs, the ABS shows linearly dispersive bands that are enforced to be degenerate at zero-energy [22].

In the Bougouliobov-de Gennes formalism, broken Cooper pairs are viewed as quasi-particle excitations above the superconducting ground state [80]. These are described by the superposition of electron-hole creation and annihilation operators, which are linked to one another by $\gamma(E) = \gamma^{\dagger}(-E)$ due to the PHS of the state [6, 7, 80].

The fact that the ABS are fixed to zero-energy on the surface of a TSC means that the operators for creation and annihilation are equivalent. Also, the linearly dispersive nature of the excitations means they are described by the relativistic Dirac equation in an analogous fashion to TIs, and the non-trivial topology of the bulk leads to a single surface ABS [22, 23]. Finally, the spin-momentum locked structure of the electronic states breaks spin-rotation symmetry, and overall the single surface ABS of an inter-orbital spin-triplet TSC is actually a 2D MJZM: the quasi-particles are then referred to as Majorana fermions [6, 7].

An example of this surface state spectrum is shown in Figure 2.6a [22]. Figure 2.6b shows the combination of a non-trivial bulk pairing and the preservation of a Dirac cone TI surface state when transferring to the TSC phase, leading to a more complicated surface dispersion, which however remains a MJZM on the surface [22].

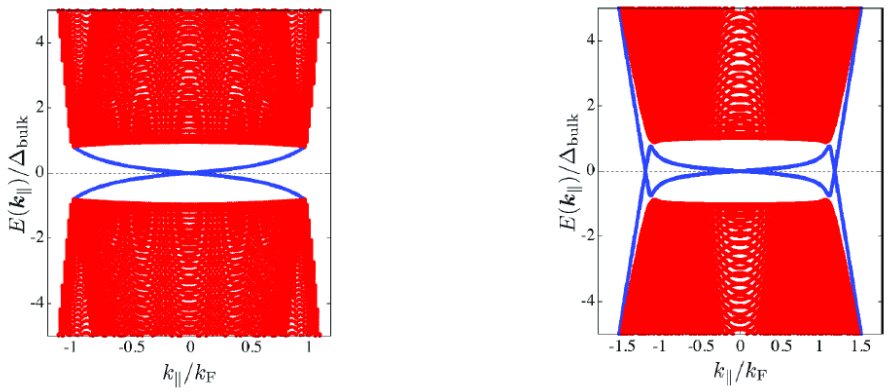

(a) (b)

Figure 2.6: Numerically calculated examples of MJZMs found on the surface of a TSC with a fully gapped pair potential [22]. (a) Example of simple surface state structure without a remnant Dirac cone from an underlying topological normal state. (b) Example of more complicated surface dispersion resulting from the interference of the emerging MJZM and preserved normal state Dirac cones.

The primary drive for realising isolated MJZMs is for their prospective use as the underlying components of topological quantum computers. In essence, the topological origin of the surface state protects against suppression of the underlying computational unit, and the exchange of single MJZMs leads to topologically protected quantum operations on the wave-function of the particle [11, 12].

2.2.4 Experimental Signatures

Again, full theoretical consideration of the underlying electronic structure is required to confirm a TSC phase. The novel structure of the Cooper pair, described by the pair potential, often called the superconducting gap function, may however lead to experimental signatures separate from the direct observation of the surface states. This section reviews some of these features, and details the more direct methods for confirming the MJZM surface states and TSC phase.

Unconventional Thermodynamics

Unconventional pairing symmetries generally lead to unconventional behaviour in many of the standard probes of superconductivity. Formally, the energy gap function derived for conventional s-wave BCS superconductors can be used to calculate many of the bulk thermodynamic properties of the superconducting state [80]. Often, novel pairing symmetries can lead to divergence from the BCS theories predictions, especially in the temperature dependence of the bulk properties for anisotropic gap functions in the unconventional superconductors [92]. Similar ideas can therefore be transferred to TSCs, which suggest an unconventional nature of the superconducting state if measurements deviate from the BCS or Ginzburg-Landau (GL) theory.

Formally, full theoretical consideration of the different permitted superconducting pair-potentials for a particular crystal structure are required, and the effect that these should have on the bulk properties must be calculated in detail [92]. Notably, gap anisotropies are not necessarily guaranteed since the pairing interaction may generally be phonon mediated, spin-independent and spatially isotropic in TSCs [49, 80, 86], and in some cases fully gapped spin-triplet pairings can lead to identical behaviour to a fully gapped spin-singlet pairing [85, 92]. Nevertheless, some unconventional behaviours are present in many of the standard probes of superconductivity in TSC materials, and these signatures are reviewed here.

First, the normalised scale of the electronic specific heat jump when entering the superconducting state may be modified beyond the weak-coupling BCS limit of 1.43 [80, 95, 96]. In itself this probes only the coupling strength, since an isotropic s-wave pairing is assumed in theory, however TSCs often show divergence from BCS weak-coupling behaviour [96].

To probe the nature of the pairing more directly, the temperature dependence of the specific heat is related directly to the temperature dependence of the energy gap and so the pair potential. Deviations from the behaviour predicted for a BCS s-wave superconductor [80, 97] have been identified in $Cu_xBi_2Se_3$ [96], and behaviour consistent with nodal d-wave behaviour has been identified in TSC candidate $Cu_x(PbSe)_5(Bi_2Se_3)_6$ [98].

Formally, the full microscopic details of the superconducting pair potential will also affect the temperature dependence of the critical field values of a superconductor, leading to different quantitative theoretical predictions [92]. For example, behaviour

consistent with p-wave spin-triplet pairing symmetry has been found in TSC candidates β-$PdBi_2$ [99] and $Cu_xBi_2Se_3$ [100, 101].

Another approach is to consider the detailed temperature dependence of the penetration depth for various superconducting gap functions, where most differences are seen at low temperatures [80]. In unconventional Type-II superconductors muon spin-rotation (μ-SR) experiments have emerged as a powerful tool for characterising the spectrum of local magnetic fields, which then allows determination of the penetration depth since the local field variation around vortices depends on the value of $\lambda(T)$ [80, 102]. Recently, the μ-SR technique was applied to TSC candidate ZrRuAs, where good agreement with s-wave behaviour was found suggesting conventional behaviour [97]. Further investigations have been undertaken in various intercalated Bi_2Se_3 samples, where signatures of unconventional superconductivity have been uncovered [103, 104].

Full theoretical consideration of the impact of different pair potentials was carried out in detail for the first TSC candidate $Cu_xBi_2Se_3$ [105–107], where examples of nematic superconductivity have been experimentally identified in many of the thermodynamic quantities [108, 109].

Notably, some spin-triplet states with odd parity may present essentially identical isotropic gap functions, and therefore identical equilibrium properties to spin-singlet superconductors [92]. However, due to the different spin-states present in TSCs, pair-breaking effects of the magnetic field are also generally expected to have a different impact on the critical field values [92].

Magnetic Field Pair Breaking Effects

Type-I and Type-II superconductors are defined in the GL theory depending on the GL parameter $\kappa = \lambda/\xi$, with effective field penetration depth λ and effective superconducting coherence length ξ, where $\kappa = 1/\sqrt{2}$ separates Type-I ($\kappa < 1/\sqrt{2}$) and Type-II ($\kappa > 1/\sqrt{2}$) [80]. At the boundaries between a normal state region with magnetic field B and a superconducting region, the B field is screened exponentially with a characteristic length scale λ and the superconducting condensate order parameter recovers over a characteristic length scale ξ [80]. The distinction between Type-I and Type-II arises due to the surface energy at this domain wall, which is positive in Type-I with $\xi \gg \lambda$ and negative in Type-II with $\lambda \gg \xi$ [80].

The key physical difference between these regimes is the behaviour in a magnetic

field. A Type-I superconductor (with no demagnetising shape effects) completely screens a magnetic field, due to the energy cost associated with the domain wall and so minimisation of these boundaries, up to a thermodynamic critical field B_c where the superconducting state is suddenly destroyed. A Type-II superconductor allows magnetic flux to penetrate above a lower critical field B_{c1} in normal state vortices containing the minimum magnetic flux quantum Φ_0, due to the negative domain wall energy promoting the formation of a maximum number of vortices with minimal flux contained in each, where the superconductivity is destroyed at an upper critical field B_{c2}.

The thermodynamic and upper critical fields of Type-I and Type-II superconductors represent the point at which the work done by the superconducting condensate in counteracting the magnetic field by setting up screening currents is equal to the condensation energy of the superconducting state [80].

In the BCS and GL theory the critical fields are calculated based on thermodynamic principles [80]. In reality, the free-energy of the superconducting state in a magnetic field is also affected by contributions of Landau diamagnetism (orbital de-pairing effects), Pauli paramagnetism (spin de-pairing effects), and by spin-orbit coupling, which are formally accounted for by the Werthamer, Helfand and Hohenberg (WHH) theory [110]. These additional Cooper pair-breaking or stabilising effects related to the spin-state will affect the internal-energy of the Cooper pair in a magnetic field, and so affect the overall magnitude of critical field values [80].

The WHH equation (see e.g. [111]) is solved numerically to give a value of the upper critical field at a fixed temperature for a dirty Type-II superconducting system, taking the critical temperature, mean-free path and Fermi velocity as fixed parameters. Two additional fitting parameters, the Maki parameter α quantifying the strength of the spin-paramagnetic pair breaking effects that reduce the critical field values, and λ_{SOC} quantifying the strength of the stabilising SOC effects that increase the critical field values, can then be determined.

The WHH equation with $\alpha = \lambda_{SOC} = 0$ always includes orbital de-pairing effects, and the critical field values predicted in this limit act as an upper limit for the critical field values of a superconductor in a conventional spin-singlet pairing [111–113]. This is because with some finite α and strong SOC ($\lambda_{SOC} \gg 1$), the upper critical field values predicted by the theory are equivalent to those when $\alpha = \lambda_{SOC} = 0$ [111–113], meaning these values cannot be surpassed. Formally, the WHH upper critical field values with

$\alpha = \lambda_{SOC} = 0$ are only surpassed by spin-triplet superconductors [114]. This fact has been used for evidence of spin-triplet pairing in many TSC candidates [99–101].

Fundamentally, the pair breaking effect from Pauli spin-paramagnetism has a larger effect on spin-singlet pairings than the aligned spin-triplet Cooper pairings, leading to the expectation of a small or negligible suppression of the critical field values due to the spin-paramagnetic effect in spin-triplet superconductors [114]. Since spin-orbit coupling provides a spin-stabilising effect against the Pauli spin-paramagnetism, in the limit of strong spin-orbit coupling the Pauli spin-paramagnetism may be completely counteracted [111, 113]. However, the upper limit of the WHH theory cannot be surpassed even in this case due to the spin-singlet structure. Surpassing the WHH limit remains a signature of spin-triplet pairing [99–101].

Smoking Gun Experiments

For less well studied materials and novel TSC candidates, it is important to initially look for deviations from standard BCS behaviour for suggestions of unconventional behaviour. These signatures may either way be confirmed by more direct probes of the topological nature of the state. Smoking gun experiments in TSC systems are those that provide a more direct probe of the symmetry of the pair potential, or those that directly measure the surface state spectrum to confirm the existence of a MJZM on the surface.

A powerful tool for investigating TSC is the use of tunnelling spectroscopy [93] [94]. As mentioned earlier anisotropic pair potentials result in electron-hole quasi-particle ABS on the surface of a superconductor. Since these bound states are a finite density of states residing in the superconducting energy gap, they allow a finite tunnelling current in point contact measurements for voltage bias' within the superconducting gap, where for fully gapped BCS superconductors there is no tunnelling current [80]. For the case of odd-parity TSCs which have Majorana zero modes on the surface, the conductance peaks occur at zero voltage bias and are dubbed zero bias conductance peaks (ZBCPs). These have been confirmed in many 3D TSCs [115, 116].

A large body of work aiming to achieve these signatures so far has focused on proximity-induced superconductivity in TI wires, where the induced superconductivity becomes topologically non-trivial due to the spin-texture in the TI, and accordingly MJZMs appear localised at the boundaries of the systems [24]. Some studies report

on the observation of ZBCPs in TI/conventional superconductor heterostructures [25], however these systems are extremely difficult to fabricate cleanly, as a recent high-profile retraction attests to [117].

Some open questions in the field revolve around Josephson Junction devices, which are sensitive to internal phase differences between the pair-potentials of different superconductors, and as a result can be used to probe the pair potential of TSCs [22, 118]. The Josephson current between a conventional s-wave superconductor and a TSC should take a second order form $J(\phi) \sim \sin(2\phi)$ with phase difference ϕ, and so is distinct from the first order form in a SNS junction comprised of BCS superconductors [118].

There is a growing effort to realise coupled Josephson Junction architectures in proximity induced TIs: some examples of the second order form of the Josephson current have been established using the proximity effect in S-TI-S junctions [119, 120]. Anomalous Josephson currents have also been realised in crossed-junction structures on the surface of 3D TI Bi_2Se_3 [27].

Chapter 3

Methods

3.1 Growth Methods

3.1.1 Single Crystals - Modified Bridgman Method

The processes and equipment for this material growth were set up by the author alongside Dr. B.D.G. Steele and Dr. S. Sasaki prior to the start of this project. The first Sb_2Te_3 sample with nominally stoichiometric composition was grown prior to this thesis, which was used for control in an investigation of Sn and Pb doped Sb_2Te_3 that is not reported here. All subsequent work was carried out during the author's PhD campaign.

The single crystal growth procedure of Sb_2Te_3 consists of 4 steps: weighing the desired amounts of each element, sealing in a clean quartz ampoule, box furnace pre-reaction of Sb and Te into a poly-crystalline Sb_2Te_3 ingot, and finally single crystal growth in a vertical tube furnace with a stable temperature gradient.

Source material pellets are kept in a controlled N_2 atmosphere glove box to protect them from oxidation and contamination: typical relative humidity values are below 2%. Stoichiometric amounts are weighed before being sealed at vacuum ($P \sim 10^{-2}$ mbar) in an Ar purged and roughing pump evacuated quartz tube using an oxygen-acetylene torch. All the materials used are 5N purity, and are weighed repeatedly to within a standard error of $\pm$ 10 μg of the required amounts. To ensure a well mixed sample before the Bridgman growth the pellets are initially melted together and mixed in a box furnace at 800°C for at least 24 hours. This mixing process promotes an even distribution of material, judged by the uniform colour of an ingot afterwards.

Large and high-quality single crystal examples of the strong 3D TI candidates can be reliably grown using a modified Bridgman method [121, 122]. The standard Bridgman method slowly pulls a sample through a temperature gradient from above the melting point to below it, where the temperature gradient must be large enough to have a well defined point where crystallization occurs and the pulling rate set appropriately slowly so that crystallization is continuous from the initial nucleation site [123]. The same is true for the modified method, however instead of moving the sample the furnace is cooled at a controlled rate, meaning the crystallisation temperature line moves across the sample instead, overall requiring less equipment to implement.

Figure 3.1a shows a schematic of the vertical tube furnace set-up and temperature profile. The fire bricks, ceramic plate and insulating blanket are used to prevent air

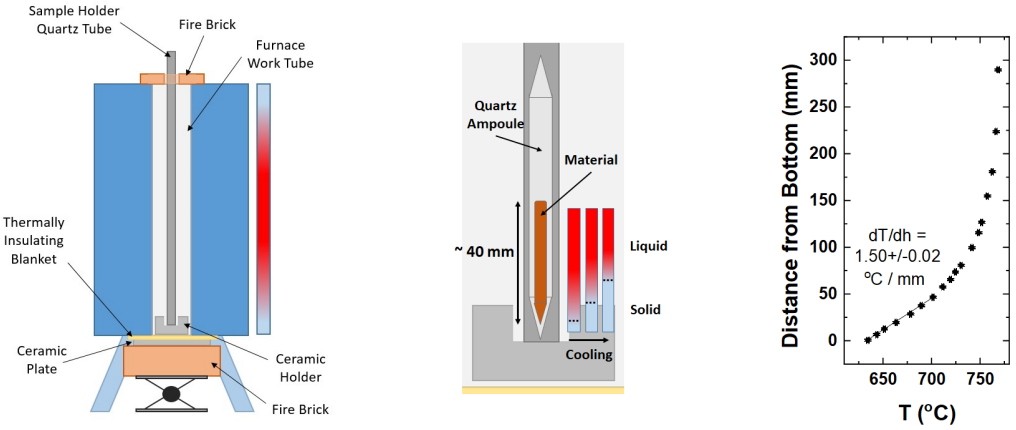

(a) (b) (c)

Figure 3.1: (a) Schematic of the vertical tube furnace used to implement the modified Bridgman method, with simple representation of the temperature profile. (b) Representation of single crystal growth driven by the moving temperature gradient. (c) Measured temperature gradient at the bottom of the furnace, which is linear across the sample length and remains the same during the growth.

currents moving through the furnace that would disrupt the temperature gradient, the ceramic holder improves the reliability of sample positioning radially. Figure 3.1b details the growth mechanism: as the furnace cools the point of the furnace at the crystallisation temperature (dashed line) moves up across the sample. Figure 3.1c shows an example of the temperature gradient of the furnace measured with an external thermocouple inserted at different lengths into the furnace. This was taken with the bottom temperature of the furnace slightly above the melting point (620°C) of Sb_2Te_3, with a set-point temperature of 770°C, which is the temperature in the middle of the furnace. The temperature gradient across the length of the molten material (typically $\sim$ 40 mm) is linear and equals 1.50 ± 0.02 °C/mm. Reducing the set-point temperature of the furnace should decrease this temperature gradient since the 'coldest' point is always at room-temperature, and so it may change during the growth: it was found however to remain constant within the uncertainty down to a set point of at least 670°C, at which point all of the material will have crystallised.

A full cycle of a modified Bridgman growth consists of a high temperature re-melt and mixing period, followed by a controlled cooling through the melting point where

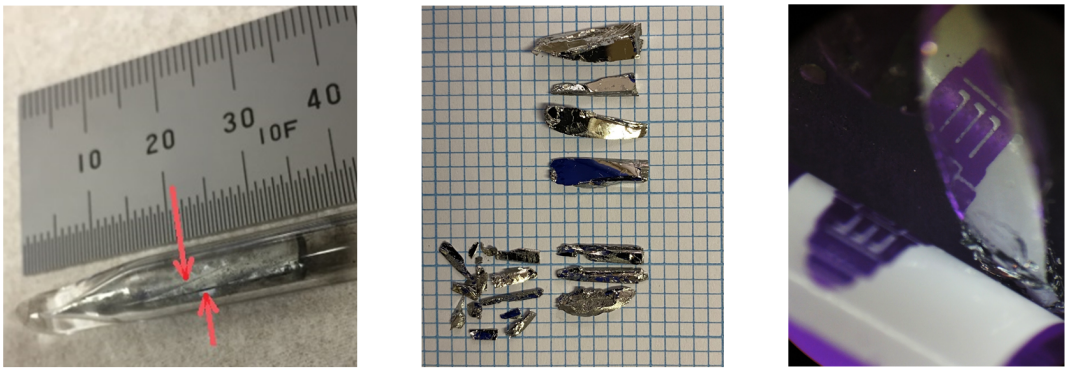

(a) (b) (c)

Figure 3.2: (a) Examples of growth lines signifying the formation of large single crystal segments in the material ingot after the modified Bridgman method. (b) The growth ingots can be cleaved apart to reveal large single crystal segments and more polycrystalline regions (bottom). (c) Example of pristine mirror-like surface of a single crystal after cleaving.

crystallization occurs, and finally cooling to room temperature. A mixing temperature close to 800°C is again used for 24 hours, and a cooling rate of 0.1°C/min from 700°C to 530°C was found to produce large single crystals that often extend across the entire length of the material ingot.

Multiple initial crystal nuclei may form single crystals concurrently using this growth method, so after growth the total ingot may consist of separate single crystal segments and more polycrystalline regions. An example of the ingot after growth is shown in Figure 3.2a, where clear growth lines can be seen indicating good, but multiple, single crystal formations. The samples cleave apart easily when applying pressure to these growth lines with a razor or scalpel, revealing mirror-like single crystal segments and more poly-crystalline regions as shown in Figure 3.2b. An example of the pristine mirror-like nature of the crystals is shown in Figure 3.2c. It was found that the shape of the bottom of the quartz tube would impact the quality of the single-crystal formation: an even conical shape extending to a sharp point led to fewer competing forming segments of single crystals and so overall larger ingots to be taken for further measurement.

3.1.2 Thin-films - DC Sputtering

As discussed later, DC sputtering is selected as the deposition method for repeating Pb-Rh-Pb multilayer units, which are then annealed post-growth to mix the layers and form $RhPb_2$. This method is selected based on its relative ease of implementation, with specific apparatus and appropriately sized material targets available at the University of Leeds for layer-by-layer deposition, and also since stoichiometric thin-films of TSC candidates are highly desirable for future applications. This section briefly reviews the process of DC sputtering [124] and details the apparatus used.

Sputtering relies on the ejection of a source material by high energy ions, where the kinetic energy of the ion is greater than the binding energy of atoms within the solid, allowing them to be ejected by a collision. In this work, DC magnetron sputtering with Ar plasma is employed. A deposition chamber is pumped out to UHV ($\sim 10^{-8}$ mbar) and a small amount of inert gas is introduced (Ar at 2.4 mTorr). An electric field is held between a cathode (target) and anode (substrate) using a large potential ($\sim$ kV), where electrons with high energy collide with the Ar atoms and eject electrons in an ionisation event, creating the unbound charged particles that form the plasma. The positively charged Ar ions are then accelerated to the target and collide with $\sim$ keV kinetic energy to eject sputter atoms. Permanent magnets behind the sputter target produce a magnetic field is used to confine the positive ions radially, since there is a horizontal radial component of the magnetic field and a vertical drift velocity from the electric field, the Lorentz force on the ions produces an circular drift current parallel to the target surface: the charged ions drift whilst undergoing cyclotron motion and colliding with the target. Electrons are also confined by this field, improving the efficiency of ionisation events and therefore increasing the sputter yield.

After ejection, the neutral sputtered atoms of desired material have some kinetic energy and move around the chamber by ballistic or diffusive transport, depending on the Ar gas pressure, and ultimately arrive at the substrate. The energy of the arriving atoms and flux of other species in the plasma determine the growth morphology of the thin film, as does the substrate material and temperature, since the growth morphology is determined by the competition of inter-atomic forces and the energy of arriving atoms [125]. Here, a cold growth is used with reasonably low Ar pressure/high energy sputter atoms to produce continuous layers of the targeted materials, which are then annealed post-growth aiming for mixing of the layers and re-structuring of the films.

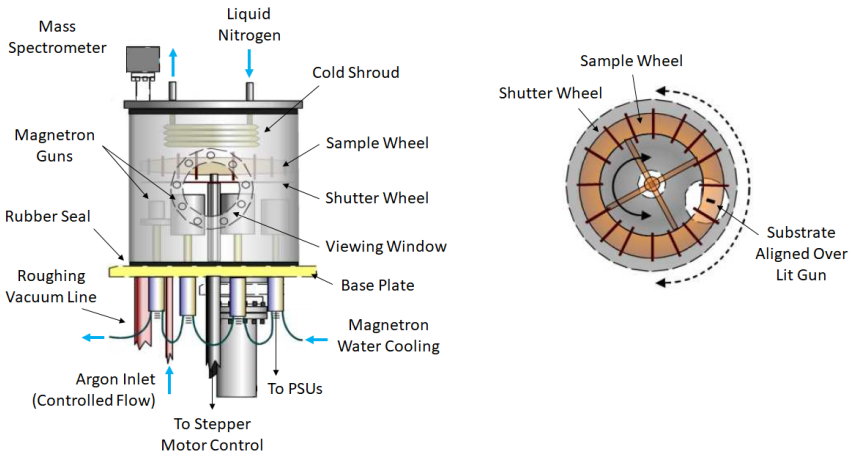

Figure 3.3: Schematic of the DC Magnetron Sputtering growth system used in this work, adapted from [126].

The apparatus used was built in house at the University of Leeds, shown schematically in Figure 3.3. A roughing pump and cryo-pump are connected to the main chamber, the roughing pump initially evacuating to $\sim 10^{-2}$ mbar and then the cryo-pump evacuating to a pressure of $\sim 10^{-8}$ mbar. A cold shroud is also used with a continual flow of liquid nitrogen to condense gaseous impurities out of the chamber to reduce the pressure and impurity content further. Substrates are mounted on Cu plates with Kapton tape, which are secured in a rotatable motor controlled sample holder wheel and aligned directly above the target materials before growth. A motor controlled shutter wheel is also present to block substrates from the sources to prevent unwanted deposition. The shutter wheel also contains a permanent magnet array around the opening to deflect energetic charged particles that may cause unwanted re-sputtering of the grown material or damage the films. Growth of one layer of a specific thickness is performed by moving a substrate and open shutter over a lit source for a certain amount of time and moving off again: movement and timings are controlled automatically by in-house software.

During growth Ar is introduced to a working pressure of 2.4 mTorr and the sputter rates for specific materials at this growth pressure are controlled based on the power discharge through the plasma by controlling the current from the Power Supply Units (PSUs). Rh is a hard material with high binding energy, requiring 50 mA current for 2 Å/s growth rate, Pb is much softer with 10 mA giving a 3 Å/s rate. Both materials

used are 5N purity: a thick-film of Pb showed T_c (defined as the midpoint of the resistive transition) of 7.19 ± 0.02 K, with transition width $\Delta T_c = 0.2$ K, suggesting no magnetic impurities; a thick film of Rh showed a small upturn in resistivity at low temperature which was not removed by magnetic field, thereby discounting Kondo effects and suggesting no magnetic impurities. Further information regarding the film structure and annealing process is discussed in Chapter 5.

3.2 X-Ray Characterisation

After growth, cleaving, or annealing, the primary mode of structural characterisation used in this work is the scattering of x-rays. This section details the x-ray apparatus set-up and introduces some of the characterisation methods employed.

3.2.1 X-Ray Apparatus

For all measurements in this thesis a 2θ-θ Bragg geometry was used in a commercial Bruker D8 diffractometer with Cu as the x-ray source. For the Sb_2Te_3 investigation both the Cu-$K_{\alpha-I}$ and Cu-$K_{\alpha-II}$ radiation was present, with Cu-K_β filtered out by a Ni plate. For the $RhPb_2$ investigation a 4-bounce Ge (002) monochromator was used to retain only Cu-$K_{\alpha-I}$ radiation.

The system has multiple degrees of freedom for the alignment of samples. In all cases the measurements are taken in an out-of-plane geometry, so diffraction occurs from planes parallel to the flat planar surfaces of both the single crystal and thin-film samples.

3.2.2 X-Ray Diffraction

X-ray diffraction (XRD) is a powerful technique for characterising the crystalline state. It relies on the diffraction of x-rays from the periodic arrangement of atoms in a crystal lattice to angular positions defined by Bragg's law, leading to the observation of sharp peaks in diffracted intensity. Here, XRD is primarily used to identify already known phases by comparison to published crystal structures, and to track the structural quality of a materials system undergoing different preparatory treatments.

The primary goal of phase identification is performed by measuring the high-angle XRD peaks and comparing these to known spectra from the materials of interest, which

also rules out the presence of impurity phases. The position of a particular XRD peak is directly related to the size of the crystalline unit cell and the orientation of planes that are diffracted from. The measured peak positions are compared to reported values in the literature: the standardised unit-cells for Sb_2Te_3 and $RhPb_2$ are modelled in the PowderCell software suite to produce complete XRD scans for comparison.

Ideal single crystals grown without twinning or multiple domains should present higher orders of a single index peak for a particular alignment orientation: this fact is used to ensure that cleaved single-crystals are single domain and confirm the out-of plane orientation for the interpretation of transport measurements in magnetic field.

Thin films may generally be amorphous, polycrystalline with no preferred orientation, polycrystalline and textured, or completely epitaxial, depending on the substrate choice, growth method and conditions. The goal of this work is to grow crystalline films of $RhPb_2$, given the amorphous/polycrystalline Rh buffer layer used to chemically protect the phase, either polycrystalline or textured thin films of $RhPb_2$ are anticipated and XRD is used to characterise the dominant orientations of $RhPb_2$ forming in the films. The progression of phase formation in the films with annealing time and temperature is also determined by XRD.

Detailed quantitative information regarding the structural quality of the materials in this work is not used. To fully account for the various factors affecting the intensities and width of diffraction peaks not arising from the intrinsic properties of a sample is a highly non-trivial undertaking. Instead, qualitative trends are analysed in series of the same materials by looking at how a particular diffraction peak may change by some different treatment of the system. To do this reliably, the beam geometry and collimation is kept fixed so that the instrument factors are equivalent in each case. Also the sample dimensions for each material system studied are kept approximately the same.

For bulk single crystal samples, information regarding lattice dimensions can be compared from peak positions, and changes in overall structural disorder due to micro-strain from vacancies and lattice defects can be judged by changes in diffraction peak widths, for a fixed peak index. In thin-film samples the peak widths will be affected by grain size and by lattice defects. Since the growth method uses an annealing protocol to form the desired phase, the total peak area can also be tracked with various parameters, corresponding to the overall phase strength.

3.2.3 X-Ray Reflectivity

X-ray reflectivity (XRR) is an effect based on the reflection of x-rays from surfaces and interfaces in multilayer films. The reflection or transmission of x-rays from an interface depends on the electronic density of the two materials and the angle of incidence, leading to different levels of reflection from different interfaces in multilayer films [127]. For a single layer film with thickness t, the interference of reflections from the surface and interface leads to the well known oscillatory form, Kiessig fringes, the form used for single layer fitting in this work given by:

$$\theta_{m+1}^2 - \theta_m^2 = \frac{\lambda^2(2m+1)}{4t^2} \tag{3.1}$$

describing the angular separation between two peaks with index m [127].

For multilayers, the full XRR pattern is a combination of oscillatory Kiessig fringes from different reflections in the films, where the scattering length density (SLD) profile of a specific sample determines the exact form of the XRR pattern [127]. The SLD profile depends on the chemical make-up of each layer, the density of each layer, and the roughness of the interfaces between layers [127]. Fitting software can model the SLD profile for a multilayer film and predict the XRR pattern, thereby allowing fitting of a measured XRR pattern by parameter refinement.

In this work, the open source software GenX is used to fit XRR data from multilayer films. Initially this allows characterisation of layer thickness, densities, and roughness to judge to success of a growth run and determine the nominal composition of a film to be annealed. This is also used again after annealing to check for buffer and cap layer inter-mixing effects, which also determines whether significant impurity phases may have formed.

3.3 Electronic Transport

3.3.1 Cryostat Systems

^{4}He System

To investigate the electrical properties of materials in this thesis at temperatures between 300 K and 1.5 K ^{4}He cryostats with variable temperature inserts (VTI) are used: a schematic of which is shown in Figure 3.4a. The cryostat essentially consists

of a constant temperature (4.2 K) liquid ^{4}He reservoir that is used as a transfer gas for cooling and heating from room temperature to 4.2 K: liquid ^{4}He is introduced through a porous inlet block, where the total flow rate is controlled by a motorised needle valve, and the temperature of the exchange gas controlled by a heater next to the inlet block. The amount of heating or cooling power from the VTI inlet to the sample is controlled by the quantity of gas flow and the pumping speed of the connected roughing pump.

To reach temperatures below 4.2 K the roughing pump connected to the VTI reduces the vapour pressure of ^{4}He in the VTI which results in a lower temperature [128]. A typical minimum working temperature of 1.5 K is achieved by balancing the inlet gas-flow with a rotary pump capable of evacuating to $\sim 10^{-2}$ mbar.

The inner vacuum, liquid nitrogen jacket and outer vacuum are used to thermally insulate the He-reservoir, the liquid nitrogen jacket acts as a heat sink to reduce heat transfer into the He reservoir. Radiation baffles are present in the VTI to disperse radiative heating from the top of the cryostat. Unlabelled ports on the top of the cryostat are for reservoir filling, vacuum pumping, and safety relief valves.

A superconducting solenoid is submerged in the liquid helium reservoir around the sample space which is used to produce magnetic fields up to 8T along the vertical directions in Figure 3.4a. Sweeping the field between -8 T (down) and 8 T (up) allows measurement of the magneto-transport of the sample, which can be taken in various configurations depending on the orientation in which the sample is mounted.

The chip carriers containing the samples are mounted in brass holder heads, in close proximity and with good thermal contact to a calibrated Cernox temperature sensor, and electrical contact is made to the base pads of the chip carrier with non-magnetic spring-loaded pins. The sample holder is then connected to a probe stick that contains the thermometry and twisted-pair measurement lines which run to a break-out box that is used to connect to the current-source and voltage-measurement equipment. Different orientation heads are used to change the sample orientation relative to the field.

^{3}He System

To reach temperatures below 1.5 K, an Oxford instruments ^{3}He based 'Heliox' insert is used in-place of the VTI, with schematic shown in Figure 3.4b. The physical principle behind reaching lower temperatures than a ^{4}He based cryostat is that much less pumping capacity is required to reduce the temperature of ^{3}He, since the vapour pressure is

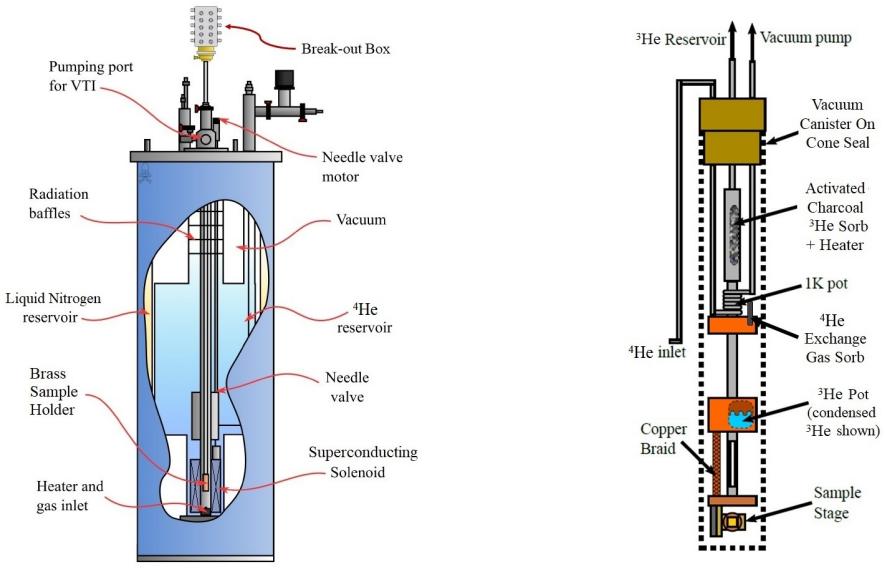

(a) (b)

Figure 3.4: (a) Schematic of the ^{4}He Dewar with VTI insert adapted from [129]. (b) Schematic of ^{3}He Heliox insert adapted from [130].

overall higher due to the lighter mass [128]. Since ^{3}He is extremely rare and expensive, a closed system is desirable. In place of a roughing pump and re-cycling system which risks some leakage, the ^{3}He is pumped on by an activated charcoal sorb within a closed system in the Heliox insert.

The operation is as follows. The entire sample space is enclosed in a vacuum can sealed by being evacuated and pulled onto a cone seal with high-vacuum grease. The sample space is purged with clean ^{4}He and evacuated multiple times, and finally pumped out to $\sim 10^{-5}$ mbar using an oil diffusion pump, to minimize ice build up upon cooling. A single 10 cm^3 shot of ^{4}He exchange gas is finally introduced to provide a heat link between the 4.2 K ^{4}He bath and the insert, allowing efficient initial cooling upon insertion to the bath. Once lowered into the ^{4}He bath and pre-cooled to 4.2 K, opening a needle valve on the ^{4}He inlet line, pumped on by a roughing pump, will draw in ^{4}He from the bath and cool the 1 K pot region and ^{4}He exchange gas sorb to 1.5 K, where it will capture all of the ^{4}He exchange gas and remove the heat link to the bath.

After this, a heater within the closed ^{3}He system on the sorb is used to raise the temperature to 30 K and de-sorb the ^{3}He gas condensed there, which will be cooled

by passing near to the 1 K pot line and condense into the ^{3}He pot. After roughly 30 minutes all of the ^{3}He gas will be condensed into the ^{3}He pot. Turning off the ^{3}He sorb heater, its temperature will slowly reduce to that of the 1 K pot line that it is mechanically linked to, and it will begin to pump ^{3}He and reduce the saturated vapour pressure of the liquid and so temperature of the ^{3}He pot. The sample space is heat linked to the ^{3}He pot by a thick copper braid and closely follows the temperature of the ^{3}He bath.

Significant heat-sinking is performed near the 1K pot region, since there is active cooling there, and a section of the measurement lines are made of high resistance wire to reduce heat transfer to the sample from room temperature. With the 1 K pot and ^{3}He sorb at 1.5 K, the ^{3}He pot can reach a temperature of 260 mK, the sample space temperature is measured by a calibrated cernox mounted on the sample chip carrier, and will reach a minimum temperature of 380 mK. Temperature control below 1.5 K is by changing the ^{3}He sorb temperature and so adsorption ability, a heater on the ^{3}He pot can be used to control the temperature above 1.5 K when the ^{3}He evaporates.

3.3.2 Sample Preparation

Single Crystals

The preparation procedure of single crystals for transport measurements consists of 3 main steps: cleaving and exfoliation of a pristine mirror-like sample into an appropriate shape, attaching gold wires with silver paint in a Hall bar configuration, and then securely mounting the wired sample onto a standard gold plated chip carrier. In order to obtain high quality electronic transport data in single crystal samples significant care must be taken during sample preparation in order to minimize the effects of extrinsic factors such as sample deformation, poor contact resistances, and oxidation.

Initial cleaving of single crystal segments from the growth ingot is performed with a razor blade by gently pushing along growth lines, these are cut into cuboids approximately 4 mm x 1 mm lateral dimension using a diamond wire saw, which gently grinds through the sample without applying pressure and deforming the single crystal segments. Samples are held in place during cutting by beeswax which is easily removed in warm (50°C) acetone. These cuboid are then ex-foliated with kapton tape to $\sim$ 0.1 mm thickness, where the planar single crystal surfaces in contact with wax/acetone are removed.

Attaching 25 μm diameter gold wires to the sample by hand using silver conductive paste results in ohmic contacts ($\sim 1\ \Omega$) after curing in a small vacuum chamber at room temperature that are mechanically sturdy, occasionally gentle current annealing is used if contact resistance is greater than 10 Ω. Hall bar geometries are used in all cases of single crystals measurements, shown in Figure 3.5a, so that the Hall effect and MR can be measured simultaneously at the same temperatures, an important consideration when SdHO from both quantities are to be compared.

In Figure 3.5a, V_{xx} signifies measurement of a longitudinal voltage, and V_{yx} measurement of a transverse voltage. Since the transport properties of Sb_2Te_3 are isotropic in the mirror plane [131], the only component contributing to V_{yx}, for perfectly aligned contacts, is the Hall voltage for a non-zero B. With B pointing perpendicularly out of the sample mirror plane, we define the out-of-plane MR that is measured on V_{xx}. The measured magnetotransport data is processed into even and odd components with field to remove any artefacts due to contact misalignment, since the Hall voltage is odd in field and the MR is even.

Large current contacts are connected to the end areas of the sample with a full and even distribution of silver paint across the entire face to promote planar current injection, the lateral extent of the four voltage leads are minimised to reduce voltage averaging and error in resistivity determination, but they are extended across the thickness of the sample.

Sample lateral dimensions between the voltage contacts are measured using a motor-controlled 2-axis sample stage underneath an optical microscope, which can directly map the contact co-ordinates (x, y) in real space to calculate the sample dimensions. Uncertainties in the lateral dimensions due to the size of the contacts are typically 50μm, roughly twice the wire width. Misalignment between the centres of the contacts is typically less than 50 μm. The thickness of the samples is measured using the height adjustment of the same stage, with an uncertainty of 10 μm.

To prevent electrical contact to the chip carrier a thin piece of rolling paper is secured to the chip carrier base with a small amount of low temperature varnish-acetone mix, which then acts as a gentle adhesive layer to hold the sample and thermally anchor it to the chip carrier. Images of a sample after cutting, exfoliation, wiring and mounting in a chip carrier are shown in Figure 3.5b.

XRD of samples before and after this process confirms no deterioration of sample

quality, judged by the XRD peak width, from this processing. The finally ex-foliated surfaces of measured samples are typically exposed to atmosphere for ~ 2 hours during the final wiring step, and are otherwise kept under vacuum in a small vacuum chamber for drying the silver paint contacts, when not wiring they are kept in a desiccator.

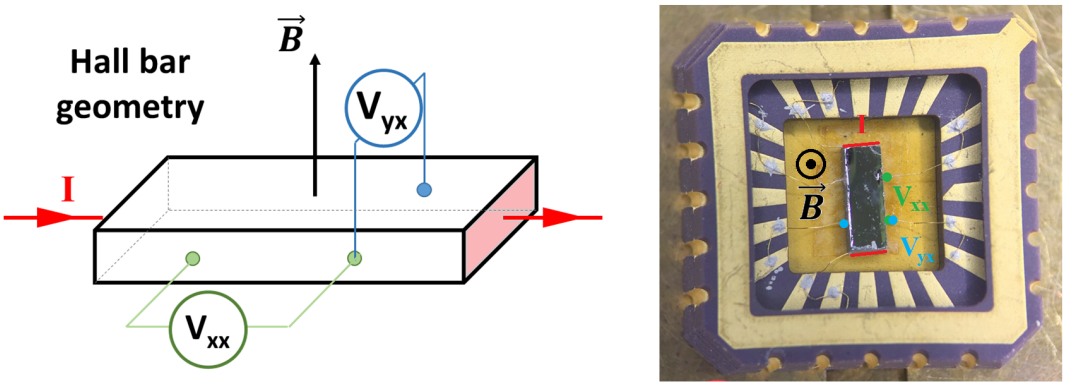

(a) (b)

Figure 3.5: (a) Schematic of the Hall bar geometry used to measure the electronic transport in Sb_2Te_3 single crystals. (b) Image of single crystal sample after preparation for transport measurements. Chip carrier sample area is 4 × 4 mm for reference. Highlighted contacts and labels show the Hall bar configuration.

Thin-Films

After the annealing procedure the thin films are typically 4 mm × 4 mm in lateral size, grown on a 0.5 mm thick substrate. Contacts are again made to the sample using Au wire and Ag paste, which are typically $\sim 1\ \Omega$. Samples are secured to the chip carriers using a small amount of low temperature varnish.

The Van der Pauw (VdP) geometry, shown in Figure 3.6, is used to measure the film's resistivity at room temperature and at 1.5 K to calculate the RRR, since any geometric effects will be removed [132, 133]. Two measurements for each side are taken with voltage and current lines swapped, these are then averaged and used to calculate the film resistivity following Ref. [133]. Thickness is taken from the XRR characterisation.

Hall measurements are also taken using the VdP geometry, but using a continuous

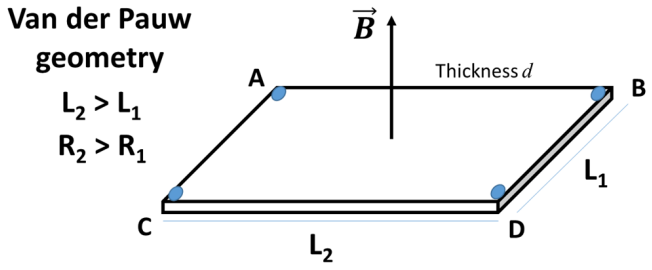

Figure 3.6: (a) Schematic of the Van der Pauw geometry used to measure the electronic transport in $RhPb_2$ thin films. Contacts are made to the film by Ag paste and Au wire.

AC current measurement with field swept to positive and negative values [132]. Current is applied across the sample diagonal (e.g. along CB) and voltage measured on the transverse contacts (e.g. over DA). The odd component of this voltage is again isolated to give the correct Hall resistivity. Switching current and voltage lines was found to give an identical Hall resistivity, since the samples are symmetric.

To speed up measurements of the resistivity dependence on temperature and field, two additional contacts are used between two corners, set in-line across the sample diagonal, to take an approximate 4-point measurement of the longitudinal resistivity. These give an incorrect measurement of the actual resistivity, however they correctly measure the RRR and MR%, confirmed through comparison to the full VdP measurement. These longitudinal 4-point measurements are multiplied by a geometric factor to make them identical to the VdP resistivity, and these are the measurements that are presented. In the thin film samples, we define the perpendicular MR for an out-of-plane B, transverse MR for in-plane B perpendicular to I, and longitudinal MR for in-plane B parallel to I.

A calibrated Cernox temperature sensor was mounted alongside the samples in each measurement run in order to measure the sample temperatures below 1.5 K, since in the ^{3}He system there is no in-built thermometry in the sample space. These were calibrated against a pre-calibrated Cernox obtained from Lakeshore Cryogenics, with resistances measured using a low-power AC resistance bridge.

3.3.3 Electrical Measurements

All measurements of sample voltage were carried out using a Keithley 6221 AC/DC current source. Voltage measurements at room temperature for initial characterisation of resistance are taken in DC mode using a Keithley 2182 nano-voltmeter. During dynamic measurements a sinusoidal AC waveform is applied constantly through the sample, and Stanford SR830 lock-in amplifiers were used to measure the voltage in AC mode. The frequency used in all measurements presented here was 117.66 Hz, which was selected to avoid interference from mains sources (50, 100 Hz) and reduce inductive effects: in all cases measurements are only undertaken if the out-of-phase voltage components are close to zero. Only the band-pass filters of the lock-in are used, since the 50 Hz and 100 Hz line filters affect the measurement at 117.66 Hz. The overall set-up of the measurement lines are also arranged to reduce external noise. Twisted pairs are always used for current lines and voltage measurement pairs, typical noise level is 20 nV for the AC measurement technique.

For these measurements Joule heating effects in the samples during measurement may be significant. The samples lateral sizes are large leading to reasonably low resistances in the both the single crystals and films, typically $\sim$ 50 mΩ and $\sim$ 0.5 Ω respectively. Power dissipation in single crystal samples measured with 1 mA current is $\sim$ 10 nW, producing negligible heating effects.

In the thin films studied in this thesis only the onset of superconducting transitions are found, typically showing a transition in resistance $<$ 0.2 mΩ. The transitions were first identified using continuous AC measurements and the offset-expand feature of the lock-in amplifiers, allowing small changes on a larger base-line voltage to be measured. The typical level of baseline noise in the AC voltage measurement is 20 nV: to achieve a signal to noise ratio of 10, a 1 mA current is required. The maximum power dissipation then is $\sim 10\mu$W in the thin films, which was seen to increase the sample temperature at the ^{3}He insert base temperature by $\sim$ 0.1 K over the course of $\sim$ 30 s where it then stabilised.

To ensure this heating effect did not change the measured superconducting properties, a measurement of the transition with a pulsed DC current was performed, where DC current is only applied for a short time during a voltage measurement, and then the current is left off for a longer delay time, minimising the heat load on the sample. Figure 3.7a compares a pulsed DC measurement with 1 mA, 25μs pulse width, and 0.1s

delay time, to a 1mA continuous AC measurement. The data presented for the DC measurements is an average of multiple measurement runs, interpolated and smoothed to remove noise. The superconducting transition is not affected seen by the excellent agreement by the two measurements. Since the thin-film samples resistances are typically similar, the slight heating effects are therefore taken as an acceptable condition for cleaner measurements across all samples, since they only affect the base-line temperature reachable in the ^{3}He system and not the sample properties.

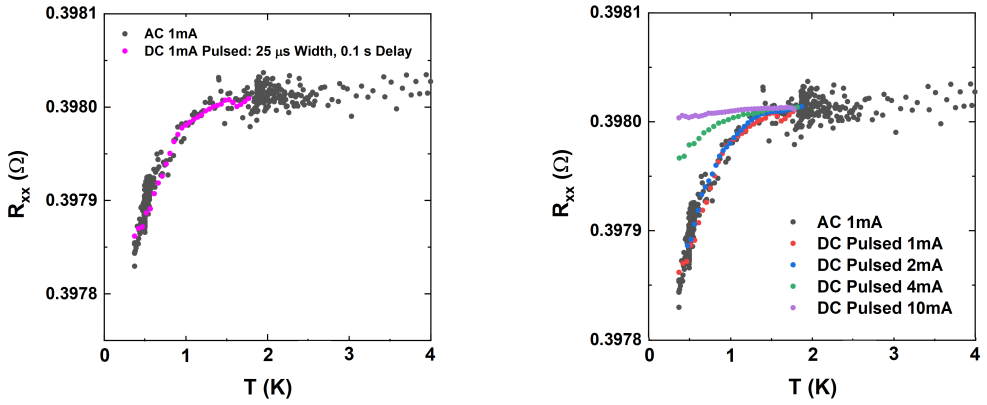

Figure 3.7: (a) For clean measurement of the small SC transitions in this work 1mA current is required, which is confirmed to produce no visible change on the SC transition through heating effects by comparison of DC pulsed and AC continuous measurement. (b) No intrinsic suppression of the SC transition is observed until 4 mA current in DC pulse mode, also confirming correct determination of the SC onset temperatures in measurements using 1 mA.

Apart from heating effects, the SC state is fundamentally sensitive to the application of a current, where ultimately the current destroys the superconducting state for some critical value I_c related to the critical field and the sample geometry [80]. To check whether the current is suppressing the SC behaviour observed in these thin films, Figure 3.7b compares the SC behaviour for various measurement currents in DC pulsed mode. Clearly, up to 2 mA there is no effect on the downturn, and again 1mA measurement current is determined to be a safe level for clean measurements.

3.3.4 Magnetotransport Effects

Resistivity Tensor

Following the relaxation-time approximation (Drude model), the equation of motion for a charge carrier q, with effective mass m^* and drift velocity $\boldsymbol{v}$, undergoing scattering events at rate τ, in the presence of both an electric $\boldsymbol{E}$ and magnetic $\boldsymbol{B}$ field, is given by [134, 135]:

$$m^* \left(\frac{d\boldsymbol{v}}{dt} + \frac{v}{\tau} \right) = q\boldsymbol{E} + q\left(\boldsymbol{v} \times \boldsymbol{B}\right) \tag{3.2}$$

For a planar sample with lateral dimensions in the x, y plane, with thickness t in the z direction, electric field $\boldsymbol{E} = (E_x, E_y, 0)$, current density $\boldsymbol{J} = (J_x, J_y, 0)$, defined as $\boldsymbol{J} = nq\boldsymbol{v}$ where n is the carrier density, with out of plane $\boldsymbol{B} = (0, 0, B)$, and taking the steady-state solution with $\frac{d\boldsymbol{v}}{dt} = 0$, we can re-express this as:

$$\boldsymbol{J} = nq\mu\boldsymbol{E} + \mu\left(\boldsymbol{J} \times \boldsymbol{B}\right) \tag{3.3}$$

$$\begin{pmatrix} J_x \\ J_y \end{pmatrix} = \begin{pmatrix} nq\mu E_x + \mu J_y B \\ nq\mu E_y + \mu J_x B \end{pmatrix} \tag{3.4}$$

where $\mu = q\tau/m^*$ is the charge carrier mobility. These equations can be decomposed into a matrix equation [135]:

$$\begin{pmatrix} J_x \\ J_y \end{pmatrix} = \frac{\sigma_0}{1+\mu^2 B^2} \begin{pmatrix} E_x + \mu B E_y \\ -\mu B E_x + E_y \end{pmatrix} = \frac{\sigma_0}{1+\mu^2 B^2} \begin{pmatrix} 1 & \mu B \\ -\mu B & 1 \end{pmatrix} \begin{pmatrix} E_x \\ E_y \end{pmatrix} \tag{3.5}$$

where $\sigma_0 = nq\mu = nq^2\tau/m^*$ is the Drude conductivity. From $\boldsymbol{J} = \sigma\boldsymbol{E}$ we can define the conductivity tensor as:

$$\overleftrightarrow{\boldsymbol{\sigma}} = \begin{pmatrix} \sigma_{xx} & \sigma_{xy} \\ \sigma_{yx} & \sigma_{yy} \end{pmatrix} = \frac{\sigma_0}{1+\mu^2 B^2} \begin{pmatrix} 1 & \mu B \\ -\mu B & 1 \end{pmatrix} \tag{3.6}$$

where $\sigma_{xx} = \sigma_{yy}$ and $\sigma_{yx} = -\sigma_{xy}$. Inverting the matrix to give the resistivity tensor:

$$\overleftrightarrow{\boldsymbol{\rho}} = \begin{pmatrix} \rho_{xx} & \rho_{xy} \\ \rho_{yx} & \rho_{yy} \end{pmatrix} = \frac{1}{\sigma_{xx}^2 + \sigma_{xy}^2} \begin{pmatrix} \sigma_{xx} & -\sigma_{xy} \\ \sigma_{xy} & \sigma_{xx} \end{pmatrix} = \rho_0 \begin{pmatrix} 1 & -\mu B \\ \mu B & 1 \end{pmatrix} \tag{3.7}$$

where $\rho_0 = 1/\sigma_0$. The usual expression for the Hall effect is contained here as $\rho_{yx} = \rho_0 \mu B = \frac{1}{nq} B = R_H B$, showing that the Lorentz force results in a linear Hall resistivity

dependence with field. From this, the origin of the MR is not simply due to the Lorentz force acting on charge carriers: in a free-electron model with a completely isotropic Fermi surface the MR should be zero [134, 136]. The origin of intrinsic MR is related to anisotropies in the carrier properties around the Fermi surface and formally the MR can be calculated based on the detailed conductivity tensor components calculated using the Boltzmann transport theory and knowledge of the Fermi surface shape [136].

Nevertheless, from equation 3.7 we have: $\rho_{xx} = \frac{\sigma_{xx}}{\sigma_{xx}^2+\sigma_{xy}^2}$, in metallic systems typically $\sigma_{xx} \gg \sigma_{xy}$ at low field and $\rho_{xx} \approx \frac{1}{\sigma_{xx}} \approx \rho_0 \left(1 + \mu^2 B^2\right)$, revealing the well known B^2 power law dependence of the MR [134].

Multiple Bands

As explored in the introduction, many non-trivial topological materials have complicated Fermi surfaces with multiple branches of partially occupied bands. Overall, the response of each band combines to give the total current density: $\boldsymbol{J}_T = \sum_n \boldsymbol{J}_n = \sum_n \overleftrightarrow{\rho_n}^{-1} \boldsymbol{E}$, leading to the definition: $\sum_n \overleftrightarrow{\rho_n}^{-1} = \overleftrightarrow{\rho}^{-1}$.

Using this definition and the inversion of a single band resistivity tensor [47]:

$$\overleftrightarrow{\rho}_n = \begin{pmatrix} \rho_n & -R_n B \\ R_n B & \rho_n \end{pmatrix} \longrightarrow \overleftrightarrow{\rho}_n^{-1} = \frac{1}{\rho_n^2 + R_n^2 B^2} \begin{pmatrix} \rho_n & R_n B \\ -R_n B & \rho_n \end{pmatrix} \tag{3.8}$$

leads to a set of equations for two dominant transport bands:

$$\frac{\rho}{\rho^2 + R^2 B^2} = \frac{\rho_1}{\rho_1^2 + R_1^2 B^2} + \frac{\rho_2}{\rho_2^2 + R_2^2 B^2} \tag{3.9}$$

$$\frac{R}{\rho^2 + R^2 B^2} = \frac{R_1}{\rho_1^2 + R_1^2 B^2} + \frac{R_2}{\rho_2^2 + R_2^2 B^2} \tag{3.10}$$

which, after some arithmetic, lead to expressions describing the Hall and MR in a system with two dominant transport bands:

$$\rho_{yx}(B) = \frac{(R_1\rho_2^2 + R_2\rho_1^2)B + R_1 R_2 (R_1 + R_2) B^3}{(\rho_1 + \rho_2)^2 + (R_1 + R_2)^2 B^2} \tag{3.11}$$

$$\rho_{xx}(B) = \frac{\rho_1\rho_2(\rho_1 + \rho_2) + (\rho_1 R_2^2 + \rho_2 R_1^2) B^2}{(\rho_1 + \rho_2)^2 + (R_1 + R_2)^2 B^2} \tag{3.12}$$

which are often applied to TI materials with one band arising from bulk carriers, and the other from surface carriers [44].

Importantly, the qualitative behaviour of the 2-band Hall effect shows an explicit non-linear dependence on field, compared to the linear dependence for a single-band

model. The qualitative behaviour of the MR in a 2-band material is the same as that of a single band material, both showing saturation provided there is no compensation between carrier populations where instead the MR will continue to grow with B^2 [47, 134, 135]. The existence of multiple band transport and the requirement for the associated fitting is therefore indicated by a non-linear Hall resistivity in a non-magnetic material.

These equations are directly fitted to the measured $\rho_{yx}(B)$ and $\rho_{xx}(B)$ data. Sweeping to positive and negative field allows the data to be decomposed into even and odd components, separating out any cross-talk artefacts related to contact misalignment, since $\rho_{yx}(B)$ is odd in field and $\rho_{xx}(B)$ even. Since the single band Hall resistivity is captured correctly by the free-electron model, but the single band MR is not, it is expected that this free-electron like 2-band Hall effect will provide more reliable information regarding the carrier properties after fitting compared to the MR.

In general, there may be higher numbers of bands contributing to the transport, the three-band form of the Hall resistivity is derived following the same method as above:

$$\rho_{yx}(B) = \frac{\begin{array}{c} B^2 R_1 R_2 R_3 \\ +B[R_1p_2p_3+R_2p_1p_3+R_3p_1p_2]\left[p_1p_2+p_1p_3+p_2p_3-B^2(R_1R_2+R_1R_3+R_2R_3)\right] \\ -B[p_1(R_2+R_3)+p_2(R_1+R_3)+p_3(R_2+R_1)]\left[p_1p_2p_3-B^2(p_1R_2R_3+p_2R_1R_3+p_3R_1R_2)\right] \end{array}}{\left[p_1p_2+p_1p_3+p_2p_3-B^2(R_1R_2+R_1R_3+R_2R_3)\right]^2+B^2[p_1(R_2+R_3)+p_2(R_1+R_3)+p_3(R_1+R_2)]^2} \tag{3.13}$$

as it is later applied to Sb_2Te_3.

Shubnikov de Haas Oscillations

With increasing magnetic field strength, the charge carriers will complete circular cyclotron orbits in a plane perpendicular to the applied field. With increasing B the radius of the charge carrier orbits will decrease, and the cyclotron frequency will increase. At high enough fields ($\mu B \gg 1$) and at low enough temperatures ($\hbar\omega_c \gg k_B T$), the cyclotron orbit radius will reduce to less than the average scattering length, and the charge carriers will be able to complete many cyclotron orbits before scattering. In momentum space, the charge carriers are completing many orbits around the Fermi surface without scattering, leading to a periodic boundary conditions on the electron wave function, and accordingly the emergence of quantum effects.

Specifically, the Schrödinger equation for the charge carriers resembles that of a

quantum harmonic oscillator, and the energy spectrum of the electrons becomes quantised into Landau levels with index n, here with B applied along the z-axis [78]:

$$E = \hbar\omega_c \left(n + \frac{1}{2}\right) + \frac{\hbar k_z^2}{2m^*} \tag{3.14}$$

The quantization of the energy means that the only permitted electronic states lie on Landau tubes in k-space, defined by an area a, whose actual cross section for fixed n depends on the energy of the Fermi surface ϵ and k_z:

$$a(\epsilon, k_z) = \left(n + \frac{1}{2}\right) \frac{2\pi e B}{\hbar} \tag{3.15}$$

as shown for a spherical Fermi surface in Figure 3.8a.

As B is increased the tubes radii increase and the occupied length of the tube shrinks, eventually vanishing completely when $a = S$, the extremal cross sectional area of the Fermi surface. This happens periodically as tubes with smaller n pass through the edge of the Fermi surface, shown schematically in Figure 3.8b for the value of k_z corresponding to S. This vanishing is periodic in intervals of $1/B$:

$$\Delta\left(\frac{1}{B}\right) = \frac{2\pi e}{\hbar S} \tag{3.16}$$

or with frequency:

$$F = \left(\Delta\left(\frac{1}{B}\right)\right)^{-1} = S\frac{\hbar}{2\pi e} \tag{3.17}$$

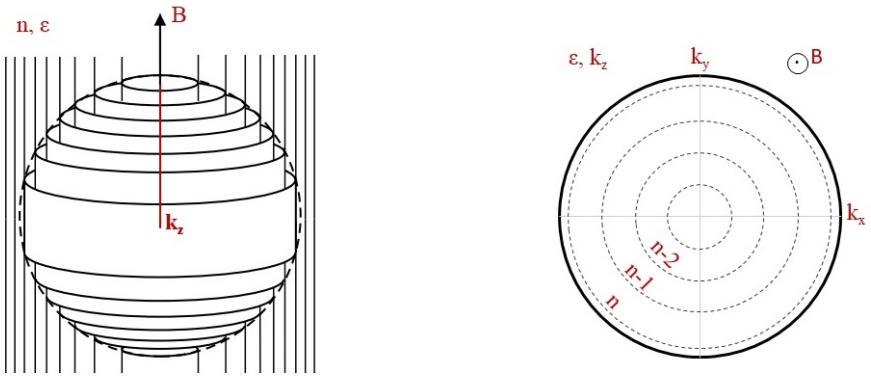

(a) (b)

Figure 3.8: (a) Electrons completing cyclotron orbits have quantized k-space orbit areas in the direction perpendicular to the applied field, known as Landau tubes. Figure adapted from [78]. (b) As the field is increased the tube radius increases and they periodically vanish at the extremal cross sectional area of the Fermi surface, meaning there is a periodic change in the density of states at the Fermi level. For fixed k_z, corresponding to the maximal area S of the Fermi surface ϵ, this periodic change is due to tubes of different Landau level index n passing through the edge of the Fermi surface.

Since the Landau tubes represent the only allowed states for electrons there is a sharp change in the density of states at the chemical potential each time a tube crosses it, and accordingly changes in many of the physical properties of a system are expected. In particular here we are interested in oscillations of the conductivity described by the Lifshitz-Kosevich (LK) theory [44, 78, 137, 138]:

$$\frac{\Delta\sigma_{xx}}{\sigma_{xx}} = AB^{1/2}\cos\left[2\pi\left(\frac{F}{B} - \frac{1}{2} + \beta\right)\right] \tag{3.18}$$

where β is a phase offset related to the Berry phase, which is determined by the nature of the band dispersion [54–56]. The amplitude A of the oscillations is related to the maximal CSA and the Fermi surface curvature in the field direction, and various reduction factors:

$$A = A_0\left(S\frac{\partial^2 S}{\partial k_{\|B}^2}\right)^{-1/2} R_T R_D R_S \tag{3.19}$$

where R_T, R_D, and R_S are temperature, Dingle and spin reduction factors respectively. The second derivative summaries the amplitude dependence on the Fermi surface

curvature which is fixed for each SdHO branch and so absorbed into A_0 during fitting, R_S is also fixed for each SdHO branch so is also absorbed into A_0 during fitting [78].

Temperatures cause a smearing out of the Landau levels, reducing the abruptness of the change in the density of states and so the SdHO amplitude [78]:

$$R_T = \frac{\chi}{\sinh \chi} \tag{3.20}$$

with $\chi = 2\pi^2 \left(\frac{k_B T}{\hbar \omega_c}\right)$, meaning the temperature dependence of the SdHO amplitude can be used to extract the cyclotron mass m_c in $\omega_c = eB/m_c$.

Finite scattering times also cause some smearing of the Landau levels by the uncertainty principle, described by the Dingle term [78]:

$$R_D = \exp\left[-2\pi^2 \left(\frac{k_B T_D}{\hbar \omega_c}\right)\right] \tag{3.21}$$

causing an exponential amplitude growth with field, characterised by the Dingle temperature:

$$T_D = \frac{\hbar}{2\pi k_B \tau_D} = \frac{e\hbar}{2\pi k_B m_c \mu_D} \tag{3.22}$$

which allows calculation of μ_D once m_c is known.

Structural inhomogeneity, such as micro-strains, reduce the SdHO amplitude by causing low angle scattering which affects the single-particle relaxation time and μ_D, but not the Drude scattering time and Hall mobility [64, 78, 139]. The effect can be summarised as a multiplicative factor (>1) in front of T_D which is difficult to extract separately [78], but can give a qualitative indication of sample quality in a series with similar Hall mobilities.

Clearly, many useful parameters can be extracted after observation of SdHO. The main analysis procedure in this work is comprised of isolating the SdHO envelope from a measured resistivity, determining the Frequency F by a Fourier Transform, then directly fitting equation 3.18 to the data to determine the exponential decay rate related to T_D, and the phase offset β related to the Berry phase of the carriers. Separately, fitting the R_T term to the temperature dependence of the FFT, and so SdHO, amplitude is used determine the cyclotron mass of the carriers m_c.

Careful consideration of the application of this equation is required, since the SdHO are measured in the resistivity. We note that, depending on the relative magnitudes of σ_{xx} and σ_{xy} in equation 3.7, we may have either $\frac{\Delta\rho_{xx}}{\rho_{xx}} \approx \frac{\Delta\sigma_{xx}}{\sigma_{xx}}$ for $\sigma_{xy} \gg \sigma_{xx}$, allowing direct application of equation 3.18 to the resistivity, or $\frac{\Delta\rho_{xx}}{\rho_{xx}} \approx \frac{-\Delta\sigma_{xx}}{\sigma_{xx}}$ for $\sigma_{xy} \ll \sigma_{xx}$.

For the Sb_2Te_3 samples in this work $\sigma_{xx} \sim \sigma_{xy}$ and no unanimous simplifications are found: there is usually some transition between the two regimes across the SdHO envelope, moving to $\frac{\Delta\rho_{xx}}{\rho_{xx}} \approx \frac{\Delta\sigma_{xx}}{\sigma_{xx}}$ at high field ($B \geq 4$ T) when $\sigma_{xy} \gg \sigma_{xx}$. To reliably determine the SdHO phase offsets which are a key indication of the Dirac nature of carriers, we only consider the regions of the SdHO at high field where $\frac{\Delta\rho_{xx}}{\rho_{xx}} \approx \frac{\Delta\sigma_{xx}}{\sigma_{xx}}$ and equation 3.18 can be directly applied.

Also, an equivalent equation for SdHO oscillations in σ_{xy} is defined with the same form as that for those in σ_{xx}, with the possibility of a sign change, mapping for example, a peak in σ_{xx} to a trough in σ_{xy} [138, 140]. In fact, this depends on the charge carrier type: a maximum in σ_{xx} will correspond to a minimum in σ_{xy} for hole carriers, and a maximum for electron carriers [141]. To uncover this information from the SdHO the same fitting procedure is used on SdHO isolated from ρ_{yx} to compare the relative phase of the oscillations and whether electron or hole carriers are responsible. Again, it is found that $\frac{\Delta\rho_{yx}}{\rho_{yx}} \approx \frac{\Delta\sigma_{xy}}{\sigma_{xy}}$ at high-field and only this region is fitted for reliability.

For multiple bands, the amplitude of the SdHO also depends on the scale of the contribution of the individual band to the total transport [78]. Overall, the separate contributions from different Fermi surface branches can be treated independently from one another [78, 142] so that complicated SdHO envelopes can be fit with a linear combination of equations of the form 3.18.

Chapter 4

Antimony Telluride

4.1 Introduction

Antimony Telluride (Sb_2Te_3) makes up the second generation of TI materials with other quintuple-layered chalcogenide material family members Bismuth Selenide and Bismuth Telluride. The non-trivial TI phase in these materials arises from the spin-orbit induced band crossing of opposite parity orbitals at the Γ point in the Brillouin Zone, resulting in a singular Dirac cone on the hexagonal (001) mirror-like cleavage surface.[4, 60] Intriguingly, two more sets of surface states have been identified in Sb_2Te_3: intrinsic Rashba spin-orbit split surface bands extending from 300 to 750 meV below the valence band edge exist within a partial valence band gap, that are protected by a spin-orbit gap between opposite parity bulk bands;[18–21] and some topologically trivial states 600 meV above the Dirac point.[143] To our knowledge Sb_2Te_3 is the only TI material with observed intrinsic Rashba-split surface states co-existing with the topological Dirac surface states, though the Hamiltonian describing the bulk states of all the chalcogenide family members displays degenerate Rashba-like spin texture,[4, 23, 48] meaning intrinsic Rashba spin-split surface bands could be ubiquitous across the material family.

In Sb_2Te_3 the scale of the Rashba splitting: $\Delta E = \alpha k_{\parallel}$, characterised by Rashba coefficient α for momentum parallel to the surface $k_{\parallel}$; is larger ($\alpha = -1.4$eVÅ) than that observed in typical metallic Rashba systems e.g. Bi(111) and Au(111) surfaces [19], with similar magnitude to that found in a confined 2 dimensional electron gas (2DEG) created by band bending near the surface of Bi_2Se_3 [144], and larger than that typically observed in other 2DEG systems expected to find use in spintronics applications [145–148]. Coupled with the ability to tune the chemical potential position, altering the degree of spin accumulation through the Rashba-Edelstein effect, Sb_2Te_3 emerges as a promising base for investigating spin-orbit torque magnetisation switching devices [149] [150].

As well as this, the high mobility of the surface states and the existence of intrinsic Rashba states highlights Sb_2Te_3 as a candidate for switch-able spin-polarised transport devices. Roughly, the mean-free-path of a carrier on the surface with mobility $\sim 2.5 \times 10^4$ cm^2/Vs and $k_F \sim 0.1$ Å^{-1} is estimated to be ~ 1 μm. The existence of a second surface band with Rashba splitting also contributes to this ability [16, 151], and a system with Dirac and Rashba bands clearly separated in energy provides a good platform for being able to tune between these two regimes.

Sb_2Te_3 is usually heavily hole doped and previous observations of SdHO have found

that bulk carriers from multiple valence bands can contribute to the transport with p $\approx 10^{20}$ cm^{-3}, the typical carrier density for nominally stoichiometric samples, which should also place the chemical potential close to the intrinsic Rashba surface states.[152, 153] With reduced carrier densities (p $\approx 10^{18}$ cm^{-3}) in vapour-transport grown samples contributions to the transport have been identified from a novel 2DEG in the material, which are facilitated by an extremely high mobility of 2.5 $\times 10^4$ cm^2/Vs, where a novel superconducting phase also emerges.[17] So far no systematic studies of the transport behaviour between these two regimes exists, and given the existence of multiple surface bands of interest it is important to characterise the material in detail before pursuing further applications of the novel surface states.

To better understand the material system and probe for contributions to the transport from the surface states, the magneto-transport of (001) oriented single crystal Sb_2Te_3 grown with carrier densities in the range 2.4 - 11.5 $\times$ 10^{19} cm^{-3} is studied. For the first time the electrical transport is explained using a two-carrier band model, which uncovers contributions from both hole and electron bands, and clear SdHO are resolved across the carrier density range. The convolution of different frequency SdHO cause novel beating envelopes for samples with reduced carrier densities, and fitting the SdHO uncovers non-trivial Berry phases for carrier densities in the range 4.1 - 7.9 $\times$ 10^{19} cm^{-3}. Naively, the emergence and extinction of a non-trivial Berry phase in this material with decreasing carrier density may be interpreted as tuning the chemical potential through the band region of the Rashba surface states, where they would contribute significantly to the surface transport. However, detailed consideration of the SdHO instead points away from either the Rashba or Dirac surface bands being responsible for the non-trivial phase, and instead, a region of linearly dispersive Dirac-like bulk states in the upper valence band is found responsible for the non-trivial Berry phase and SdHO beats.[54–56, 79]

This work adds a Dirac semi-metal bulk phase to the phenomena present in Sb_2Te_3 and displays the ability to tune the chemical potential from a regime of dominant Rashba surface states to dominant Dirac bulk states. It is expected that bulk contributions to the transport are still too high to observe the surface states at present, and reducing the thickness of Sb_2Te_3 samples studied will be required to keep the chemical potential in the appropriate region for both sets of surface states to be accessed through transport experiments.

4.2 Material Growth and Structural Parameters

Based on previous studies of the nature of the intrinsic defects in Sb_2Te_3, excess Te is incorporated during the melt growth to suppress the formation of Te vacancies and the subsequent Sb on Te anti-site defects which give rise to the high carrier densities in Sb_2Te_3 [62, 154–156]. In the conventional Kröner-Vink defect notation, we have double negatively charged Te vacancies denoted by $V_{Te}^{\cdot\cdot}$; and singly positively charged Sb on Te anti-site defects denoted by Sb_{Te}'.

Cation vacancies are a common problem in this material family, which is due to the low boiling points and so high vapour pressures during growth, reducing the Te/Se content in the melt.[62] Sb_2Te_3 then also suffers from high numbers of anti-site defects due to the similar electro-negativity and atomic radius of Sb and Te, which allows Sb to easily enter the vacant Te site.[157]

Similar methods using excess Se/Te were used with Bi_2Se_3 and Bi_2Te_3 in the early days of TI research in attempts to reduce the bulk carrier contribution to the transport and observe the topological surface states in transport measurements,[63] where it was soon discovered that mixed crystals of the BSTS type were more effective in controlling the carrier density and observing the Dirac surface states.[67] This study uses non-alloyed Sb_2Te_3 to avoid any complications with altering the band structure since despite the shared bulk Rashba-like Hamiltonian across the material family, it remains unclear how the intrinsic Rashba surface states would be altered in Sb_2Te_3 with alloying. Doping has also been employed in the Sb_2Te_3 system previously, where substitution of Sb for a more electronegative element can effectively reduce the carrier density by reducing the number of anti-site defects.[157] It is avoided here since the charged dopant atoms act as scattering sites for the charge carriers, reducing their mobility and making SdHO harder to observe from either bulk states or the surface states of interest.

The combined effects of higher Te vapour pressure from the excess Te and a Te-rich solute are expected to reduce the number of Te vacancies in the forming crystal and therefore reduce the number of vacant Te sites available for Sb to enter, in-line with defect formation energy calculations.[158] A range of nominally super-stoichiometric Te content from 5% atomic excess up to 50% is used, with the expectation that most of this will not enter into the final single crystal segments since the usual deficiency is $\approx$ 0.7%, corresponding to Te = 2.98.[17] In total 7 separate growth runs were performed

with nominal Te concentrations of: 3.00, 3.10, 3.16, 3.29, 3.43, 3.89, and 4.52. Details of the modified Bridgman growth method are found in Chapter 3.

Figure 4.1 shows the XRD patterns for cleaved single crystal segments of each composition, all displaying the expected (0 0 3l) XRD peaks for single crystal Sb_2Te_3 aligned to the mirror plane. Peaks are shifted upwards with increasing nominal composition for clarity, and are normalised to the strongest XRD peak for the (0 0 15) peak close to 45 degrees. No additional peaks from Te impurity phases are found.

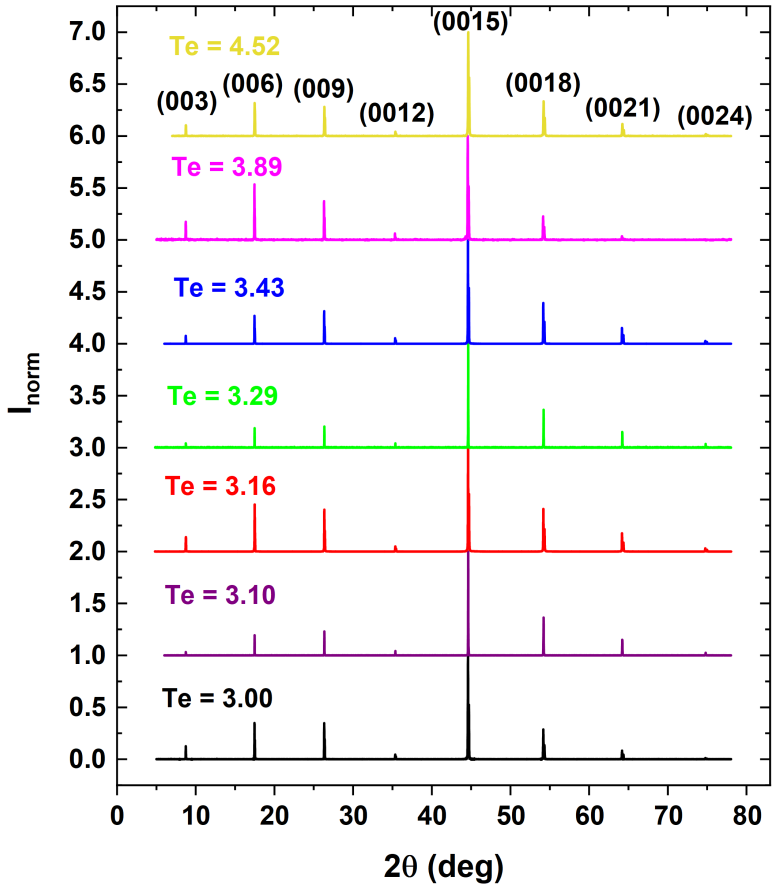

Figure 4.1: XRD patterns for increasing nominal concentration of Te. Each scan is normalised to the highest intensity peak close to 45 degrees, and data sets are shifted upwards with increasing Te content for clarity. Diffraction peaks are labelled with the (003l) index for single crystal Sb_2Te_3.

A schematic of the hexagonal-rhombohedral unit cell of Sb_2Te_3 (space group $R\bar{3}m$)

is shown in Figure 4.2a. It is made up of 3 quintuple layered units of atomic layers of Te-Sb-Te-Sb-Te, where each of the quintuple layer units is connected by a Van der Waals (VdW) gap. The crystals are easily separated along the VdW gap cleavage plane, revealing the mirror-like *ab*-plane, which has the *c*-axis pointing perpendicularly out of it.

Figure 4.2b(i) summarises the *c*-axis values extracted from the strongest (0 0 15) peak, finding an almost constant value across the composition range (mean $c = 30.454 \pm 0.003$Å) in agreement with that found previously [159, 160]. The constant c-axis suggests that the incorporated Te not entered into the Van der Waals gap, where an extension of the *c*-axis would be expected [161].

Figure 4.2b(ii) shows the full width at half maximum (FWHM) of the dominant (0 0 15) peak for each sample, showing an approximately constant value for Te < 3.43, and a slight increase for the samples with higher nominal Te content. Data is presented only for samples measured with the same x-ray beam collimation.

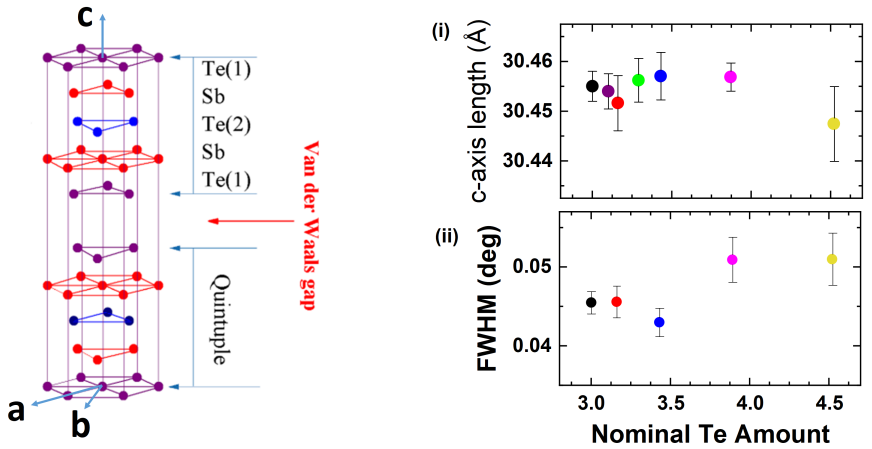

(a) (b)

Figure 4.2: (a) The hexagonal unit cell of Sb_2Te_3, highlighting the quintuple layers and Van der Waals gap cleavage plane. Adpated from [162]. (b)(i) Hexagonal unit cell *c*-axis values extracted from the (0 0 15) XRD peak, shown to stay approximately constant across the nominal composition range. (b)(ii) XRD peak FWHM extracted from the (0 0 15) peak, only for samples measured using the same x-ray beam collimation, showing a slight increase for samples with high nominal Te concentration.

As mentioned, the nominal amount of Te is much higher than the actual deficiency in the formed single crystal. We reiterate that there is no change in the single crystal segments c-axis value, and no Te impurity phases are observed in the single crystal segments, suggesting that the excess Te that is not incorporated into the vacant sites of the single crystal Sb_2Te_3 does not end up elsewhere in the single crystals studied, and resides in a different part of the growth ingot. For example, most of the nominal excess Te that is not incorporated into the single crystal may have segregated to the grain boundaries of polycrystalline regions of the growth ingot [163].

Overall the single crystal segments all show single phase with good crystalline quality and a consistent structure across the composition range. The amount of extra Te inclusion in the grown crystals due to the nominal excess has not been measured. Analysis methods such as energy-dispersive x-ray spectroscopy could provide information regarding the exact chemical composition [164]. Structural refinement using the measured XRD patterns can also provide more information regarding the Sb or Te site occupation and how this is affected by the nominal excess of Te [165].

The success of the additional Te in reducing the number of Te vacancies and Sb_{Te} defects in the single crystals is inferred by measuring the electrical transport properties of the samples in the next section.

4.3 Electronic Transport Measurements

This section discusses the electronic characterisation of the Sb_2Te_3 samples grown, in order to judge the success of excess Te in reducing the bulk carrier densities. Initially from the Hall effect measurements, it is found that the system is well described by a two-band transport model comprised of a majority hole and minority electron band. The validity and self-consistency of the model are discussed, where the measured out-of-plane MR is found consistent with the model parameters.

4.3.1 Transport Characterisation

First, the resistivity dependence on temperature for all compositions is shown in Figure 4.3a. Metallic behaviour is found for all suggesting bulk carrier densities have remained high, or Sb_2Te_3 has remained a degenerately doped semi-conductor system and the chemical potential still resides somewhere in the bulk valence bands. No par-

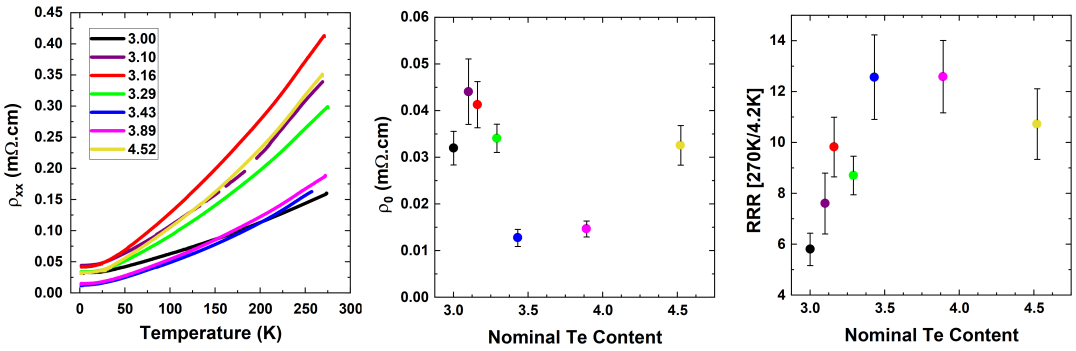

(a) (b) (c)

Figure 4.3: (a) Resistance dependence on temperature indicates a degenerately doped semiconductor system with metallic like behaviour, suggesting the carrier densities have remained high and the chemical potential resides in the valence bands. (b) Variance in ρ_0 with nominal composition. (c) Variance of RRR calculated from the values of ρ_{xx} at 270 K and 4.2 K.

tial freeze out of carriers indicating semi-conducting behaviour is observed. Figure 4.3b shows the dependence of the residual resistivity ρ_0 on the nominal composition, and Figure 4.3c shows significant changes in the RRR across the composition range. The usual expectation for metallic systems of higher structural quality producing lower residual resistivity and a higher RRR does not apply in systems like Sb_2Te_3, since it should formally be a semi-conductor and the persistent free carriers arise from the aforementioned point defects in the lattice, leading to a complicated dependence of ρ_0 and RRR on structural quality.

To uncover the effects of the nominal excess of Te on the transport, the magneto-transport of the single-crystals are studied. Here, current is applied in-plane and the magnetic field applied perpendicularly out of the plane of the samples, parallel to the hexagonal c-axis. Misalignment to the field is confirmed to be less than 1 degree in all cases by measuring the height profile of the top sample surface, using the optical microscope method described in Chapter 3.

Figure 4.4a shows the Hall resistivity taken at 1.5 K, where a clear non-linear dependence with field is found indicating multiple carrier band transport, shown more clearly in the inset [47]. Figure 4.4b shows the MR taken at 1.5 K, displaying quadratic low-field response that begins approaching some saturation value in the high-field limit,

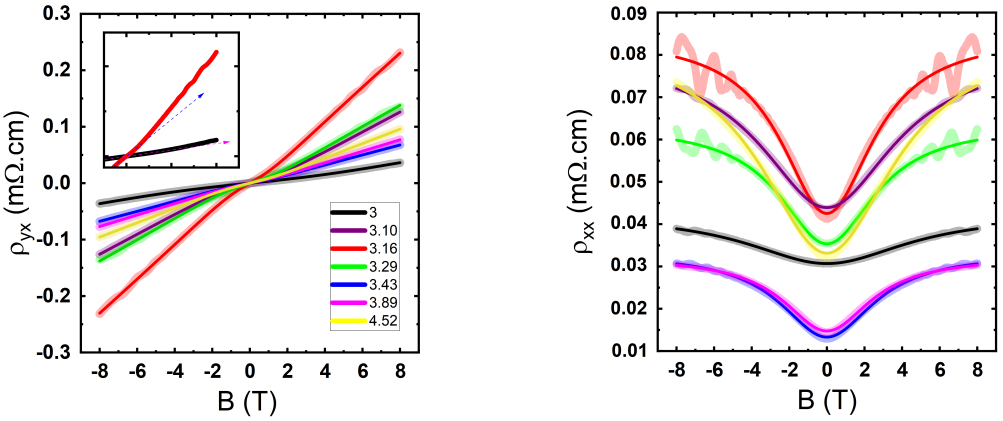

(a) (b)

Figure 4.4: (a) Hall resistivity measured at 1.5 K shows a clear non-linearity with field for all compositions, which is a signature of multiple-band transport in non-magnetic systems. Inset shows deviation from low-field linear slope for largest and smallest Hall resistivity. (b) The MR measured at 1.5 K shows quadratic low-field behaviour and tends towards saturation at higher fields, with clear SdHO. Solid lines are the fitted curves of the two-band magnetotransport equations.

which is an indication of closed carrier orbits in-plane parallel to the current direction, and may arise from single or multiple band transport in an uncompensated system [47]. Clear SdHO are visible in ρ_{xx} for all compositions, and are visible in ρ_{yx} for some compositions, these are discussed in detail later.

As discussed in Chapter 3, the non-linear dependence on field is the key indication of the requirement for a multiple-band transport model, since the single-band Hall resistivity only scales linearly with field. Here, there is a transition from a shallower linear low field slope to a steeper linear high field slope in all compositions: this shape non-linear Hall resistivity has been observed in single crystal Sb_2Te_3 previously [17, 166, 167] and has not, to our knowledge, been explained in a multiple band transport model.

4.3.2 Multiple-Band Transport

The number of inflections and zero-crossings can broadly suggest the number of transport bands, for example finding only two regimes of linear gradient in many of the TI

materials with a single bulk transport band and single surface band [16, 67, 168], and finding three inflections and two zero-crossings in ZrSiS where three or more bands may contribute [169]. The balance of band parameters has a large effect on the true shape of the Hall resistivity however and there is no concrete rule: in this instance, with only one inflection for each field branch and the only zero crossing at $B = 0$ T, the form of the measured data suggests that there are two-bands dominating the Hall effect.

Following this, the bold lines in Figure 4.4 are the results from fitting the two-band transport equations introduced in Chapter 3. For the Hall resistivity the fitting is only accepted if the determined carrier parameters reproduce the measured value of the longitudinal resistivity at zero field at 1.5 K, using $\left(\sum_n \overleftrightarrow{\rho_n}^{-1}\right)^{-1}$ [44], ensuring the reliability of the determined parameters.

Focussing first on the Hall data, the standard 2-band equation fits the data well across the composition range and uncovers contributions to the transport from both hole and electron carriers. For the nominally stoichiometric sample there is majority p-type band with 1.2 $\times$ 10^{20} cm^{-3} carrier density and a minority n-type band with 2.7 $\times$ 10^{19} cm^{-3}. This is surprising given the chemical potential resides in the valence band of Sb_2Te_3. The fitting reveals similar mobilities to that in previous work for nominally stoichiometric single crystal Sb_2Te_3 (1500 cm^2/Vs) where p-type carrier densities are also typically quoted as $\approx 10^{20}$ cm^{-3}.[152, 153, 170]

To check the possibility of a third transport band, fitting is also performed with the three-band form of the Hall resistivity, derived following the same methods to give the two-band model in Chapter 3. In both the stoichiometric and Te = 3.16 samples, two of the bands are found to have identical parameters to those from the two-band fitting, and a third band is found to have $p \sim 10^{19}$ cm^{-3} with extremely low mobility $\mu \sim 0.1$ cm^2/Vs, most likely meaning a non-physical band and that the three-band fitting is converging to the two-band case.

Considering the hole and electron bands found, the same direction of inflection of Hall signal from shallow to steeper at higher field is observed in WTe_2 but with overall different sign, which has a majority electron band with minority hole carriers confirmed by transport and ARPES [171, 172]. This suggests that two bands of opposing carrier charge exist in the material and the fitting is reliable. It is also possible to show analytically, using the limiting cases of the standard 2-band model in high and low field, that the increase in slope from low to high field can only be explained with hole

and electron bands and not two bands of the same carrier type.

The composition dependence of the carrier properties determined from the Hall effect are shown in Figure 4.5. Clearly, the additional Te incorporated in the growth gives notable reductions in the carrier densities and increases mobilities respectively, the largest changes seen for the samples grown with up to 10% atomic excess Te. There is an order of magnitude decrease in the majority p-type carrier density for $3.10 \leqslant \text{Te} \leqslant 3.29$ to $\approx 3 \times 10^{19}$ cm^{-3} and on average a slight reduction for higher Te content to $\approx 7 \times 10^{19}$ cm^{-3}. A similar trend is found for the minority n-type band in Figure 4.5c where samples with $3.10 \leqslant \text{Te} \leqslant 3.29$ have the lowest carrier densities of $\approx 3 \times 10^{18}$ cm^{-3}, with an average value of 7×10^{18} cm^{-3} for higher Te content. Figures 4.5b and 4.5d show a 2 - 4 fold increase in the mobility of both bands for all compositions compared to nominally stoichiometric Sb_2Te_3, it increasing on average to 5000 cm^2/Vs with some scatter across compositions.

Importantly, the determination of majority hole and minority electron bands is confirmed in all compositions, and there has been a successful reduction in the bulk carrier density by the inclusion of excess Te, finding an optimum nominal composition close to Te = 3.16. Also, as is explored in more detail later, the range of carrier densities found allow a detailed investigation of the electronic band structure, using the SdHO as an indication of the changing nature of the electronic states. First, the self-consistency of the two-band model is explored by checking whether the other transport properties can be accounted for.

4.3.3 Self-Consistent Semi-metallic Two-Band Transport

As shown already in Figure 4.4b, the observed MR can also be accounted for by the two-band model. The background MR found for all samples is a quadratic low-field response that begins approaching some saturation value in the high-field limit. Generally this behaviour is expected for single or multiple band materials with closed Fermi branches in the current direction, or in two-band materials without electron-hole compensation [47]. Fitting to the two-band model captures the saturating MR for all samples and also reveals a majority hole and minority electron band across the composition range.

Somewhat surprisingly given that the MR should depend on detailed consideration of Fermi surface anisotropies [134, 136], and the two-band model derived assumes isotropic Fermi surfaces, the changes in MR% also seem to be broadly consistent with the

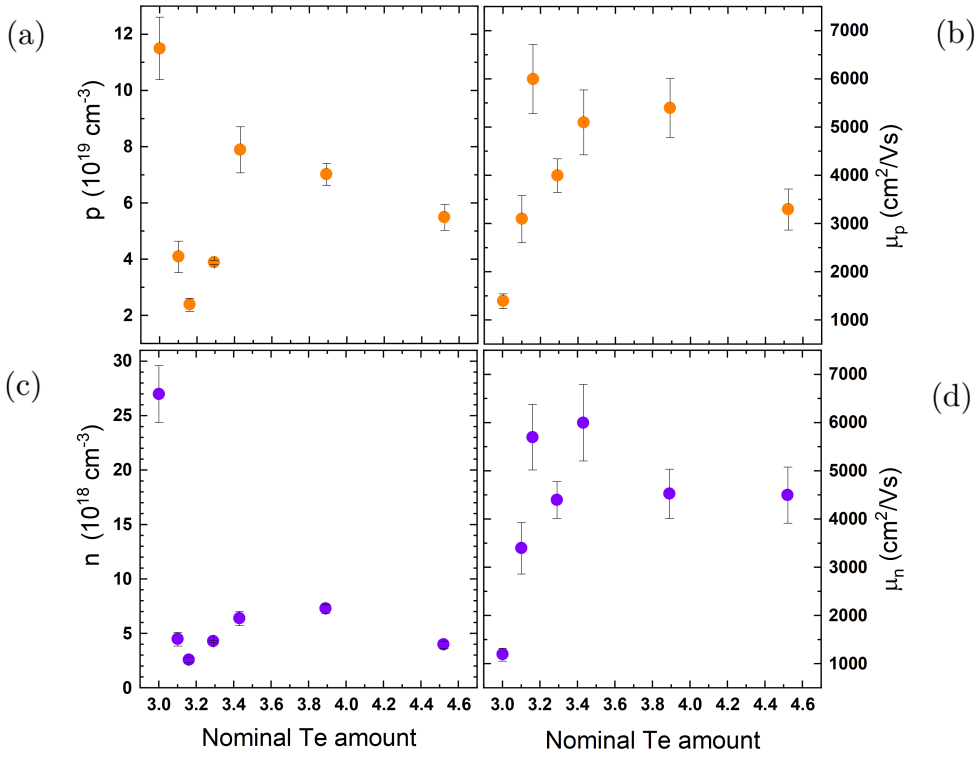

Figure 4.5: Composition dependence of the transport parameters determined from the 2-band fitting to the Hall data. (a) p-type carrier density, (b) p-type carrier mobility, (c) n-type carrier density, (d) n-type carrier mobility.

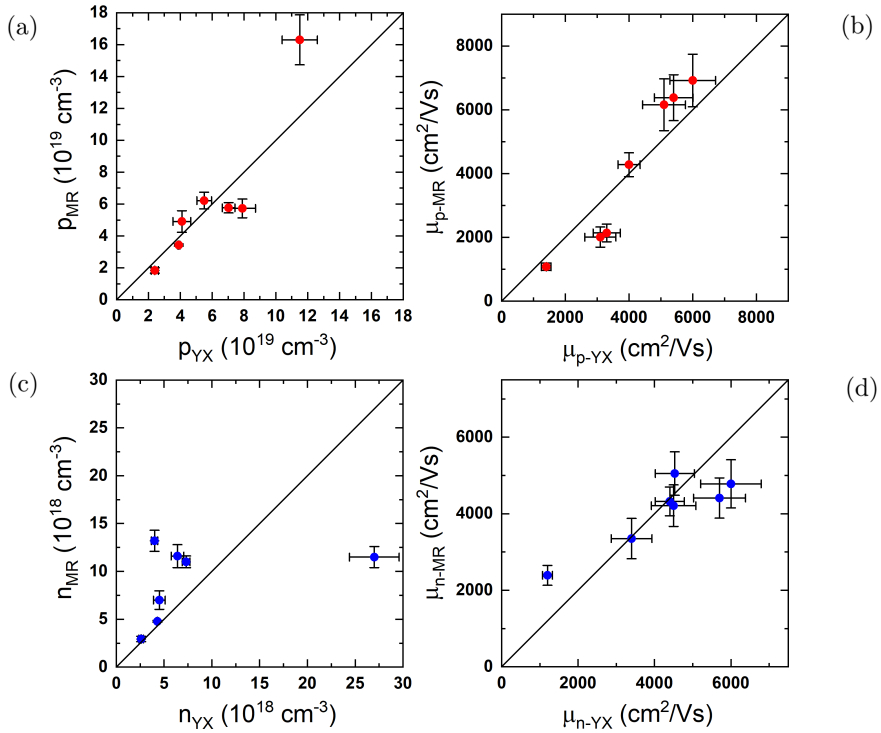

Figure 4.6: Comparison of the 2-band model fitting parameters determined from fitting the Hall resistivity and the out-of-plane MR. Solid lines show 1:1 correspondence. (a) p-type carrier density, (b) p-type carrier mobility, (c) n-type carrier density, (d) n-type carrier mobility.

changing carrier properties in the two-band model. This is shown by the reasonable agreement between the fitting parameters for both the Hall and MR fitting in Figure 4.6, where solid lines show 1:1 correspondence.

As mentioned earlier, a complicated dependence of the RRR on the defect content in impurity dominated semi-conductors is expected. The carrier properties from the Hall resistivity predict the degree of metallicity well for all the samples studied in this work, with a positive correlation between the measured RRR and effective conductivity calculated using the Hall parameters ($\sigma_{\text{eff}} = ne\mu_n + pe\mu_p$) shown in Figure 4.7a.

Figure 4.7b shows there is also good agreement between the high-field Hall effective carrier density $p_{\text{eff}} = p$ - n extracted from the high-field regime (B >5 T) of ρ_{yx} (where the data is linear with field[47]) and the same quantity calculated from the extracted fit parameters, which bolsters the reliability of the determined parameters and confirms

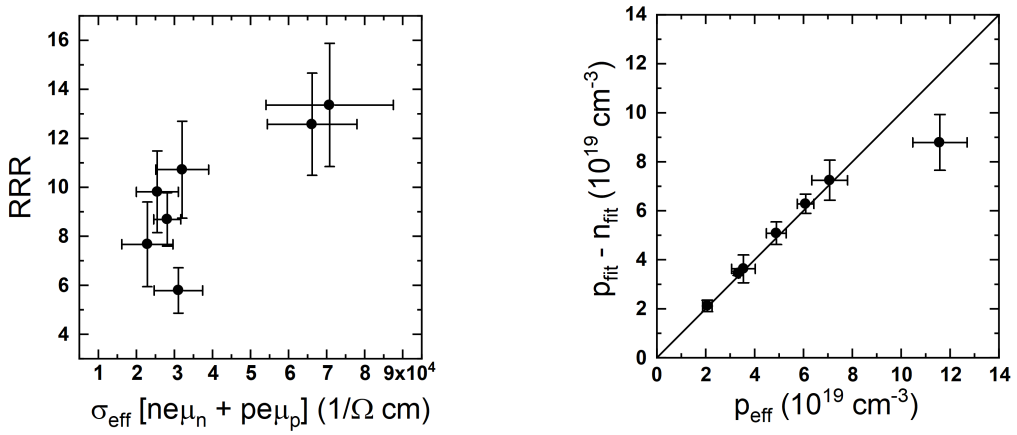

(a) (b)

Figure 4.7: Reliability of the 2-band model shown by (a) the positive correlation between the conductivity calculated from the 2-band fit parameters and the measured RRR and (b) good agreement between the 2-band fit effective carrier density and the effective carrier density determined from the high-field limit of the Hall resistivity.

the model is self-consistent.

4.4 Shubnikov de Haas Oscillations

This section focusses on the analysis of the clear SdHO visible in both ρ_{xx} and ρ_{yx}. The motivation here is to see whether the SdHO can be accounted for by either of the non-trivial surface states in the material, which was thought possible given the order or magnitude reduction in carrier density and the emergence of a clear beating envelope similar to those observed from Rashba spin-split states in 2DEG systems [148, 173], and similar to the beating envelope observed previously in low carrier density ($p \sim 10^{18}$ cm^{-3}) Sb_2Te_3 samples [17]. The range of carrier densities found allows a kind of spectroscopy of the electronic states by tracking the changes in SdHO parameters, which instead point to a region of separate bulk bands causing the SdHO beating.

4.4.1 Isolation and Resolution of Multiple SdHO

Figure 4.8a shows isolated SdHO from ρ_{xx} plotted against inverse field for the samples with the range of hole carrier densities shown in Figure 4.4a. The SdHO are extracted

by selecting the dominant peak and trough positions and interpolating for the envelope outlines, averaging these for the ρ_{xx} baseline which is then subtracted from the raw data [142, 174]. It is clear that as p is reduced from 1.2×10^{20} to 2.4×10^{19} cm^{-3} the nature of the SdHO envelope changes in Figure 4.8a, the dashed lines are a guide for the eyes to show the SdHO envelope form clearly.

For the highest carrier density sample exponential-like growth of SdHO amplitude is found, but with a small reduction of the carrier density to 7.9×10^{19} cm^{-3} an envelope that transitions from exponential at low field to non-exponential at high field is uncovered. Then, for samples with $7.0 \geqslant p \geqslant 5.5 \times 10^{19}$ cm^{-3}, the envelope looks like a beat pattern that is not completely resolved by 8 T (0.125 T^{-1}). Further reducing p to 4.1×10^{19} cm^{-3} and below, a full beating pattern with two-nodes is observed, with some additional amplitude modulation at high field from an additional SdHO. Arrows show the node positions of the beat envelopes: samples with two observed nodes have beat periods ≈ 0.14 T^{-1} so beat frequencies of ≈ 7.5 T magnitude.

To identify the principle frequencies contributing to the SdHO beat envelope Figure 4.8b shows the Fast Fourier Transforms (FFTs) taken on the SdHO, in each case taken over $0.125 \leqslant 1/\mathrm{B} \leqslant 1$ T^{-1} using a rectangular window to improve frequency resolution. The highest carrier density sample shows a dominant frequency at 51 T matching the exponential envelope and in agreement with previous work for Sb_2Te_3 with 1×10^{20} cm^{-3} carriers.[17, 152, 153] For decreasing carrier densities ($7.9 \geqslant p \geqslant 5.5 \times 10^{19}$ cm^{-3}) only one dominant frequency between 50 T - 60 T is clearly resolved despite the non-exponential envelopes. For $p \leqslant 4.1 \times 10^{19}$ cm^{-3} some partial splitting in the FFT peaks is apparent, which is most clearly seen for the lowest carrier density sample with $p = 2.4 \times 10^{19}$ cm^{-3}, clearly showing two SdHO frequencies. Also for $p \leqslant 4.1 \times 10^{19}$ cm^{-3} some higher frequency peaks are resolved close to 70 T.

The Lifshitz-Kosevich (LK) theory describes SdHO in ρ_{xx} with periodic behaviour in inverse magnetic field $1/B$, at fixed temperature, by:

$$\frac{\Delta\rho_{xx}}{\rho_{xx}} \propto R_D \cos 2\pi \left(\frac{F}{B} - \frac{1}{2} + \beta \right) \tag{4.1}$$

Here, the Dingle term $R_D = \exp\left[-2\pi^2(\frac{k_B T_D}{\hbar\omega_c})\right]$ describes the exponential amplitude growth with field, characterised by the Dingle temperature T_D; F is the SdHO frequency in units of T, which is proportional to the extremal Fermi surface cross sectional area (CSA); and β is a phase offset determined by the Berry phase of the carriers [44, 78, 175].

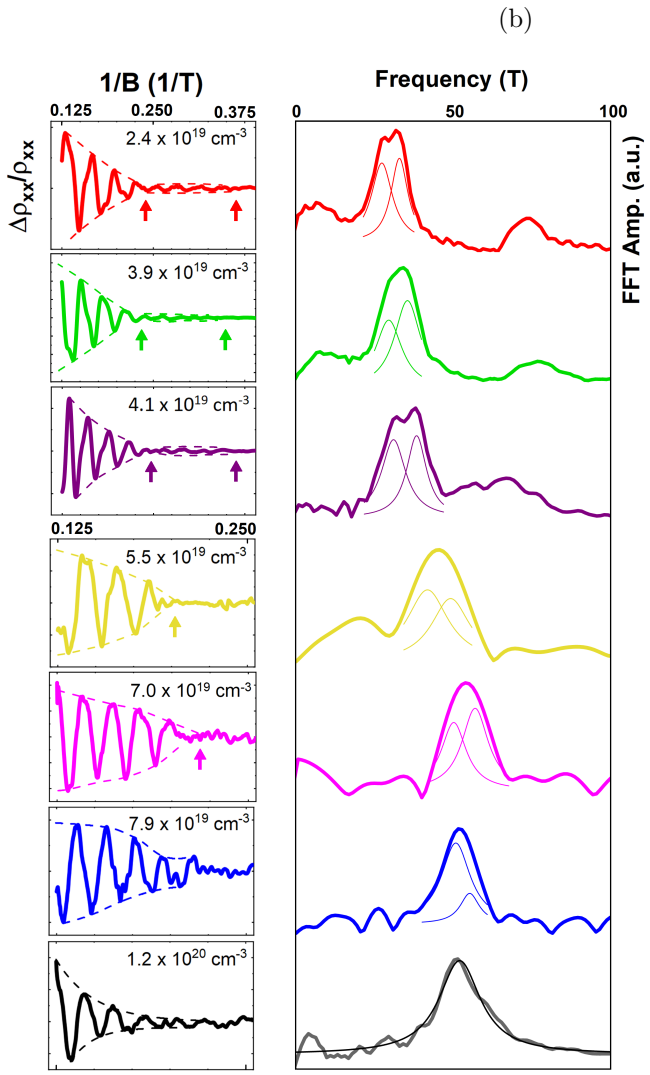

Figure 4.8: Reducing the carrier density in Sb_2Te_3 leads to the emergence of a non-exponential SdHO envelope (a) reducing carrier density from bottom to top, non-exponential envelope patterns are apparent with a small reduction of the carrier density compared to the nominally stoichiometric sample, where a clear beat pattern with nodes (shown by solid arrows) is resolved in the 3 lowest carrier density samples. (b) FFT of the beat envelopes show partial splitting of frequency peak between 20 - 30 T for the lowest carrier density samples, but no splitting for other samples which show a beating envelope. Insets show the decomposition of the FFT peaks by multiple-peak Lorentz fit, unveiling the hidden second frequencies required to produce the beating envelopes.

This means non-exponential SdHO envelopes must arise through the interference of multiple frequencies, given the exponential growth of a single SdHO amplitude with field governed by R_D, and that these SdHO with different frequencies are caused by the extremal limits of Fermi branches with different CSA.

For the samples with $p \leqslant 4.1 \times 10^{19}$ cm^{-3}, there are clearly three SdHO frequencies required to describe the envelope. For the higher carrier density samples the picture is less clear: the minimum requirement to describe a beating SdHO envelope is two frequencies with closely matched amplitude and decay rate. Since the resolution of the FFT depends on the magnetic field range measured over and the number of oscillation periods present, it is thought that in samples with only partially resolved beating envelopes ($5.5 \geqslant p \geqslant 7.9 \times 10^{19}$ cm^{-3}) the frequency splitting is present but not fully resolved in the FFT. For $p \leqslant 4.1 \times 10^{19}$ cm^{-3} the resolution increases due to the SdHO emerging at lower fields, increasing the visible/sampling range of the SdHO, and the individual components are clearly seen.

It is difficult to claim that there may not be more hidden frequencies within the single peak, however, since no additional amplitude modulation or a second beat frequency is resolved, it is only possible to reliably uncover two frequencies from the FFTs since this is the minimum requirement for the observed beating envelope. Measurements to higher fields would give better resolution in the FFTs and firmly confirm the number of SdHO frequencies in the envelopes. Given this, to uncover the frequencies contributing to the SdHO envelopes, a double peak Lorentz fit is used since the Fourier transform of SdHO envelope takes a Lorentz form [176, 177]. The decomposed peaks are shown in Fig. 4.8b and the frequencies given in Table 4.1.

For the samples with clearly resolved beat amplitude nodes in ρ_{xx} ($p \leqslant 4.1 \times 10^{19}$ cm^{-3}) the beat frequency determined from the beat period is consistent with the frequency differences found by fitting the FFT ($\approx$ 6 - 7 T), confirming that the beating arises from the closely matched frequencies near to 30 T. Also, the samples with beating envelopes show decomposed FFT peaks with similar amplitude and width, corresponding to SdHO with similar amplitude and decay rate as required to produce a true beating envelope. The sample with $p = 7.9 \times 10^{19}$ cm^{-3} shows a high amplitude and low amplitude SdHO which convolute at higher fields to produce a non-exponential envelope, rather than a true beating envelope.

Previously, SdHO envelopes with multiple frequencies have been observed in Sb_2Te_3

with reduced carrier densities. For $B \parallel c$, there is the emergence of two frequencies for samples with $p \sim 10^{19}$ cm^{-3}, close to 30 T and 80 T in agreement with our findings [152, 153], however the splitting of the peak near to 30 T has not been reported in those studies.

We note that previous work has reported an angular dependent beating envelope in Sb_2Te_3 [152]. There, the minimum angle required to produce the beating is 5 degrees from the out-of-plane direction, rotating towards either the a or b directions in Figure 4.2a. Since the samples are aligned parallel to the chip carriers by less than 1 degree along both the long and short axis of the cleaved samples, the alignment to the field out-of-plane is less than 1 degree in all cases, and this possibility is discounted.

The only similar beat pattern to that observed here is in superconducting samples of Sb_2Te_3 with $p \sim 10^{18}$ cm^{-3} [17]. In general, this kind of beating envelope is observed in 2DEG quantum well structures with appreciable Rashba spin-splitting of the energy bands [148, 173]. With contributions to the transport from these non-trivial states in Sb_2Te_3 in mind the usual Berry phase analysis is employed to further investigate the nature of the SdHO.

4.4.2 SdHO Fitting and Phase Analysis

It is well known that $\beta = 1/2$ is a strong indication of Dirac-like surface states with π Berry phase, which has been observed in many TI materials [54, 56, 79]. It has also been shown that Rashba spin-split states should have a $\pm\pi$ Berry phase ($\beta = \pm\ 1/2$) for each Fermi branch, the opposing sign arising from the opposite spin helicities of each branch [54, 174, 178–180]. To determine whether the novel SdHO beat envelopes arise from Dirac or Rashba surface states, the values of β are extracted by direct fitting of the LK equation to the $\frac{\Delta\rho_{xx}}{\rho_{xx}}$ data, which is more straightforward than Landau level (LL) indexing for multiple convoluted frequencies [142, 174].

Figure 4.9 shows the isolated SdHO from both ρ_{xx} and ρ_{yx}, corrected for the intrinsic $B^{1/2}$ dependence in the LK equation. The oscillations isolated from ρ_{yx} show the same behaviour as those from ρ_{xx} as expected, the clear beating envelope seen from both data sets. No SdHO were visible in ρ_{yx} for the sample with $p = 7.0 \times 10^{19}$ cm^{-3} due to the low amplitude. The solid lines show the fits to a linear combination of LK equations with frequencies fixed as the values from the FFTs. As explored in Chapter 3, the functional form of the SdHO in ρ_{yx} is identical to those in ρ_{xx}. The phase offsets

p ($\times 10^{19}$ cm^{-3})	F_1 (T)	k_F (Å^{-1})	β_1	p/n	F_2 (T)	k_F (Å^{-1})	β_2	p/n	F_3 (T)	k_F	β_3 (Å^{-1})	p/n
2.4	27.6	0.0289	-0.075	p	33.1	0.0317	0.039	p	73.5	0.0472	0.110	p
3.9	29.7	0.0300	0.029	p	35.6	0.0329	0.016	p	76.8	0.0483	0.005	p
4.1	31.0	0.0307	-0.302	p	38.3	0.0341	0.340	p	71.4	0.0466	-0.16	p
5.5	41.8	0.0356	-0.35	p	49.2	0.0386	0.30	p				
7.0	50.0	0.0390	-0.51	p*	56.8	0.0415	0.33	p*				
7.9	50.7	0.0392	-0.40	p	55.0	0.0408	-0.36	n				
12	51.2	0.0394	0.11	p								

Table 4.1: Summary of the Hall carrier density dependence of the SdHO frequencies (F_i), phases (β_i), and determined carrier types (p or n, hole or electron). For $p = 7.0 \times 10^{19}$ cm^{-3} carriers * indicates that the carrier type is not determined by deconvolution but inferred from the change of CSA relative to the $p = 5.5 \times 10^{19}$ cm^{-3} sample. Non-trivial phases are resolved for a significant number of samples.

are summarized alongside the frequencies in Table 4.1. Intriguingly, the determined phases in Table 4.1 suggest some non-trivial branches are contributing to the SdHO envelope since many deviate from the trivial phase expected for a parabolic band.

By comparing SdHO maxima and minima in ρ_{xx} and ρ_{yx} the carrier type of the SdHO is also determined [138, 141, 181] and given in Table 4.1. For further characterisation the SdHO frequencies in Table 4.1 are used to estimate a Fermi wave-vector k_F assuming a circular CSA using the relations: $\text{CSA} = F\frac{2\pi e}{\hbar}$; $k_F = \sqrt{\text{CSA}/\pi}$.

For clarity, Figure 4.10a shows an example of the separate SdHO components giving the beating envelope for the sample with $p = 2.4 \times 10^{19}$ cm^{-3}, which have similar amplitude and decay rate as required to give the clear SdHO beating. Figure 4.10b shows a reconstructed LL fan diagram which confirms that the SdHO observed are also far enough from the quantum limit ($n \geqslant 5$) so that the phase is correctly determined by this method [55, 56]. The x-axis intercepts in Fig. 4.10b agree with the determined phase in Table 4.1, as required.

Overall, the nominally stoichiometric sample has a dominant trivial hole-like Fermi branch in agreement with previous work [152, 153]. There is then a non-trivial phase for both branches with $7.9 \geqslant p \geqslant 4.1 \times 10^{19}$ cm^{-3}. The non-trivial phase determined for the sample with $p = 4.1 \times 10^{19}$ cm^{-3} is particularly interesting given the reliability of the FFT analysis due to the clear peak separation. Notably one branch arises from

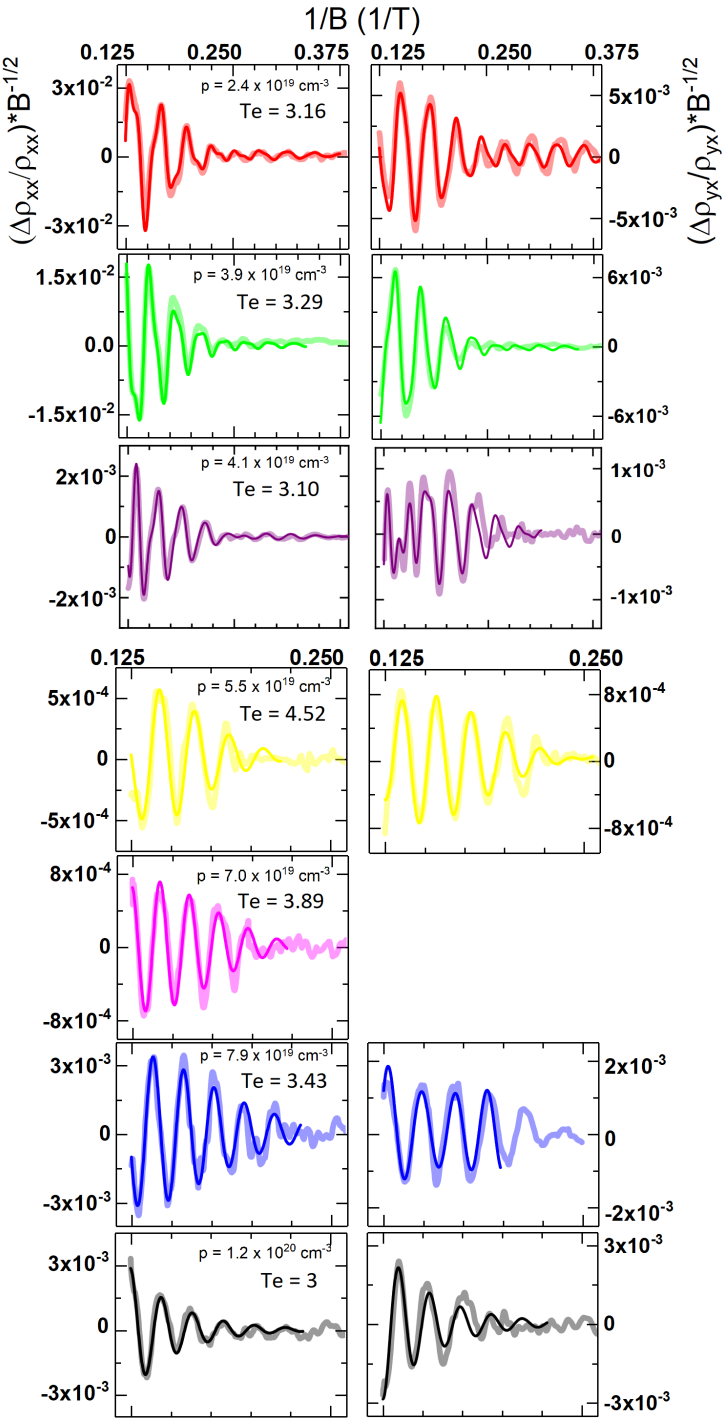

Figure 4.9: Isolated SdHO (opaque lines) plotted against inverse field for both ρ_{xx} and ρ_{yx}. Solid lines show the LK equation fits.

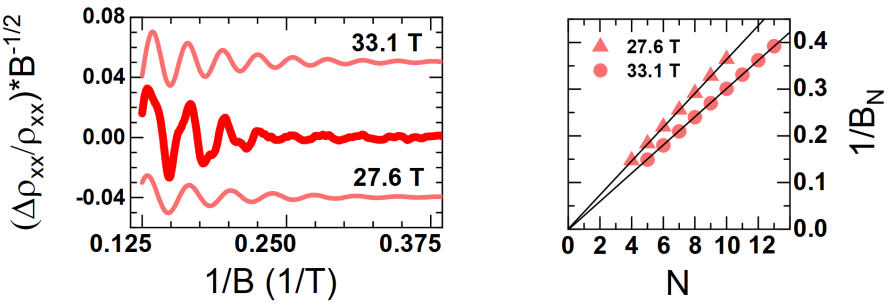

(a) (b)

Figure 4.10: (a) Example of SdHO breakdown into separate frequency components with similar amplitude and decay rate that produce the beating in the sample with p = 2.4 $\times 10^{19}$ cm^{-3}. (b) The LL fan diagram composed by plotting the decomposed SdHO minima positions in inverse field against LL index, whose x-axis intercepts are the same as the phase offset determined by fitting.

electron-like carriers for the sample with $p = 7.9 \times 10^{19}$ cm^{-3}, with larger CSA than the hole-like branch: since the Hall data still shows a dominant p-type band there must be a significant source of hole carriers not contributing to the SdHO. There are two dominant hole-like branches for $p \leqslant 3.9 \times 10^{19}$ cm^{-3}, however trivial phases are instead found implying a change in the nature of the electronic states. The high frequency SdHOs for $p \leqslant 4.1 \times 10^{19}$ cm^{-3} seem to arise from trivial p-type branches.

Since the Rashba surface states reside within a partial band gap in the valence band structure of Sb_2Te_3 [18–21], the determined changes of Berry phase with Hall carrier density are consistent with the idea of tuning from below to above the Rashba states, since both branches show a non-trivial phase with opposing polarity. Detailed consideration is therefore given to the SdHO origins, where it is found, however, that the non-trivial phase SdHO are likely caused by bulk states with predominantly linear dispersion and the beating by separate bulk Fermi branches with closely matched cross sectional area, rather than the spin-split Fermi branches of the Rashba surface state.

4.4.3 Origins of Non-Trivial SdHO

First, it is unlikely that the Dirac surface states are responsible for the SdHO in any cases as they should be more visible with reduced carrier densities, which is not consist-

ent with the observation of $\beta \approx 0.5$ only for $4.1 \leqslant p \leqslant 7.9 \times 10^{19}$ cm^{-3}. Also, only one SdHO frequency with non-trivial phase would be expected for the single Dirac surface state [168].

Further, the frequencies determined here are in-fact smaller than those reported for the SdHO beats arising from the 2DEG state in superconducting Sb_2Te_3, where F_1 and F_2 were reported as 34 T and 42 T respectively in samples with an order of magnitude lower Hall carrier density [17].

Regarding the Rashba-split surface states, Figure 4.11 first shows the calculated band dispersion for a 6 quintuple layer thick sample of Sb_2Te_3 in the region of the band structure hosting the Dirac surface state and Rashba-split surface states, taken from Reference [19]. The grey regions and black lines show the bulk band dispersions, and red and blue circles indicate opposite spin directions for the surface states, the size of the circles indicate the magnitude of the spin density [19].

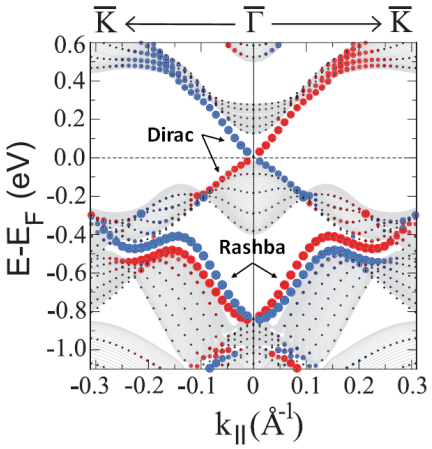

Figure 4.11: Calculated band structure of a 6 quintuple layer Sb_2Te_3 sample taken from Ref. [19], clearly showing the Dirac and Rashba surface states. Bulk bands are shown by grey regions and black dotted lines. Red and blue markers show opposite spin directions for the surface states.

Importantly, the range of k_F values observed for all the SdHO, not just those with non-trivial phase, limits the possible regime of bands that may be observed here to: $0.029 \leqslant k_{\|} \leqslant 0.048$ Å^{-1}; corresponding to $\approx$ -0.70 $\geqslant$ E $\geqslant$ -0.85 eV in Figure 4.11. In this region the expected momentum splitting Δk_F between the inner and outer Rashba branches is in the range $0.020 \leqslant \Delta k_F \leqslant 0.025$ Å^{-1} [18–21]. The largest Δk_F observed

between beating frequencies that both have non-trivial phase is $\Delta k_F = 0.003$ Å^{-1} for a 7.4 T frequency difference $(F_2 - F_1)$ in the sample with $p = 5.5 \times 10^{19}$ cm^{-3}, which is much smaller than expected, essentially ruling out the possibility of the Rashba states being responsible for the beating envelope.

Further, the dispersion of the Rashba states in the region corresponding to the determined k_F range has decreasing CSA moving further into the valence band, so it is expected that the Rashba states would be uncovered as electron-like by the deconvolution technique. Instead it is found that most SdHO come from hole-like Fermi branches and no sample shows two separate electron-like branches with non-trivial phase as would be required for the two separate spin branches of the Rashba states in this range, compounding the conclusion that the Rashba states cannot explain the observed SdHO beating patterns and non-trivial phases extracted.

Whilst the Dirac and Rashba surface bands in Sb_2Te_3 cannot account for the non-trivial phases observed, there have recently been many observations of SdHO with non-trivial phase in 3D Dirac semimetals [57] and materials with bulk Rashba-split bands [174, 178, 182]. The latter case requires inversion symmetry breaking in the bulk which is not the case in Sb_2Te_3, but recalling that the Hamiltonian describing bulk Sb_2Te_3 has a 3D Dirac form [4, 23, 48] it may be possible that Dirac-like linearly dispersive states in the *bulk* of the material are responsible for the non-trivial phase.

Also, whilst a linear Dirac form of the bulk bands may be found in Sb_2Te_3, there is no need for Dirac point degeneracies to be strictly enforced at high-symmetry points in the Brillouin Zone [183–185], bands dispersing linearly away from *accidental* band crossing points also result in a Berry phase of π [54, 186, 187].

In the most general case of bulk bands with convoluted contributions from linear and parabolic dispersions the strict quantisation rules of the Berry phase break down, whose value then depends on the details of the band structure. For quadratic bands the Berry phase approaches 0, for linear bands around a Dirac point the Berry phase approaches π, and for mixed systems the phase is a continuous function that tunes between the two values depending on the strength of each relative contribution [55, 56].

An approximate range of chemical potential positions in the band structure can be estimated to search for bulk states dispersing linearly away from band touching (Dirac) points, that may be causing the observed SdHO. A first-order estimation using a parabolic model: $E = \frac{\hbar^2 k_F^2}{2m_D}$, $k_F = (3\pi^2 p)^{1/3}$, with Hall carrier density p and an

average density of states effective mass $m_D = 0.24\ m_0$ from literature [152] gives the chemical potential bounds as $-0.1 > E > -0.4$ for the carrier density range measured here.

For reference, a schematic of the bulk band structure in both the $\Gamma - K$ and $\Gamma - M$ directions is shown in Figure 4.12. This figure has been traced and adapted from ARPES and DFT calculations of a partial $\Gamma - K$ dispersion for bulk Sb_2Te_3 in Refs. [20, 21], and ARPES and DFT of the $\Gamma - M$ and wider $\Gamma - K$ dispersion for a 6 quintuple layer sample in Ref. [18] but with the energy scale compressed to match that for the bulk sample. The features of the bands and widths in momentum are essentially equivalent between these studies, but the bulk energy scale is used as reference here allowing direct relation to our samples. Black lines show the bulk band edges, grey dashed lines show the internal dispersive nature of the bands, red and blue show the opposite spin direction for the surface states.

The expected energy range is shown by the dashed horizontal lines, clearly limiting the possible electronic states causing the SdHO to be those in BVB 1 and at the upper limit of BVB 2. First, this estimated energy range further reinforces that the Rashba surface states are not responsible for the SdHO: the expected circular CSA for the Rashba states near the top of BVB 2 would result in an SdHO frequency of $\approx$ 350 T for $k_F \approx 0.1$ Å^{-1}, much higher than any observed. It also implies that much *higher* carrier densities are required to reach the region of BVB 2 below the Rashba bands. Despite not observing SdHO from the Rashba states here, the chemical potential positions imply that they should give a significant contribution to the surface transport in the higher carrier density samples in this study.

In this region the section of BVB 1 extending in the $\Gamma - K$ direction has significant segments of more linear dispersion, caused by a strong resonance with the Dirac surface state [20]. There are also clusters of accidental band touching points at the intersections of these band pockets [18–21].

It is most likely then that these electronic states are responsible for the SdHO with non-trivial phase. Since there is a predominantly linear but ultimately mixed dispersion, a natural explanation arises for the non-trivial, but non-quantised, phase values extracted from the SdHO [55, 56].

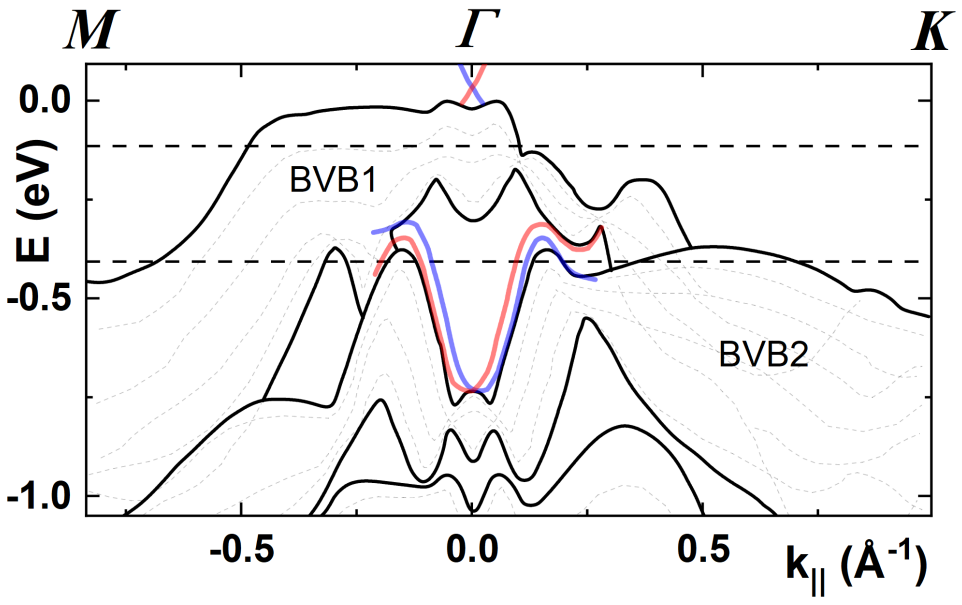

Figure 4.12: Band structure for bulk Sb_2Te_3 traced and interpolated from Refs. [20, 21] and [18]. Dashed horizontal lines signify the estimated range of the band structure observed in this work, highlighting that the section of BVB 1 along $\Gamma - K$ with linearly dispersive bands and accidental band crossing points is likely responsible for the non-trivial Berry phase SdHO. Edges of the bulk band continuum are shown by black lines and grey dashed lines show the internal dispersive nature of these bands. Red and blue markers show opposite spin directions for the surface states.

The identification of these states in the band structure highlight Sb_2Te_3 as a Dirac semi-metal [183–185], and the non-trivial Berry phase extracted from the SdHO serves as the first experimental confirmation of these bulk Dirac states in Sb_2Te_3 [186, 187].

The non-trivial phase SdHO therefore seem to arise from a Dirac band dispersion in the bulk of Sb_2Te_3. To further check the reliability of this identified band region in explaining the SdHO the other parameters extracted in Table 4.1 are considered to see how well the SdHO describe the overall band structure in this region. Since the estimated chemical potential range is based on a simplified parabolic model, stronger predictions may be gained by measuring the density of states effective mass directly for the samples in this study, instead of relying on estimates from previous work. Despite the simplified model however, the next section finds good agreement between the measured SdHO parameters and the expected bulk electronic states.

Comparison to Band Structure

For clarity the schematic of the bulk band structure is plotted again in Figure 4.13, now with the estimated chemical potential position for each sample in this study using the same parabolic model as before, adjusted within the uncertainty range for each carrier density. The chemical potential positions are shown by the coloured horizontal lines, where the colours match those used in previous figures.

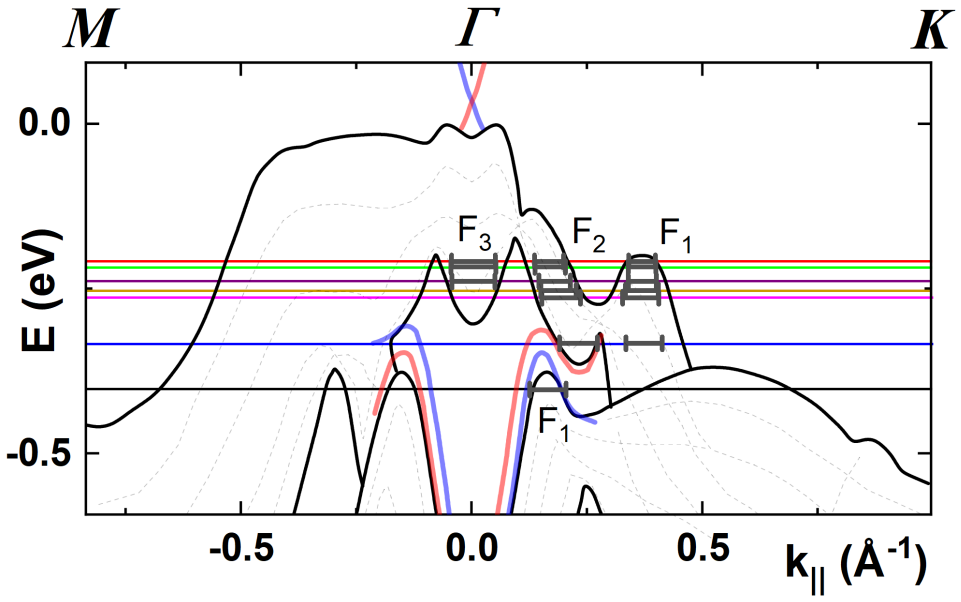

Figure 4.13: Schematic of the band structure of Sb_2Te_3 with solid colour horizontal lines showing the estimated chemical potential positions for the associated sample. Inset black line segments show the diameter of Fermi branches estimated from the SdHO.

The chemical potential for the highest carrier density sample is predicted to lie slightly below BVB 1, where the parabolic upper section of BVB 2 along $\Gamma - K$ centred at 0.164 $Å^{-1}$ is expected to give the SdHO with trivial phase. At this chemical potential position there is a similar section along $\Gamma - M$ with slightly larger CSA caused by the complicated dispersion mixing of BVB 1 and BVB 2. It is possible to extract a second SdHO from the FFT for this sample, due to the slight peak asymmetry in Figure 4.8b, with frequency $\approx$ 60 T that is also hole-like and has slightly non-trivial phase which plausibly arises from this band pocket. The dominant frequency close to 51 T

is therefore found to arise from a 6-branch Fermi surface, and the minor frequency contribution also comes from a similar CSA 6-branch Fermi surface, in total giving a 12-branch structure in the nominal stoichiometric sample in agreement with previous work for samples with $p = 1 \times 10^{20}$ cm^{-3} [152, 153].

The emergence of the non-exponential and beating envelopes with decreasing p is then likely caused by the chemical potential being tuned upwards into the separate branches of BVB 1 centred at $k_{\|} \approx 0.18$ Å^{-1} and 0.37 Å^{-1} that have similar, but slightly different, CSA. This also accounts for the electron-like branch found for the sample with $p = 7.9 \times 10^{19}$ cm^{-3} which arises due to the bottom edge of the branch centred at $k_{\|} \approx 0.18$ Å^{-1}, also implying that the SdHO with F_2 arise from the inner branch. Accordingly, the non-trivial phases found with decreasing p are consistent with the change from predominantly parabolic to linear band dispersion as the chemical potential is tuned into this section of BVB 1 with dominant linear dispersion [20]. With further decrease in p to $\leqslant 3.9 \times 10^{19}$ cm^{-3} the beating envelope still seems to arise from these separate branches of BVB 1, however the trivial phase is explained by reaching the upper limits of these branches where the band dispersions must necessarily become more parabolic.

The origins of the higher frequency SdHO in samples with $p \leqslant 4.1 \times 10^{19}$ cm^{-3} are less clear based on the band structure in this region: they are most likely caused by the central band dispersion given the expected k_F values and the decrease in CSA between $p = 3.9$ and 4.1×10^{19} cm^{-3} supports this. However these bands should behave as electron-like given the curvature and instead all are extracted as hole-like, which is not expected given the band dispersion. We note that there may be some additional contributions from second harmonics since the high frequency peaks are close to the values of $2F_1$ and $2F_2$ which are difficult to reliably account for given the low amplitude of these SdHO compared to the dominant beating frequencies, which may be responsible for inconsistencies between the SdHO and the expected physical picture for these high frequency branches. These additional SdHO are not resolved for the samples with $5.5 \leqslant p \leqslant 7.0 \times 10^{19}$ cm^{-3} due to a combination of lower SdHO amplitude and smaller field range over which the SdHO are observed, which is due to higher structural inhomogeneity judged by the XRD peak widths.

A comparison of the k_F values from the SdHO to those expected from the band widths can be given assuming circular cross sectional areas for all branches, which

gives an average value of k_F for the two axes of the Fermi pocket perpendicular to the applied field. For the branches of BVB 1 identified these are likely within the range $0 < k_F \leqslant 0.06$ Å^{-1} which gives good agreement with the values determined in Table 4.1. To show a comparison to the observed values, the black line segments inset on the chemical potential positions in Figure 4.13 show the width $2k_F$ calculated from the SdHO frequencies placed at the central point of the dispersion each SdHO is thought to arise from.

The higher $k_{||}$ states along $\Gamma - K$ in BVB 2 are discounted from contributing any observed SdHO as the approximate CSA from the band structure is expected to be $\approx$ 4 times larger than that observed in the SdHO, assuming no widening perpendicular to $\Gamma - K$, which is not consistent with the values of k_F determined. This is also true for the higher $k_{||}$ states along $\Gamma - M$ in BVB 1 that extend down through BVB 2. These have been observed in ARPES to have CSA, at the top limit of the valence band, an order of magnitude larger than what is observed here [18], which based on Figure 4.13 remains true for all the samples in this study.

It is important to re-state that the upper part of BVB 2 hosts part of the intrinsic Rashba surface states and so they should be partially occupied for samples with high carrier densities $p \geqslant 7.9 \times 10^{19}$ cm^{-3}. In this region, the Rashba states actually have the widest possible CSA and so highest carrier density, which is important for maximising their contribution to the surface transport. At present, assuming $k_F \approx 0.1$ Å^{-1} in this region, a surface channel thickness $\approx$ 1 nm from previous work [188], and a typical mobility found here $\mu \approx 5000$ cm^2/Vs, the total contribution to the transport from the Rashba surface states in samples with the dimensions here is estimated as 0.001%, making them unobservable through transport.

Since reducing the carrier density will tune away from the Rashba states and make the topological Dirac state the dominant surface contribution to the transport, the physical size of the crystals must be reduced to increase the surface to volume ratio and allow the surface contributions to be observed whilst keeping the chemical potential close to the Rashba surface states.

It is predicted that exfoliated single crystal examples of Sb_2Te_3 like those here would show a 5% contribution from the Rashba states for a thickness $\sim$ 50 nm, which should be resolvable in the transport [168] and is currently achievable, though difficult, given current exfoliation methods [16]. After this, electrostatic gating may allow for tuning

of the chemical potential between the separate Dirac and Rashba surface contributions [16, 68, 166].

Overall then we have confirmed that the bulk contributions to the transport are still too high to resolve the Rashba surface bands in Sb_2Te_3. Despite this, the consideration of the observed SdHO and predictions of chemical potential positions suggest that they should be occupied on the surface for carrier densities in the range $p \geqslant 7.9 \times 10^{19}$ cm^{-3}, opening an avenue for characterisation in exfoliated single-crystal flakes. The characterisation of the bulk states and the spurious non-trivial phase will also be useful in disentangling any surface state contribution from the bulk in future studies.

4.5 Discussion of the Origins of Carrier Bands

Fundamentally, all the free carriers in Sb_2Te_3 arise from defects, since the bonding between Sb and Te leads to completely full valence bands for the ideal crystal. The important question then is what kind of band do these carriers exist in: namely an impurity band or an intrinsic band, and how can the pictures determined from the Hall effect and SdHO be consistent with one another?

The high numbers of defects in Sb_2Te_3 naturally support the existence of two *impurity* transport bands. In MBE grown samples the defect density N, determined by Scanning Tunnelling Microscope (STM) images, approaches $N \sim 10^{20}$ cm^{-3}, where each one has an effective Bohr Radius $a^* \sim 2$ nm [158, 189]. The concentration of defect states is therefore above the threshold for metallic impurity band conduction according to the Mott criterion: $Na^3 > 0.02$ [190], the limit being $N \sim 10^{18}$ cm^{-3} for $a^* \sim 2$ nm. This also means high mobilities may generally be expected from the impurity bands [190].

As well as this, the existence of different types of carriers is also naturally explained from the $V_{Te}^{\cdot\cdot}$ vacancies acting as donors, and the Sb_{Te}' anti-site defects acting as acceptors. It is known that in stoichiometric crystals of Sb_2Te_3, $V_{Te}^{\cdot\cdot}$ vacancies contribute 2 electrons each, Sb_{Te}' anti-site defects contribute 1 hole each, with roughly 6 times more Sb_{Te}' defects than $V_{Te}^{\cdot\cdot}$ and so ≈ 3 times more hole carriers than electron carriers.[62] In the stoichiometric sample here, $p/n = 4$, consistent with this picture and suggesting that the Hall bands are comprised of carriers arising from these defects, and are therefore representing the impurity band transport.

With excess Te, the amounts of both defect should decrease according to defect

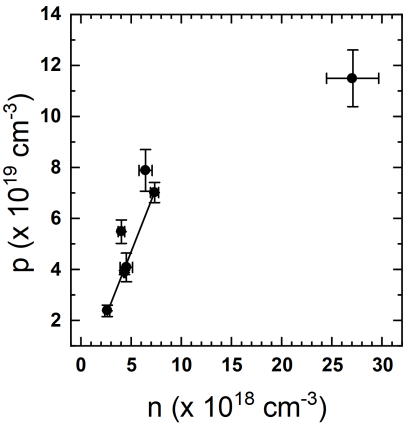

Figure 4.14: Positive correlation between the p and n type carrier densities across the carrier density range, consistent with energy formation calculations predicting a reduction of both Te vacancies and Sb_{Te} anti-site defects.

formation energy calculations [158]. This is again consistent with the determined Hall carrier parameters, finding that both p and n decrease with excess Te. Figure 4.14 shows the carrier densities plotted against one another: the fitted linear dependence has a slope of 1, implying a strong correspondence of the formation of each carrier, as would be expected given that an Sb_{Te} anti-site can only form if a vacant Te site is available. This relationship is not expected in an intrinsic semi-metallic system with offset and overlapping bands, since a reduction in an intrinsic p carrier density should give an increase in an intrinsic n carrier density.

SdHO like features in ρ_{xx} have been observed in semi-conducting materials with degenerate impurity bands [191], where the effect is understood through the tight-binding model as a result of the interference of carrier wave-functions moving in between impurity sites arranged in a random lattice. This is understood as more of an Aharonov-Bohm effect rather than a true SdHO effect, though the characteristic fields and functional temperature dependence are similar [191].

Importantly, the tight binding picture predicts that the effective mass of the carriers should increase as the band-width between tunnelling sites decreases, which is inversely proportional to the separation between sites, or $N^{1/3}$ [191]. To extract the cyclotron mass for Sb_2Te_3 here, the temperature dependence of the SdHO amplitude is measured up to 30 K, where fitting to the R_T term of the LK equation allows for direct extraction

of m_c.

An example of this data is shown for the lowest carrier density sample in Figure 4.15(a), and the full breakdown of each FFT peak's amplitude dependence on temperature is shown in Figure 4.15(b). The amplitude temperature dependence and fitting to the R_T term is summarised for all the samples in Figure 4.15(c) and the determined cyclotron masses are summarised in Figure 4.16.

We find that m_c is essentially constant across the carrier density range, which would not be expected for an impurity band [191]. The values of m_c are also consistent with those expected of the intrinsic states thought to give the SdHO observed here, and with those in previous work that confirms the intrinsic nature of the states by confirmation of the expected arrangement of the Fermi branches dictated by the crystallographic symmetries [131, 152, 153].

Further, the detailed consideration of the SdHO changes with carrier density strongly suggest the existence of carriers populating the intrinsic band states of the material, given the good agreement found between the SdHO and the intrinsic band structure of the material. Taken with the effective mass analysis, it is reasonable to conclude that the oscillatory features are true SdHO arising from the intrinsic states of the material.

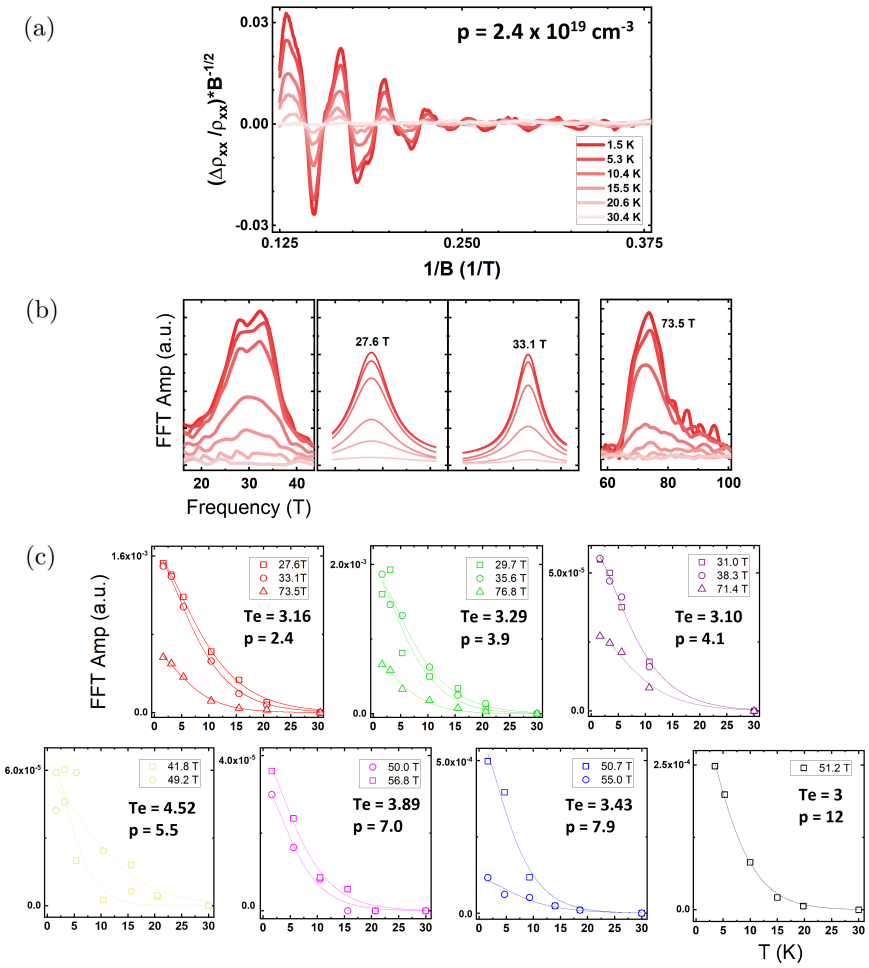

Figure 4.15: (a-b) Full breakdown of the SdHO and FFT peak amplitude temperature dependence for the sample with $p = 2.4 \times 10^{19}$ cm^{-3}. (c) Summary of the temperature dependence of the FFT amplitudes fitted to the the R_T term of the LK equation to determine the cyclotron mass of the carriers.

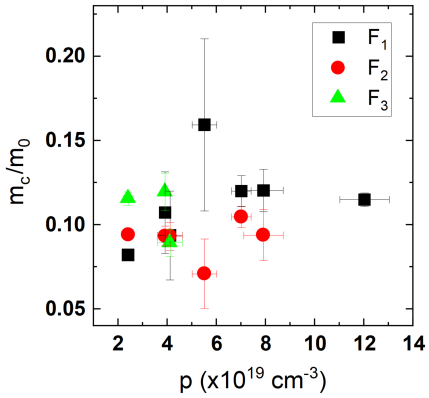

Figure 4.16: Carrier density dependence of the cyclotron mass extracted from the temperature dependence of the SdHO. All are close to the average value of 0.1 m_0.

In this case, the most likely scenario is that the high number of hole carriers are populating the intrinsic states of the material, since with high-defect content the impurity bands merge into the intrinsic states as the binding impurity potential is effectively completely screened [191, 192], but the electron carriers are remaining as a separate impurity band, accounting for the correlation of the carrier properties found in the Hall effect. Qualitatively, the Te vacancy may have a higher binding energy, thereby requiring higher carrier densities to be completely screened [192].

We find that the k_F values from SdHO are lower than, but consistent with, the determined p-type Hall carrier densities: assuming 6 spherical pockets for each branch centred away from $k_{\|} = 0$, the SdHO carrier density reduces from 2×10^{19} cm^{-3} to 1×10^{19} cm^{-3} from the samples with Te = 3 to Te = 3.16. The additional p-type Hall carriers likely arise from the wider CSA states not showing SdHO.

Overall then, this suggests a complete picture of the transport in Sb_2Te_3, with holes introduced by Sb_{Te} anti-site defects occupying the intrinsic states of the material and electrons introduced by Te vacancies forming a high-mobility impurity band. This picture is supported by a SdHO cyclotron mass which does not increase with decreasing defect density and is consistent with estimates from the intrinsic bands of Sb_2Te_3, and by the correlation of the electron carrier densities in the Hall effect with the hole carrier densities in line with the expected changes in defect content.

4.6 Summary

This chapter has presented an investigation into the electronic transport properties of Sb_2Te_3, motivated by the desire to find low bulk carrier density, high surface carrier mobility materials for device applications. Excess Te is used in a modified Bridgman method to produce high quality single crystals, which all show the expected XRD peaks for Sb_2Te_3 and a constant c-axis for all compositions which is consistent with values reported in the literature.

The transport properties of the samples show significant changes across the composition range grown. The Hall resistivity is discussed in terms of a multiple band transport model for the first time, and contributions from both hole and electron carriers are found. The origins of these carriers are discussed in terms of the dominant defects in the samples, and overall a transport model comprised of hole carriers populating the intrinsic band states of the material and a de-localised impurity band of electron carriers is proposed.

An order of magnitude reduction in the carrier density is found for samples grown with a 5% atomic excess of Te, and this persists for up to 10% excess incorporated into the growth. The carrier density range grown allows for a detailed investigation of the electronic states of the material as SdHO are identified across the composition range. A novel beating envelope with non-trivial Berry phase is identified, in-line with expectations from Rashba split-surface states, however a detailed consideration of the SdHO reveals that separate bulk Fermi branches with similar CSA and linear character are likely responsible for this.

Based on the observed SdHOs agreement with the expected electronic states at the chemical potential, further work using the exfoliation of samples with $p \geqslant 7.9 \times 10^{19}$ cm^{-3} is proposed to be able to observe contributions from the Rashba surface bands, overall highlighting Sb_2Te_3 as a promising candidate for further study.

Chapter 5

$RhPb_2$

5.1 Introduction

Experimental searches for novel topological materials are often based upon theoretical proposals: the original theoretical work regarding 3D TIs from Fu, Kane and Mele proposed that the phases may be experimentally realised in Bi-Sb alloys [43, 193].

In recent years, significant progress has been made in the ability to consider the topological properties of materials from first principles in a systematic, large-scale way, and algorithm based materials database analysis has led to the proposal of thousands of novel topological materials to be studied experimentally [32–36].

Such work, combined with consideration of existing literature and material specific theoretical publications, provides fertile ground to search for novel topological materials that may open avenues to increased functionality. One of these materials, $RhPb_2$, has been identified as a semi-metal with symmetry-enforced band degeneracies at the N and P points of the Brilluoin Zone [32–37, 194].

Alongside this, $RhPb_2$ is a member of the $CuAl_2(C16)$ materials class, all of which have a body-centred tetragonal crystal structure with space group $I4/mcm$ shown in Figure 5.1, and many of which host superconductivity [38, 39, 195]. Two papers in the literature find superconductivity in bulk $RhPb_2$, which find T_c to be 1.3 K [38] and 2.7 K [39], meaning there is a significant possibility of finding TSC in this superconducting Dirac semi-metal [40].

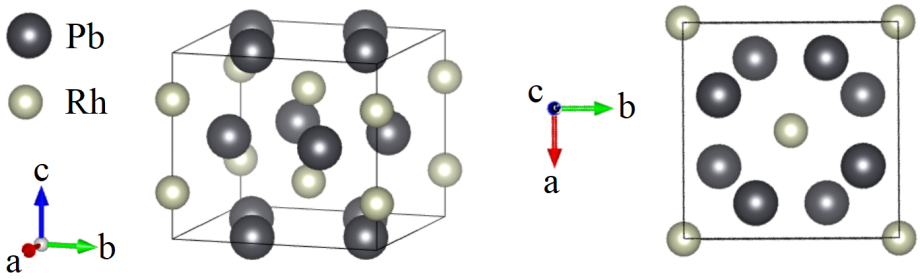

Figure 5.1: Tetragonal body-centred unit cell of $RhPb_2$ shown from two different angles, clearly displaying the body-centred structure, which is shared across the entire $CuAl_2(C16)$ materials class.

Recently too, a novel structural phase of $RhPb_2$, β-$RhPb_2$, has been theoretically predicted to be a TSC with $T_c = 9.7$ K [30]. This proposal draws from the discovery of

unconventional SC in β-$PdBi_2$ [29, 99, 196], a high-temperature phase of $PdBi_2$ forming above 380°C [197].

The theoretical structural polymorph β-$RhPb_2$ has been modelled with the same crystal structure as β-$PdBi_2$, in space group $I4/mmm$, and is proposed to host TSC based on the co-existence of a TI phase and bulk SC, forming a 2D TSC on the surface by the proximity effect [30]. Therefore there is a significant possibility of discovering TSC in a material closely related to the $RhPb_2$ phase, after realising and characterising the parent compound.

Overall then, $RhPb_2$ is identified as a promising material for study in this thesis. So far there is little experimental work regarding the material and the nature of the superconductivity in $RhPb_2$ is yet to be firmly established, leaving a broad landscape for investigation. Notably, only a statement of the critical temperature and has been previously reported [38, 39], along with confirmation of diamagnetic behaviour [38], and no normal state electronic transport properties have been investigated. Most recently the crystal structure of the material was re-investigated, confirming the $I4/mcm$ tetragonal structure with a small refinement to the unit-cell parameters [41].

5.1.1 Prospects of Topological Superconductivity in $RhPb_2$

In $RhPb_2$, the strong spin-orbit interaction conspires with crystallographic symmetries of the $I4/mcm$ space group to produce enforced band degeneracies at the P and N points of the Brilluoin Zone, shown in Figure 5.2a, where the effective Hamiltonian describing the degenerate bands takes a Dirac form [37, 40]. Noting that the Fermi level for $RhPb_2$ is close to the Dirac points at P and N, there is a significant possibility of TSC arising due to the combination of symmetry enforced degeneracies in the BZ and superconductivity.

Fundamentally two routes for non-trivial superconductivity exist in $RhPb_2$, following the work of Kobayashi and Sato [40]. The existence of the symmetry protected Dirac points leads to the emergence of non-trivial surface Fermi loops due to the bulk-boundary correspondence. Since these degeneracies are preserved during the transition to a superconducting state, bulk point-nodes of the superconducting gap and non-trivial Majorana modes should appear on the surface from these features, irrespective of the SC pairing symmetry. Additionally, the possibility of inherent odd-parity, topologically non-trivial pairing from *inter*-orbital attractive interaction arises due to the orbital de-

pendent non-trivial spin-structure of the Dirac bands, where another set of protected Majorana modes should appear.

The pairing symmetries of the superconducting state often vary between materials and there remains no clear consensus as how best to promote the emergence of intrinsic inter-orbital odd-parity pairs, even in materials with the pre-requisite ingredients [198–200]. Fundamentally, non-trivial orbital dependent spin structures are required alongside an inter-orbital attractive interaction, and phonon-mediated interactions are typically expected to be able to cause this [49].

As mentioned, there is very little literature regarding $RhPb_2$, including any exposition of the nature of the superconductivity or possible pairing mechanisms. Recently however, the normal state transport and superconductivity in iso-structural material $PdPb_2$ was investigated in detail [201]. The material shows Type-I superconductivity in single-crystal examples, which is mediated by an electron-phonon interaction of moderate strength. Measurements of the specific heat capacity of $PdPb_2$ show bulk SC behaviour consistent with isotropic s-wave behaviour.

Intriguingly, however, the T_c/T_F (Fermi temperature T_F) ratio introduced by Uemura [202–204] to characterise the degree of unconventionality in a superconductor falls in-between unconventional and conventional elemental Type-I superconductors [201]. This ratio is indicative of whether T_c falls in line with standard BCS expectations, where high n_s and low m^* (affecting T_F) typically have low $T_c \leq 10$ K, or whether similarities are found with heavy-fermion and unconventional superconductors with low n_s and high m^* but high $T_c \geq 10$ K [202–204].

In order to have some reference for comparison, it is anticipated that $RhPb_2$ should show similar behaviour to $PdPb_2$, since Pd ($Z = 46$) is simply replaced by Rh ($Z = 45$) in the same crystal structure. In-fact, band structure calculations [32, 35, 205, 206] show a similar landscape for both materials in Figure 5.2. From the partially occupied bands intersecting $E - E_F = 0$ eV, the Fermi surfaces of both materials are seen to be qualitatively similar: a central electron branch centred at Γ, with hole branches enclosing both the N and M points. Unfortunately, calculated examples of the phonon-dispersion relations are not available for these materials, however they share the same crystal structure and the unit cell parameters and atomic masses are only slightly changed between the two compounds, broadly implying similar phonon dispersion relations in each material [47].

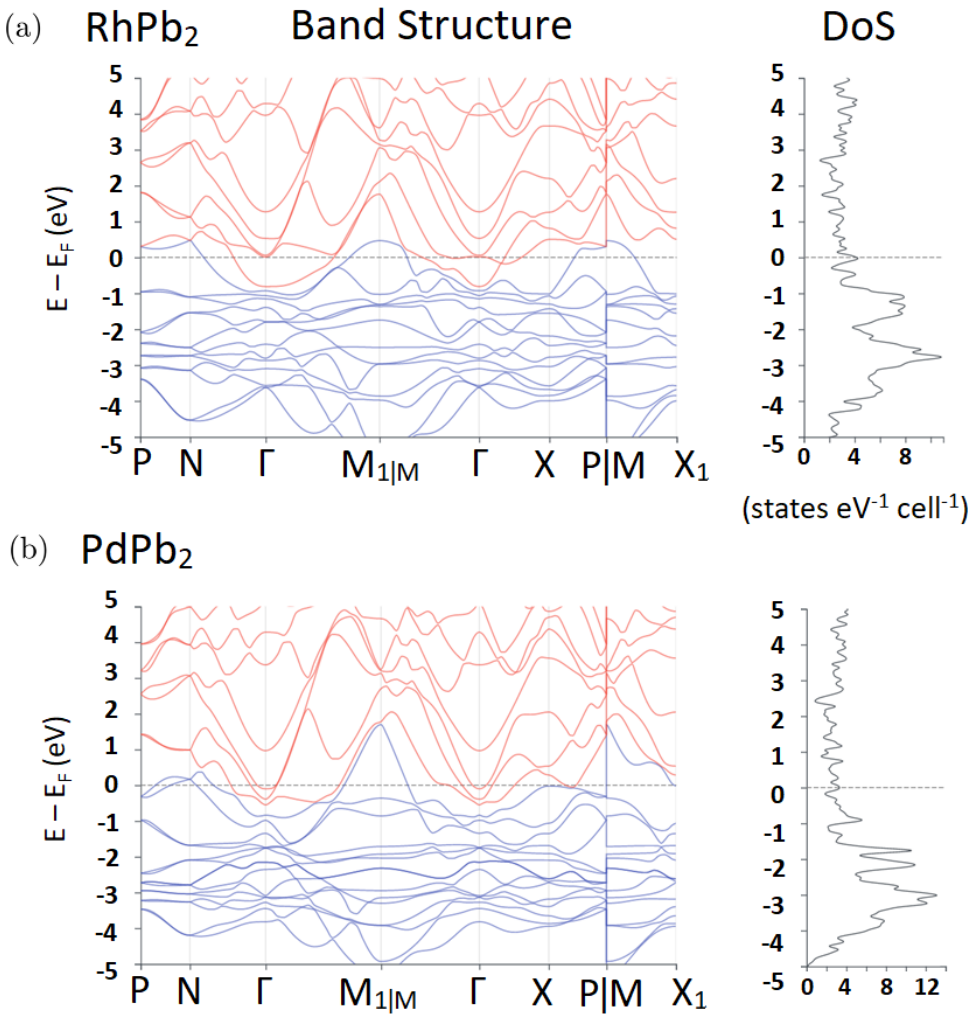

Figure 5.2: Details of the band structures of (a) $RhPb_2$ and (b) $PdPb_2$, taken from [32, 35]. Both show similar features and qualitatively similar Fermi surfaces are expected, importantly the symmetry enforced Dirac points at the P and N points in both materials open the possibility for TSC if inter-orbital attractive interactions are preferred.

Overall then, there is a significant possibility for the emergence of topologically protected point nodes in the surface superconducting state of $RhPb_2$, despite the suggestions from similar material $PdPb_2$ that conventional *s*-wave behaviour may be found. In any case, the requisite orbital dependent spin-structure exists on account of the symmetry protected Dirac points in $RhPb_2$, meaning an intrinsic odd-parity superconducting pairing may be stabilised depending on the preferred orbital interaction. In the long-term, alloying between $RhPb_2$ and $PdPb_2$ may allow for significant tuning of the chemical potential position relative to the Dirac points and ultimately may lead to fine-tuning of the superconducting state.

5.2 Material Synthesis

5.2.1 Choice of Growth Method and Initial Considerations

The literature regarding the growth of $RhPb_2$ is not comprehensive: to date only two references mention the growth method. In the first work electric arc heating was used to melt Pb and Rh together in an evacuated and argon purged environment to form a polycrystalline ingot of $RhPb_2$, the sample was then annealed at 450°C for 2 weeks before single phase samples emerged [195].

Consideration of the stability of Rh and Pb against common crucible materials suggests some difficulty in preparing $RhPb_2$ from the melt, since they are not both concurrently stable against common crucible materials [207–210]. The large difference in melting points also means that the incorporation of Rh may only be mediated by surface reaction and alloying with liquid Pb, at temperatures accessible with the furnaces available, which are below the melting point of Rh.

In fact, an initial attempt was made to grow $RhPb_2$ using a melt-growth technique with an atomic composition Rh:Pb 25:75, however some reaction of the material and quartz was apparent, and a solid formed with a melting point in excess of 1100°C, the highest temperature reachable in the furnaces available.

Despite this the second reported growth method, which was identified during the preparation of this thesis, successfully synthesised single-crystals of $RhPb_2$ [41] using a melt-growth technique with quartz ampoules, despite the possibility of reaction of Rh with Si and SiO_2 to form various silicides [207]. That study [41] used powdered Rh and a Pb-rich liquid solute in an initial mixing phase to pre-react the Pb-Rh [41].

From the initial consideration of phase stability and mixing limitations, DC-sputtering of thin films was chosen as the synthesis method, since layer-by-layer deposition techniques allow for buffer layers to chemically protect the forming phase, and either intermixed or thin layer repeating units of deposited material can be mixed with annealing to form the desired phase. Thin-film examples of TSC candidates are also highly desirable since device architectures, such as Josephson Junction devices [27], can be fabricated to test the fundamental properties of the superconducting pairing symmetry and investigate the implementation of Majorana braiding for topological quantum computing applications.

The phase diagram in Figure 5.3a shows that $RhPb_2$ melts incongruently and that a Pb rich liquid-solute is needed to crystallise the correct phase [211]. Since sputtering thin films and annealing does not rely on liquid-to-solid formation, rather the inter-diffusion of Rh and Pb atoms below the melting point of the material, it is expected that compositions close to the desired phase should, on complete mixing, produce a thin-film with the correct composition. Figure 5.3b shows the composition dependence of the Gibbs free energy in the binary Rh-Pb system [194, 212, 213], which shows the possibility of two stable impurity phases, Rh_4Pb_5 and RhPb, both of which are more energetically favourable to form than the desired $RhPb_2$ phase. Based on this, compositions that are slightly Pb-rich may promote the desired phase, since more Rh-rich compositions may preferentially form Rh_4Pb_5 or RhPb.

With the ability to deposit multiple samples in the same growth environment, the 16-sample DC sputtering system at the University of Leeds is used, which allows the deposition of a single material layer at a time. There are some systems capable of co-depositing materials at the University of Leeds, this was not initially pursued since an appropriately sized Rh target was not available for use in one system, also superconducting thin-films of Pb had been successfully grown in the system used [126, 214], and there were some concerns over the quality of the vacuum for growing superconducting films requiring Pb in another system capable of co-deposition.

A multilayer structure of repeating Pb-Rh-Pb blocks is instead targeted, where post-growth annealing will mix the layers and ultimately produce a homogeneous film of the targeted phase. A schematic of the films grown in this work is shown in Figure 5.4. Thin layers are targeted to promote more complete inter-diffusion of the layers with annealing and encourage the desired phase to form. Rh is sandwiched between two

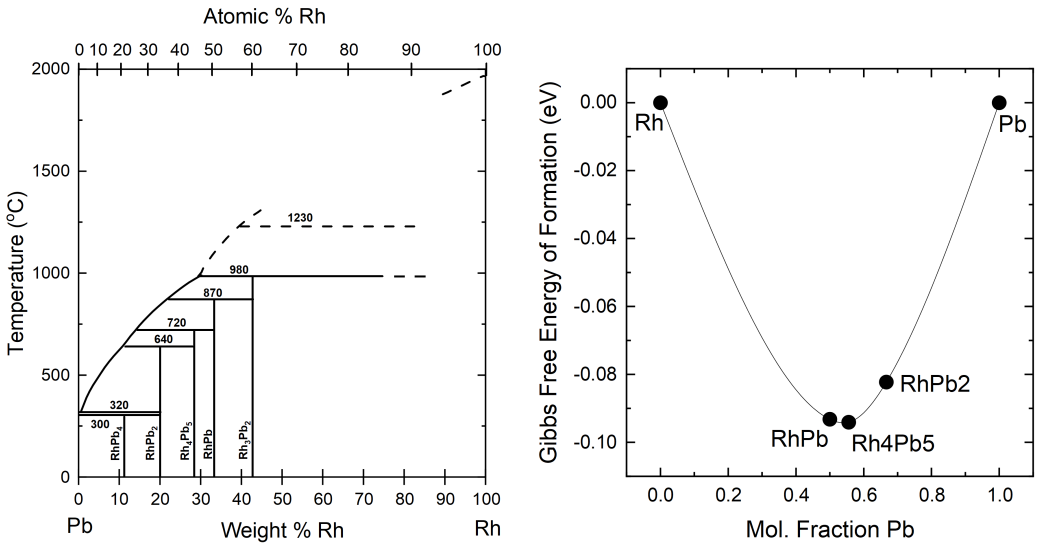

(a) (b)

Figure 5.3: Detail regarding phase formation in the Rh-Pb system. (a) Binary phase diagram for the Rh-Pb system with details of different phases [211]. (b) Composition dependence of the Gibbs free energy of formation, showing the only three stable phases in this binary system are RhPb, Rh_4Pb_5 and $RhPb_2$ [194].

identically thick layers of Pb to help promote symmetric alloying of the Rh from each side during the initial mixing phase of annealing, which should promote homogeneous phase formation across the entire film.

The nominal composition of the films is controlled by changing the thickness of the Rh in the multilayer. The targeted Pb multilayer thickness (10 Å) and layers of Rh (3 - 5 Å) should correspond to a nominal composition range for $RhPb_x$ of $1.53 \leqslant x \leqslant 2.56$. A composition range is grown around the targeted composition, since variances in layer roughness or exact thickness may affect the exact stoichiometry of the film and so phase formation.

The average number of atoms contained in a certain layer thickness can be calculated with knowledge of the unit cell size and type, allowing control for the number of atoms and so stoichiometry in a multilayer unit. For example the Pb unit cell is face centred cubic (FCC) containing 4 atoms with 4.95 Å lattice constant [215], meaning a 10 Å layer of Pb contains $\frac{10}{4.95} = 2.02$ unit cells, and so $2.02 \times 4 = 8.08$ atoms. Accordingly, for $RhPb_2$, a 4 Å layer of Rh (FCC, $a = 3.80$ Å [216]) contains 4.2 atoms, giving a ratio of Pb:Rh of 8.08:4.2, and a composition $RhPb_{1.92}$.

Since Rh may react with Si/SiO_2 [207], a 50 Å Ta layer is grown first to prevent reaction, followed by a 50 Å Rh layer to prevent any incorporation of Ta into the forming $RhPb_2$. The possibility of Rh-Ta mixing is considered later and found to be insignificant. The multilayers are capped by a 100 Å Rh layer to protect the forming phase from oxidisation whilst annealing. The films' lateral sizes are roughly 20 × 20 mm after growth, these are then cut into smaller segments (4 × 4 mm) to be annealed. Some intermixing of the Rh buffer and cap is anticipated with annealing, which is also considered later and is again found to be insignificant relative to the thickness of the forming $RhPb_2$, also confirming that no significant impurity phases are forming.

Empirically, most superconducting materials display a suppression of T_c below a thickness of $\sim$ 10 nm [217]. The exact details however depend on a number of different effects [218, 219] and superconductivity has even been found in mono-layer films of Pb [220, 221]. Below 10 nm there are also usually significant increases in the resistivity of metals due to a combination of smaller grain sizes, so increased grain boundary scattering, more significant surface scattering, and in even smaller structures quantum confinement effects [222]. From this, the total thickness of the $RhPb_2$ films is chosen to avoid suppression of T_c in the $RhPb_2$ film and avoid increased resistivity, with thin

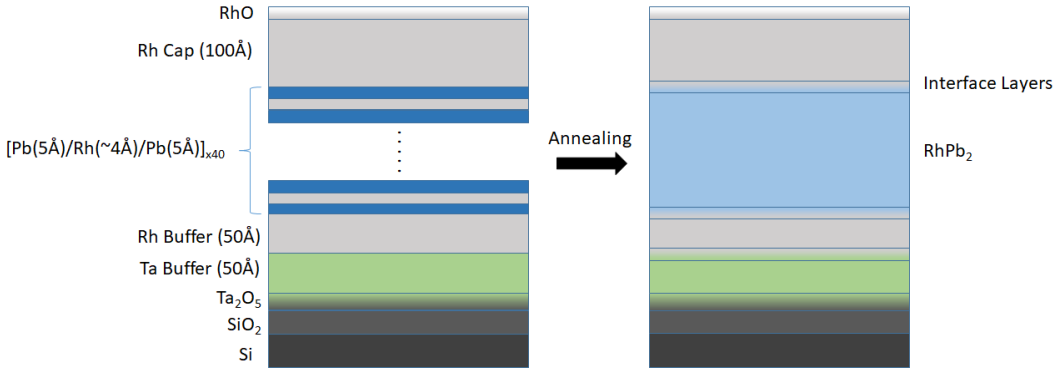

Figure 5.4: Schematic of the multilayer films grown in this work, showing the desired result with annealing where the repeated layers are mixed and crystallise into the $RhPb_2$ phase.

Ta/Rh buffer and cap layers so that they have high resistance and give negligible contributions to the electronic transport.

Specifically, the resistivity of standalone Ta/Rh buffer and Rh cap structures deposited on SiO_2 with the same growth conditions as the $RhPb_2$ films are measured at room temperature to be 35 and 21 $\mu\Omega$.cm, and at 4.2 K to be 31 and 17 $\mu\Omega$.cm, leading to resistances in a typical film of 20 - 30 Ω. The typical resistance of the total film with annealed $RhPb_2$ is measured to be 0.5 - 1 Ω, implying that $R_{Total} \approx R_{RhPb2}$ in the parallel resistor stack. The thin Ta layer should also have heavily suppressed T_c from the bulk value, which is expected to be below 500 mK [223]. The possibility of superconducting Ta, and other components of the thin-film other than $RhPb_2$, are considered in more detail later.

The targeted thickness d of the films is 100 nm, following the comparison to $PdPb_2$ (BCS Coherence length $\xi_0 = 200$ nm, London penetration depth $\lambda_L = 50$ nm) this will likely place a clean example of $RhPb_2$ in the 2D regime of superconductivity, since ξ_0, $\lambda_L \geq d$, which is considered whilst measuring the magnetic properties of the films.

The effects of substrate and buffer layer on the formation of $RhPb_2$ are now considered. First, Si with a thin and amorphous layer of native SiO_2 oxide layer is selected as the substrate material, since it should provide a smooth surface for ensuing deposition. XRR shows that the Rh buffer layer has close to 10 Å roughness, so is still a smooth layer for deposition. Since there should be no epitaxial growth of Ta or Rh on the SiO_2 layer, there should be no epitaxy in the $RhPb_2$ film. Both Ta and Rh

have been shown to order into a dominant (111) orientation out-of-plane after annealing treatments [224, 225], which generally occurs to minimise the energy of the system [125]. The annealing treatment used to form the $RhPb_2$ phase is expected to allow the system to relax into a dominant single texture [125].

5.2.2 Film Deposition and Initial XRR Characterisation

Figures 5.5 summarises the XRR scans of non-annealed multilayers, with an example of the fitted curves overlaid assuming an initial stack of the form given in the schematic in Figure 5.4. Table 5.1 summarises the changing Rh multilayer parameters determined from fitting and converts the layer thickness' to a nominal composition. The average total Pb thickness in each multilayer unit is 20.75 ± 0.3 Å, with good reproducibility between films.

In all cases the repeating layer thickness is slightly larger than targeted, which likely arises from the finite time it takes for the shutter wheel and sample to move over each sputter target, the effect compounding for the repeated Pb layers in each unit. The additional amount of Pb is ≈ 10 Å, and the additional amount of Rh is ≈ 2 Å. Due to this the films thickness' are expected to be 107 nm and the nominal compositions are slightly Pb-rich, which as mentioned may aid the formation of $RhPb_2$ based on the Gibbs free energy.

The roughness of the Pb layers is 4.6 ± 0.2 Å , with similar values found for the Rh layers. Since the roughness scale is comparable to the layer thickness there is likely some intermixing which should benefit the phase formation. The Bragg peaks arising from the repeating multilayer units are still well-defined however, which suggests that the layers and interfaces are still well-defined.

The densities during fitting were fixed at the bulk values for each material. The layer roughness may in fact be less than that reported if the density of the layers was taken as a fitting parameter and turned out to be lower than the bulk values. This may explain why the Bragg peaks are still well defined despite the high level of roughness compared to the layer thickness.

Table 5.2 summarises the remaining layers' properties, which are consistent across all the films grown, shown by the small standard deviation. Figure 5.6 shows the manual Kiessig fit to the long period oscillation present in Figure 5.6 confirming that they arise from a layer of 100 Å thickness, which is the Rh cap. Distinct oscillations

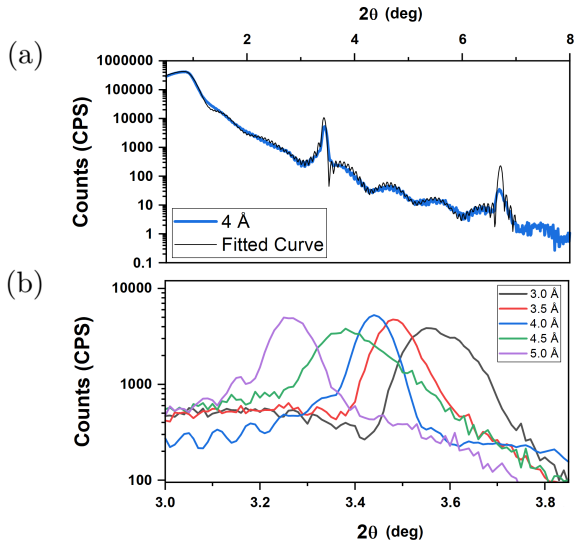

Figure 5.5: Initial XRR characterisation of the DC sputtered films (a) Example of fitted XRR data for film and (b) the changes of Bragg peak position, arising from the repeating layer unit, when changing the growth time and so thickness of the repeating Rh layer.

Rh Target (Å)	Rh Actual (Å)	Rh Roughness (Å)	Nominal Composition $RhPb_x$
3	5.0 ± 0.2	4.3 ± 0.2	3.2 ± 0.1
3.5	5.5 ± 0.2	4.9 ± 0.2	2.9 ± 0.1
4	6.0 ± 0.2	4.1 ± 0.2	2.65 ± 0.09
4.5	6.2 ± 0.2	5.0 ± 0.2	2.55 ± 0.09
5	6.9 ± 0.2	4.9 ± 0.2	2.30 ± 0.07

Table 5.1: Summary of Rh layer thickness found by fitting. The average Pb thickness of all films is used to calculate the nominal composition.

Layer	Thickness (Å)	Std. Dev. (Å)	Std. Err.	Roughness
SiO_2	32	8	3	8 ± 1
Ta_2O_5	25	14	6	2 ± 1
Ta Buffer	53	6	3	9 ± 1
Rh Buffer	52	2	1	11 ± 2
Rh Cap	98.1	1	0.6	2 ± 1
RhO	7.4	1	0.5	3.6 ± 0.2

Table 5.2: Fitting parameters for the layers present in all the films grown, showing the variance between films by the standard deviation.

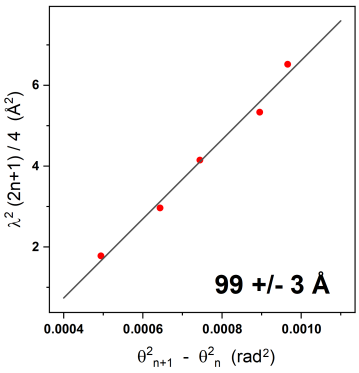

Figure 5.6: Kiessig fit to the long period oscillations in the XRR that arise from layers of 100Å thickness.

are not visible by eye from the buffer layers, however these are revealed by fitting to be close to the intended thickness across all the films.

5.2.3 Annealing Investigation and $RhPb_2$ Phase Formation

Since there is limited information available concerning the formation of $RhPb_2$ an initial annealing investigation was performed using an in-situ vacuum ($\approx 10^{-1}$ mbar) heater stage on the XRD system which allows for direct observation of the phase development with annealing, which is summarised in Figures 5.7a and 5.7b. It was found that 450°C is high enough temperature to mix and react the layers, as seen by the decreasing amplitude and disappearance of the low angle Bragg peak in Figure 5.7a, where all scans are taken immediately after reaching temperature. This reaction is shown by the

emergence of a diffraction peak close to 41 degrees, which increases in amplitude and settles to a position of 41.4 degrees at 450°C in Figure 5.7b.

Annealing in a cleaner environment, Ar purged and evacuated ($P \approx 10^{-2}$ mbar) quartz tubes, and measuring the samples at room temperature shows that this XRD peak stabilizes after 1 hour, and remains stable for up to 5 hours in Figure 5.7c. The high-angle XRD in Figure 5.7d confirms that this is the only diffraction peak present in the sample after the initial mixing, with a match to both the (201) and (226) peaks of RhPb and Rh_4Pb_5 respectively [226]. The resistivity of this sample was measured down to 380mK, shown later in Figure 5.21b, however no SC transition was observed.

Given that the energy of phase formation is lowest for Rh_4Pb_5 and the composition is closer to this phase than RhPb, it is expected that the Rh_4Pb_5 phase initially forms in the films and further annealing is required to re-crystallise the deposited material into $RhPb_2$.

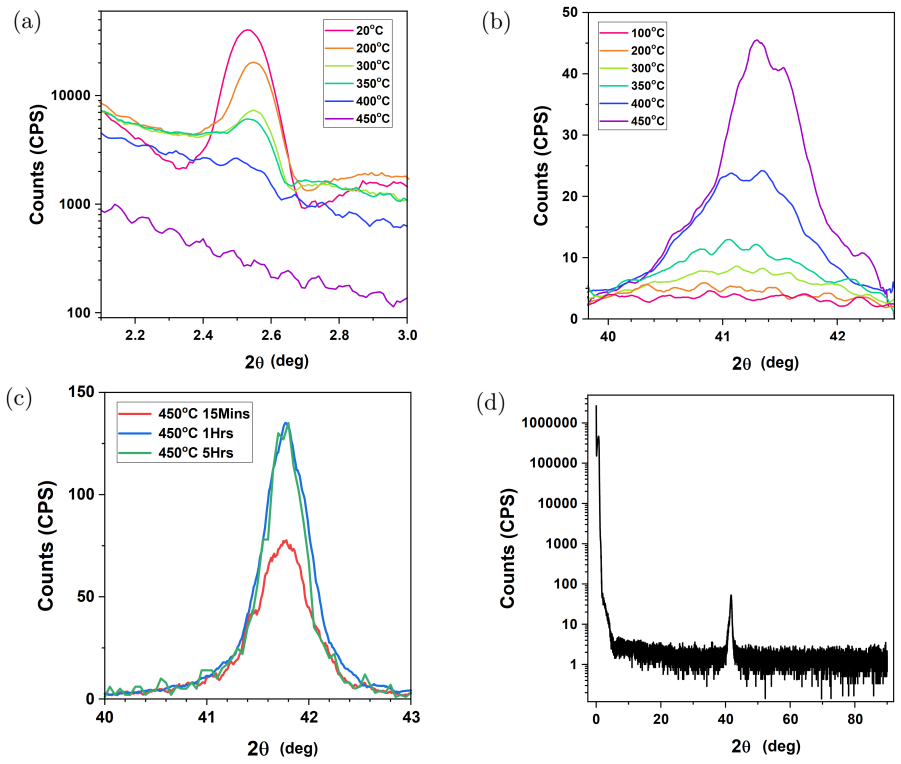

Figure 5.7: Progressively increasing the annealing temperature with in-situ annealling in (a) and (b) shows that 450°C is high enough temperature to completely mix and react the repeating layers, as seen by the removal of the low angle Bragg peak in (a), which (b) leads to the ordering of an initial phase. (c) Annealing in a cleaner environment shows the emergence of the same single phase which is stable up to 5 hours. (d) A single phase is identified, consistent with both RhPb (201) and Rh_4Pb_5 (226) diffraction peaks.

To investigate re-crystallisation longer annealing times were used: Figure 5.8a shows that at some point between 5 and 24 hours of annealing the films show a clear change in the XRD pattern, from a single dominant peak to two roughly equivalent intensity peaks at 40.8° and 42.1°. These peaks remain stable at least up to 100 hours, suggesting this is the most energetically favourable phase. In fact, annealing a nominally identical sample with a thin Al_2O_3 cap instead of Rh shows only the peak at 40.8° in Figure 5.8b, suggesting that the Rh cap crystallises into the (111) orientation as expected and

is responsible for the peak at 42.1°. Importantly, the remaining peak corresponds to the expected (202) orientation of $RhPb_2$ [41], meaning single-texture thin films have formed after the recrystallisation. For reference, Figure 5.9 shows the standard pattern of XRD peaks for $RhPb_2$ with structural parameters from Ref. [41].

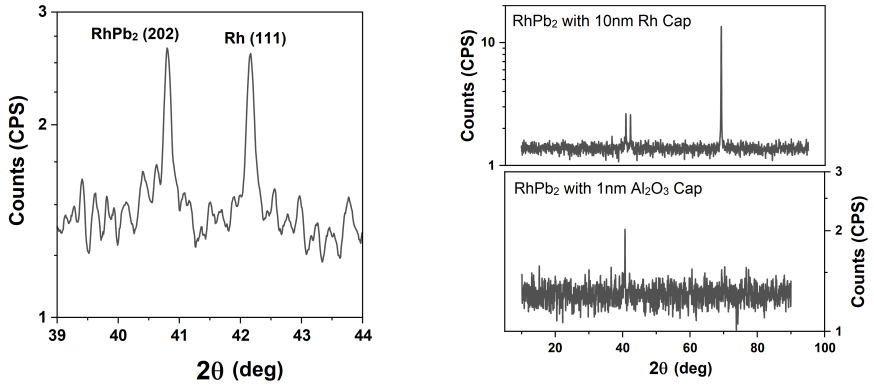

(a) (b)

Figure 5.8: (a) Evidence for recrystallisation into $RhPb_2$ after annealing for 24 hours in a clean environment. (b) Comparison of film with and without Rh cap, showing that the 42.1° peak is due to the (111) orientation of Rh, so (202) single-texture $RhPb_2$ has formed after re-crystallisation.

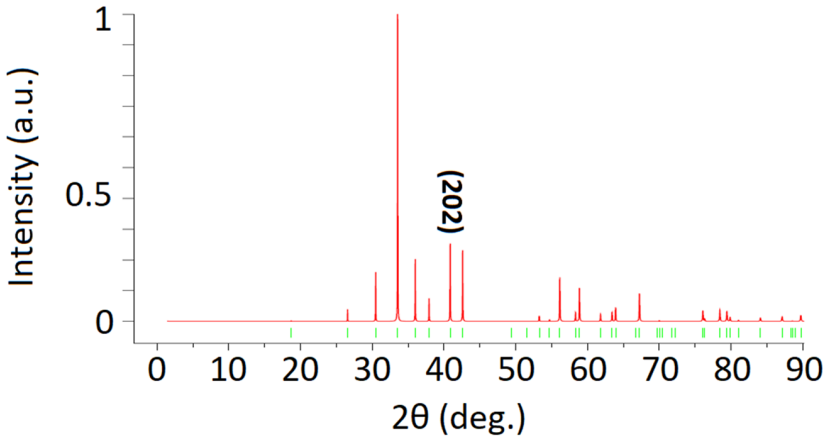

Figure 5.9: Standard XRD peaks for $RhPb_2$ shown up to 90 degrees, with the (202) orientation peak labelled. This data was produced based on the structural parameters reported in Ref. [41].

Figure 5.10a shows that annealing at 450°C for 24 hours forms the desired phase across the entire nominal composition range grown, for $2.3 < x < 3.2$ in $RhPb_x$, but with some significant changes in the total phase strength. Figure 5.10b shows the dependence of XRD peak area and so phase strength on the nominal composition, showing that the maximum $RhPb_2$ phase formation here is for $x = 2.65$. The connecting line is a spline function and suggests the phase formation is essentially optimised in composition here.

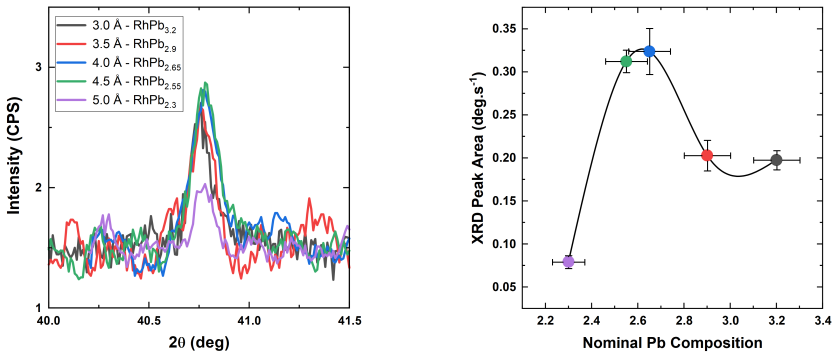

(a) (b)

Figure 5.10: Composition dependence of $RhPb_2$ phase formation (a) High angle XRD of the (2 0 2) $RhPb_2$ peak for changing nominal composition. (b) Peak area, extracted by Lorentz fit, dependence on nominal composition. Connecting line is spline interpolation, suggesting $RhPb_{2.65}$ is the optimised composition.

Considering the possibility of extra Rh mixing from the cap and buffer layers with annealing, Figure 5.11a shows the low-angle XRR scan of the $RhPb_{2.65}$ film annealed at 450°C for 24 hours, where the long period oscillation arising from the Rh cap is still visible. The inset of Figure 5.11a shows the Kiessig fit of these oscillations, suggesting a similar Rh cap thickness to before annealing. Figure 5.11b shows the fitted curve based on the annealed structure from the schematic in Figure 5.4, with fitting parameters summarised in Table 5.3. Figure 5.11c shows a section of short period oscillations arising from the thick $RhPb_2$ layer which are also captured by the fitting, the inset Kiessig plot confirms a total thickness close to 1100 Å. The XRR fitting and Kiessig plots confirm that the Rh buffer and cap layer thickness' have essentially remained the same after the annealing process: thin inter-mixing layers have formed at the interfaces

with the $RhPb_2$, which likely produce a negligible change in the overall composition of the $RhPb_2$ layer. The thickness of the Ta layer has remained roughly constant after annealing, suggesting negligible reaction with the substrate oxide layer or Rh.

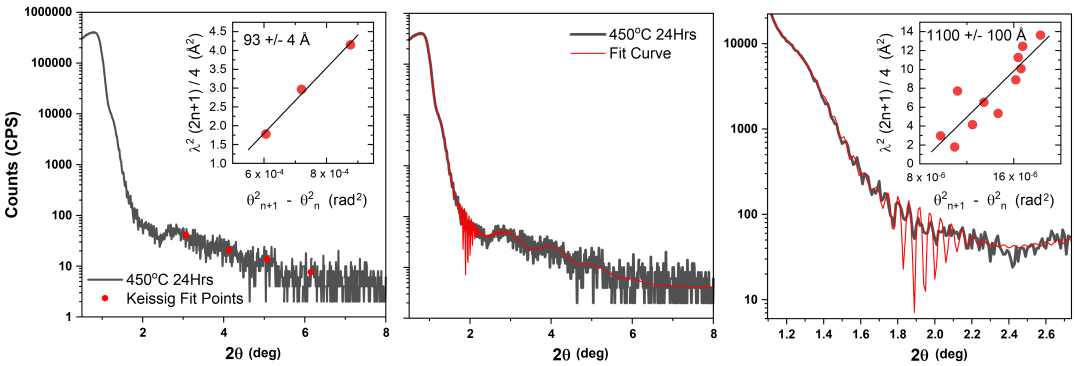

(a) (b) (c)

Figure 5.11: (a) XRR data for $RhPb_{2.65}$ film after recrystallisation, showing a long period oscillation arising from a 100 Å thick layer, suggesting minimal reaction of the Rh cap, and by extension the Rh buffer layer, with the forming $RhPb_2$. (b) Full fitting of the XRR profile for film annealed at 450°C, fitting parameters are shown below in Table 5.3. (c) Focus on short period oscillations arising from the $RhPb_2$ layer, with inset Kiessig plot confirming the accuracy of the full fitting profile.

Layer	Thickness (Å)	Roughness (Å)
SiO_2	16 ± 3	7 ± 1
Ta_2O_5	15 ± 3	11 ± 1
Ta Buffer	54 ± 2	4 ± 1
Ta/Rh Mix	10 ± 1	4 ± 1
Rh Buffer	30 ± 2	13 ± 2
Rh/$RhPb_2$ Mix	4 ± 1	13 ± 1
$RhPb_2$	1099 ± 6	23 ± 1
$RhPb_2$/Rh Mix	8 ± 2	12 ± 1
Rh Cap	100 ± 1	13 ± 1
RhO	22 ± 2	15 ± 1

Table 5.3: Fitting parameters for the layers after annealing, confirming minimal change in the Rh buffer and cap layer thickness compared to non-annealed films.

Concluding, single-texture (202) films of $RhPb_2$ have been successfully grown on a Rh buffer layer using DC sputtering and an annealing protocol. Annealing at a temperature of 450°C in Ar purged and roughing pump evacuated quartz tubes is sufficient to mix and react layers of Rh and Pb into an initial Rh_4Pb_5 phase, which then recrystallises into $RhPb_2$ after 24 hours annealing time. A Pb-rich composition is found to optimise to phase strength, which shows significant variance in the nominal composition range $2.3 < x < 3.2$ in $RhPb_x$. XRR of the annealed films confirms minimal inter-diffusion of the Rh buffer and cap layers, and that the thickness of the $RhPb_2$ layer is consistent with the initial amount of Rh and Pb deposited.

Overall, we find that a nominal composition of $RhPb_{2.65}$ leads to the largest $RhPb_2$ (202) orientation XRD peak area, after annealing at 450°C for 24 hours. In the next three sections, measurements are presented for the film with this nominal composition. We note that a downturn in resistivity is observed with the same magnitude and onset temperature in the films with nominal composition $RhPb_{2.55}$, but the strongest phase sample was measured in more detail and so is presented here.

5.3 Electronic Characterisation

5.3.1 Transport Properties

Since $RhPb_2$ has minimal characterisation in the literature, this section aims to determine the basic transport properties of the material in thin film form, and search for any indication of the predicted Dirac semi-metal phase.

Figure 5.12 summarises the basic transport measurements for $RhPb_{2.65}$ annealed at 450°C for 24 hours. Field is applied out of plane. All uncertainties are taken from the VdP equations considering the finite size of the contacts and misalignment [132], since these are larger than the numerical uncertainties from Ref. [133]. Errors in ρ_{xx} are $< 0.2\%$, and in ρ_{yx} are $< 3\%$.

The electronic transport measurements show that the thin-film $RhPb_2$ is overall metallic with decreasing resistivity with reducing temperature, and at 1.5K shows a linear Hall resistivity with field consistent with single band transport, and B^2 MR determined by the general fitting form. From the slope of the Hall resistivity hole dominant transport is found with a high carrier density of $(1.52 \pm 0.05) \times 10^{23}$ cm^{-3}. The scale of the MR is small, so does not suggest compensated bands as is usually

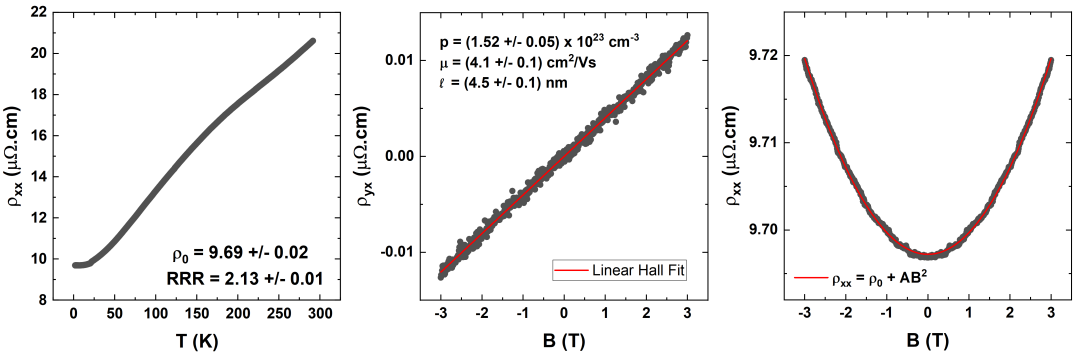

(a) (b) (c)

Figure 5.12: Basic electronic characterisation of $RhPb_2$ films. (a) Longitudinal resistivity shows metallic temperature dependence with downward curvature at higher temperatures. (b) Hall resistivity with field shows linear, positive slope, showing dominant hole transport with $p = 1.5 \times 10^{23}$ cm^{-3}. (c) Perpendicular MR shows quadratic dependence on field.

observed in many Dirac semi-metals, and may be expected in $RhPb_2$ based on the partially occupied bands in the calculated band structure in Figure 5.2a.

From the values of ρ_0 and p at 1.5K the mobility is estimated as (4.1 ± 0.1) cm^2/Vs, using a single band model consistent with the observed Hall effect, with: $\mu = \frac{1}{pe\rho_0}$. Using the relations $\mu = \frac{q\tau}{m^*} = \frac{ql}{m^* v_F}$ and $v_F = \frac{\hbar k_F}{m^*}$ with the assumption of a spherical Fermi surface with wave-vector $k_F = \left(3\pi^2 p\right)^{1/3}$, the mean free path of the carriers can be calculated as $l = \frac{\hbar k_F \mu}{q}$, which is estimated as (4.5 ± 0.1) nm.

To look for other signatures of the Dirac nature, Figure 5.13 shows the angular dependence of the MR at 3T, with B applied in the plane of the sample. This is performed to search for an indication of negative MR when $B \parallel I$ as has been reported as evidence of charge pumping between Dirac cones when spin degeneracy is lifted by the magnetic field [57]. The sample is rotated from $B \perp I$ at 10 degrees to $B \parallel \pm I$ at -80 and 100 degrees, showing only positive MR. This suggests that at present, a trivial bulk-band is dominating the transport properties.

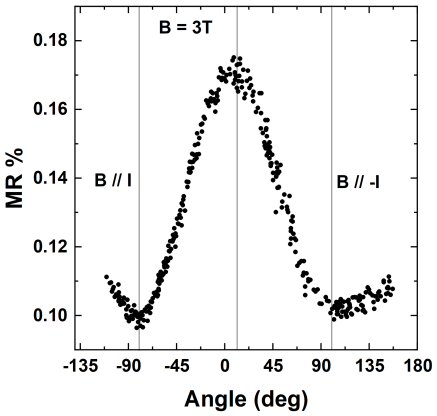

Figure 5.13: Angular dependence of the MR with B applied in-plane, showing no evidence for negative MR with $B \parallel I$.

5.3.2 Resistivity Dependence on Temperature

To reveal some information regarding the dominant scattering mechanism in the $RhPb_2$ films, the temperature dependence of the resistivity is considered. First we focus on the low temperature regime, then separately consider the observed curvature at higher temperatures.

Low Temperature

Generally, the resistivity in the low temperature region of a metallic system can be fit to a power law dependence:

$$\rho(T) = \rho_0 + AT^n \tag{5.1}$$

where n is taken as a fitting parameter that is dependent on the dominant scattering mechanism [227]. For electron-phonon scattering mechanisms, $n = 3$ is predicted for inter-band $s - d$ scattering which is often prevalent in transition metal compounds are their alloys [228], and $n = 5$ is predicted for intra-band scattering which often describes s-shell valence metals [47]. Usually, the phonon momenta required to cause s-d scattering is larger than s-s scattering, and s-d scattering becomes more dominant at higher temperatures [228, 229].

Some materials display a temperature dependence closer to $n = 2$, which may arise due to dominant electron-electron scattering effects [47, 230, 231], or from non-Debye like phonon-assisted s-d inter-band scattering [230]. Through Matthiessen's rule, these

scattering mechanisms may all contribute simultaneously, leading to non-integer values of n.

With increasing temperature the resistivity of non-magnetic metals moves to scale linearly with temperature, on account of the number of excited phonon modes scaling linearly with T [47]. The full resistivity curve may be described by the Bloch-Gruneisen (BG) equation:

$$\rho(T) = \rho_0 + \frac{k\lambda_{BG}\Theta_D}{\hbar\omega_p^2}(4\pi)^2\left(\frac{2T}{\Theta_D}\right)^n \int_0^{\Theta_D/2T} dx \frac{x^n}{\sinh^2(x)} \tag{5.2}$$

where the exponent $n = 5$ is usually taken, defining intra-band phonon mediated scattering as the dominant mechanism [232–235]. Other fitting parameters are the Debye temperature Θ_D and the electron-phonon coupling constant λ_{BG}, for fixed values of the residual resistivity ρ_0 and the Drude plasma frequency ω_p. The value of λ_{BG} is dependent on the value of the Drude plasma frequency since both contribute to the slope of the resistivity when linear with T, meaning only the values of Θ_D can be reliably determined without knowledge of ω_p [233, 234].

First, the low-temperature regime of the resistivity is fit to the general expression with n as a fitting parameter. Low temperature is defined by the region of the resistivity before the cross-over to linear behaviour starts to occur [227]: this is identified as $\approx T \leqslant 25$ K using the derivative of the resistivity in Figure 5.14a, above which the slope starts to decrease. To determine any variance of n with increasing temperature the fit is performed over different temperature ranges with the lower limit fixed at 1.5 K, finding reliable fits above an upper limit of 13 K up to 27.5 K. Figure 5.14b shows n plotted against the upper temperature fitting limit, finding that a T^5 dependence describes the data correctly up to ≈ 17 K, above which the exponent starts to decrease. Above an upper fitting limit of 30 K the simple expression fails to fit the data well. To further check this dependence Figure 5.14c shows the resistivity plotted against T^5, with dashed lines showing 5 K intervals up to 25 K, where there is a clear linear dependence on T^5 up to 17 K.

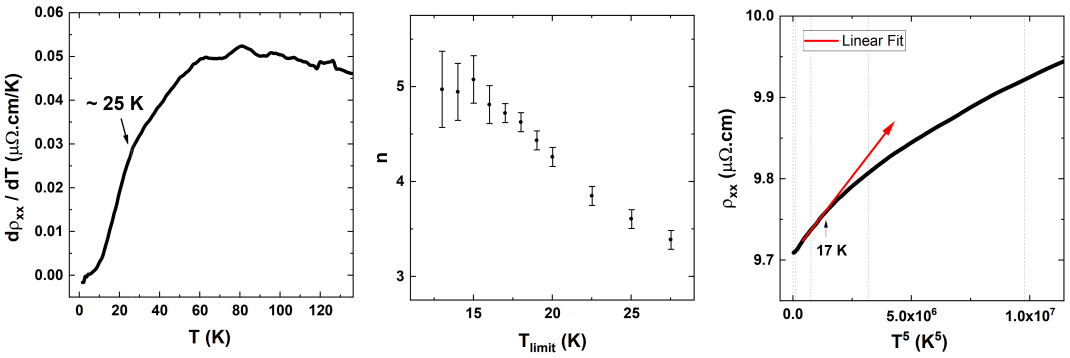

(a) (b) (c)

Figure 5.14: (a) First derivative of the resistivity dependence on temperature, identifying the low-temperature regime as below 25 K. (b) Temperature exponent n determined from fitting the resistivity to the simple, general model for increasing temperature range. (c) Resistivity plotted against T^5, showing a departure from linear behaviour close to 17 K.

Applying the full BG equation in the low-temperature regime ($T \leqslant 25$ K) produces good agreement with the general expression, finding this region to have dominant T^5 behaviour. The fit is shown in Figure 5.15a, finding $n = 4.9 \pm 0.2$, with $\Theta_D = 140 \pm 4$ K, consistent with that previously determined in $PdPb_2$ ($\Theta_D = 152 \pm 1$ K) [201]. The determined values of n and Θ_D remain the same with fitting up to $T = 40$ K, shown by the dashed line in Figure 5.15a. Above this temperature the exponent n again starts to decrease.

Given the transition metal (Rh) d-electron valence orbitals involved in the chemical bonding in $RhPb_2$, there may be some move to T^3 dependence with increasing temperature. The decreasing value of n with increasing temperature seems to suggest this, and Figure 5.15b shows the resistivity plotted against T^3, which produces a linear trend up to 28 K.

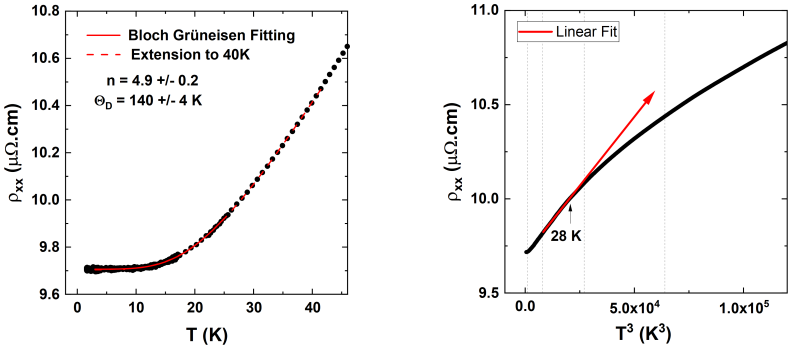

(a) (b)

Figure 5.15: (a) Fitting the resistivity dependence on temperature to the Bloch-Gruneisen equation, confirming a dominant T^5 behaviour at low temperature and allowing extraction of the Debye temperature for $RhPb_2$ as $\Theta_D = 140 \pm 4$ K. (b) Resistivity plotted against T^3, suggesting an increasing dominance of inter-band scattering with increasing temperature, consistent with the transition metal nature of $RhPb_2$.

Overall then, the resistivity dependence on temperature, at least up to 40K, seems well described by the conventional electron-phonon scattering mechanisms for transition metal compounds, with a cross-over from dominant T^5 to T^3 behaviour with increasing temperature.

High Temperature Resistivity

With increasing temperature, the resistivity tends towards linearity as expected, however above 140 K there is some significant downwards curvature. This is also observed in single-crystal samples of $PdPb_2$ [201]. There are many proposed mechanisms for this effect in non-magnetic materials [236, 237]. The first explanations were based on the idea of a minimum mean-free path, leading to a maximum 'saturation' value of the resistivity, it is called resistivity saturation.

A parallel-resistor model has been previously applied at high-temperatures to describe the behaviour [201, 236, 237]:

$$\rho(T) = \left[\frac{1}{\rho_s} + \frac{1}{\rho(T)}\right]^{-1} \tag{5.3}$$

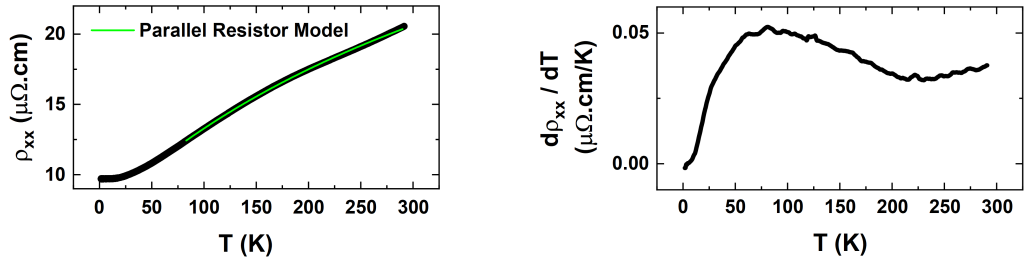

(a) (b)

Figure 5.16: (a) High temperature regime of the resistivity with the phenomenological saturating resistivity model applied, shown by the green line. Some additional upwards curvature is present in the resistivity above ≈ 215 K that is not completely accounted for, shown by (b) the derivative of the resistivity with respect to temperature.

where $\rho(T) = \rho_0 + \rho_i T$, with residual resistivity ρ_0 and ρ_i describing the slope of the ideal high-temperature linear dependence of the resistivity in units of $\mu\Omega$.cm/K. Despite the name, the resistivity may not necessarily reach a constant value at high-temperature, there is also not a physical parallel transport channel in the material: the model has simply been formulated as an empirical/phenomenological description of the saturating behaviour [236, 237].

The high temperature behaviour is fitted to this parallel-resistor model for $T \geqslant 80$ K and shown in Figure 5.16a, for fixed $\rho_0 = 9.7$ $\mu\Omega$.cm, the value for $\rho_s = 43.1 \pm 0.3$ $\mu\Omega$.cm and $\rho_i = 0.107 \pm 0.001$ $\mu\Omega$.cm/K. The simple saturation model describes the resistivity well up to ≈ 215 K, however some additional curvature is present in the resistivity above this, shown by the derivative in Figure 5.16b, that is not completely accounted for.

5.4 Superconductivity in $RhPb_2$ Thin Films

5.4.1 Onset of Superconductivity

The film with nominal composition $RhPb_{2.65}$ with the largest (202) XRD peak area was taken for measurement in a ^{3}He 'Heliox' cryostat insert, capable of cooling the sample to ≈ 380 mK. Figure 5.17a shows the resistivity dependence on temperature for this

sample below 10 K, with a clear resistance downturn at low temperature.

Previous works have identified the superconducting critical temperature of $RhPb_2$ as 2.7 K [39] and 1.32 K [38, 195]. The work finding $T_c = 1.32$ K extracts the critical temperature as the midpoint of the magnetic susceptibility transition to the superconducting state. In our work a complete transition to a zero resistance state is not observed so such a mid-point cannot be defined. Instead, the onset temperature of the resistance downturn is quoted as T_c here.

We define the onset temperature as the intersection point of the residual resistivity to the tangent of the resistivity transition, shown in Figure 5.17b, finding $T_c = 1.4 \pm 0.1$ K. The uncertainty is estimated from the approximate range of intersection points given by the noise in the data. Notably, an onset temperature of 1.4 K is consistent with the previous determination of a mid-point T_c of 1.32 K [38].

Unfortunately, only a partial resistance drop is observed: only a 0.01% drop in resistance is observed over a 1 K reduction in temperature, or 70% of T_c. The capability to measure the film's magnetisation below 1.8 K is not available at the University of Leeds and so observation of Meissner screening is also not currently possible to further confirm that this downturn is due to the onset of the superconducting state. This is also true of heat capacity measurements, so the expected discontinuity in the electronic component of the specific heat across the superconducting transition cannot currently be observed either. Instead, the field dependence of the state is explored and shows the expected properties for a superconducting transition, confirming that the downturn is caused by the onset of superconductivity.

Figure 5.17c shows the low temperature resistivity with different applied magnetic field, where the field is applied in-plane and parallel to the long side of the sample to minimise the demagnetising shape factor, showing the rising residual resistivity with field from the normal state MR and the apparent removal of the resistance downturn.

Figure 5.17d more clearly shows the removal of the downturn by offsetting the curves in resistivity for the normal state MR. There is a clear shift of the downturn to lower temperatures with increasing field as expected for the superconducting state, and by 8 T the downturn is completely shifted to below the lowest temperature reachable. Figure 5.17e shows the dependence of T_c on the applied field, more clearly showing the reduction of T_c. An initial estimate of the critical field at 0 K is found by the extrapolation of a linear trend to $T_c = 0$, or the complete destruction of the SC state,

leading to $B_c \approx 9$ T.

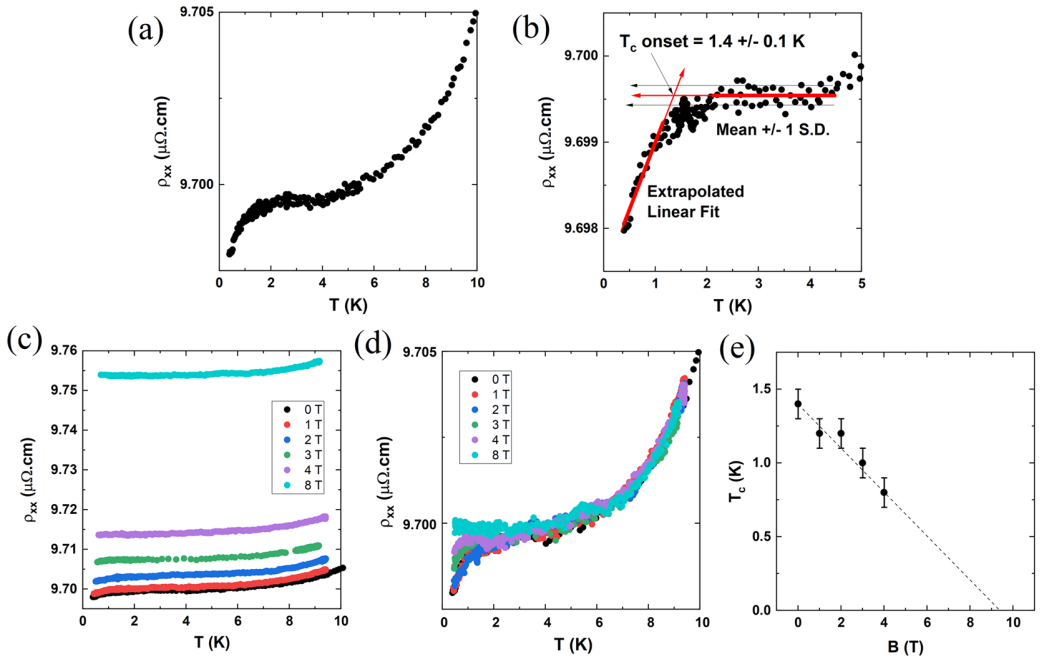

Figure 5.17: (a) Low temperature resistance downturn in $RhPb_2$ film. (b) Details regarding the determination of the onset temperature, finding $T_c = 1.4 \pm 0.1$ K. (c) Resistivity temperature dependence measured with different applied fields applied in-plane and parallel to the current and longest side of the sample, showing the normal state MR and removal of the resistance downturn. (d) Field dependence of the transition (curves offset in resistivity to match at 9 K) clearly shifting the transition onset to lower temperatures with applied field. (e) Clearer dependence of onset temperature with applied field, linear extrapolation gives an initial estimate for the critical field close to 9 T.

Figure 5.18a shows the in-plane MR with field applied parallel to current taken at 380mK, showing no clear transition from the SC state to the normal state and MR proportional to B^2 shown by the red line. Since the samples do not show a full transition to zero resistance and there is no large transition to see in the MR

it is difficult to directly extract any critical field values from Figure 5.18a. To better visualise the contribution of the SC state to the MR the field dependence of the quantity $\Delta\rho_{0.5\mathrm{K}-1.5\mathrm{K}} = \rho_{0.5\mathrm{K}} - \rho_{1.5\mathrm{K}}$ is extracted from the ρ_{xx} vs T curves and plotted in Figure 5.18b, where some details are shown regarding the extraction of critical field values used later.

Figure 5.18c shows the field dependence of the SC transition extracted from different temperature points of the field dependent resistivity data, following the same protocol with $\Delta\rho_{TK-1.5K} = \rho_{TK} - \rho_{1.5K}$, where T is given in the legend. Overall, there is a leftward shift of the transition with increasing temperature, corresponding to lowered critical field values, as expected for the superconducting state. Since this data is extracted from within the resistivity transition in temperature, the total size of the transition is also reduced with increasing temperature.

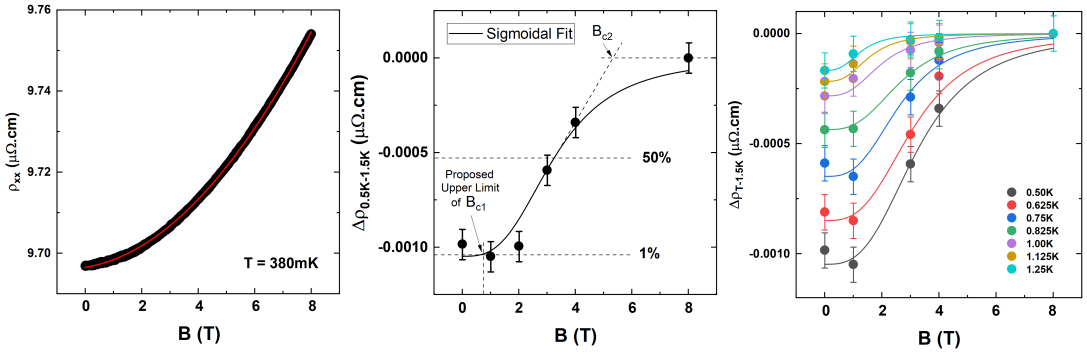

(a) (b) (c)

Figure 5.18: (a) Field dependence of the resistivity showing no clear transition from the SC state. Field is applied parallel to current direction and parallel to the longer side of the sample to minimise shape demagnetisation effects. (b) Field dependence of the superconducting transition extracted from the resistivity vs. temperature data taken at different applied field. Transition is modelled as a sigmoidal function for extraction of the upper critical field values, by extrapolating the tangent at the halfway point to $\Delta\rho = 0$, and for an estimate of an upper limit for the lower critical field B_{c1-UL} by the field value at which a 1% change in resistivity is found. (c) Temperature dependence of the SC transition in field.

Given the field dependence of the resistance downturn it appears that the thin-film

$RhPb_2$ is Type-II and exists in a mixed state before the complete destruction of the superconductivity. The transition persists across a wide field range after the initial suppression of SC, rather than a swift destruction in a narrow field range as would be the case for a Type-I superconductor in the parallel field configuration. The current density during measurement is $\sim 10^2$ A/cm^2 meaning transition broadening effects are negligible [238].

Intriguingly, $PdPb_2$ displays Type-I superconductivity in single-crystals with the BCS values of $\xi_0 = \frac{0.18\hbar v_F}{kT_c} = 200$ nm, $\lambda_L = \left(\frac{\epsilon_0 m^* c^2}{n_s e^2}\right)^{1/2} = 50$ nm [201]. With $l = 64$ nm those samples are moderately dirty, and $\kappa = 0.715\frac{\lambda_L}{l} = 0.55$, close to the threshold of Type-II behaviour. For $RhPb_2$ the BCS values are estimated as: $\xi_0 = 1000$ nm, and $\lambda_L = 20$ nm for $m^* \approx 1.9m_0$ estimated later, meaning it should also likely show Type-I superconductivity which is at odds with the observed behaviour.

To gather more information regarding the nature of the superconductivity some established methods for extracting the upper critical field values are employed [238]. The transition is modelled as a sigmoidal function and the slope at the halfway point of the transition is extrapolated to the intersection of the $\Delta\rho = 0$ line, shown by the dotted lines in Figure 5.18b, to extract the value of B_{c2}. The temperature dependence of these values are shown in Figure 5.19a. Uncertainties in the critical field values are calculated from the fitting parameters for the sigmoidal function.

Following a linear extrapolation of $B_{c2}(T)$ the maximum value at 0 K is estimated to be 8.9 T, allowing estimation of the effective coherence length ξ via: $B_{c2}^{\parallel} = \frac{\Phi_0}{2\pi\xi^2}$ [80], which gives $\xi = 6.1$ nm. Since $\xi \simeq l = 5$ nm determined from the normal state transport, the films are in the dirty limit of superconductivity where: $\frac{1}{\xi} = \frac{1}{\xi_0} + \frac{1}{l}$, and $\xi \approx l$ if $l \ll \xi_0$. Since the penetration depth is also increased in the dirty limit [80], it seems that the short mean-free paths in these films are responsible for the Type-II magnetic behaviour.

To reinforce this, it is desirable to estimate a lower bound for the effective GL parameter $\kappa = \frac{\lambda}{\xi}$ for the films by estimating a value of the effective penetration depth λ from the experimentally determined value of B_{c1}. Since in the Ginzburg-Landau theory: $B_{c1} \approx \frac{\Phi_0}{4\pi\lambda^2} \ln \lambda/\xi$ it is possible to solve numerically for λ given a value of ξ and B_{c1} [80]. Typically, accurate determination of B_{c1} comes from magnetisation measurements since the resolution in typical SQUID-VSM apparatus is fine enough to resolve the initial flux penetration that defines B_{c1} [80, 96, 98].

Since T_c is below temperatures reachable in the University of Leeds' SQUID-VSM, the field value at which the resistivity increases by 1% from the baseline value of the sigmoidal function in Figure 5.18c is instead used. Rather than the initial flux penetration this point will correspond to 1% of the superconducting downturn in resistance being replaced by a resistive voltage caused by the motion of flux vortices from the Lorentz force [80]. This means it is a result of the existence of flux vortices in the material, thereby guaranteeing some flux penetration, but does not represent the true B_{c1} value.

We note that the onset field of the resistive transition is also affected by vortex pinning, whose strength here is assumed to stay constant in the temperature range $0.380 < T < 1.25$ K. This means the 1% resistive change is taken as a consistent limit representing the same critical flux density where the pinning forces are overcome and the resistive transition begins. Accordingly, a lower B_{c1} value then gives a lower value of field where this critical flux density is reached, since each flux line contributes the same extra Φ_0 to the total flux density. This scheme is introduced to provide an extreme upper bound for the value of B_{c1}, labelled B_{c1-UL} since the two values are proposed to be correlated for constant pinning, which then provides a lower bound for λ and correspondingly κ.

The extracted values of B_{c1-UL} are plotted in Figure 5.19b. To estimate the value of $B_{c1-UL}(0)$, the data is fitted to the empirical temperature dependence: $B_{c1}(T) = B_{c1}(0)\left[1-(T/T_c)^4\right]$, based on the empirical temperature dependence of λ from the Gorter-Casimir two-fluid model [80, 96, 98]. We note that the detailed temperature dependence of λ and therefore B_{c1} will depend on the exact details of the superconducting pair-potential, however, as is confirmed in the next section, strong evidence is found for conventional superconducting behaviour meaning the application of this model is valid.

The value at 0 K is found to be 0.84 ± 0.03 T. From this the lower limit for λ is estimated to be ≈ 13 nm, meaning the lower limit for $\kappa \approx 2.1$, and that the films have been experimentally confirmed to be above the threshold for Type-II behaviour.

To reiterate, measurement of the films magnetisation would lead to accurate determination of B_{c1} and generally confirm the nature of the superconductivity by confirming the shape of the magnetic transition in field. Further, and crucially, the value of λ estimated is an extreme lower limit based on an empirical consideration of the experi-

mental data: in reality lower values of the true B_{c1} are expected instead of B_{c1-UL}, and the actual penetration depth will be larger. According to the dirty limit GL theory: $\lambda(T) = \lambda_L(T)\left(1 + \frac{\xi_0}{l}\right)$ [80], and the penetration depth could easily reach $\sim$ 300 nm given the extremely dirty nature of these films, meaning the true value may instead be limited by the thickness of the film and lead to considerable anisotropy of the upper critical field values for in-plane and out-of-plane field [239].

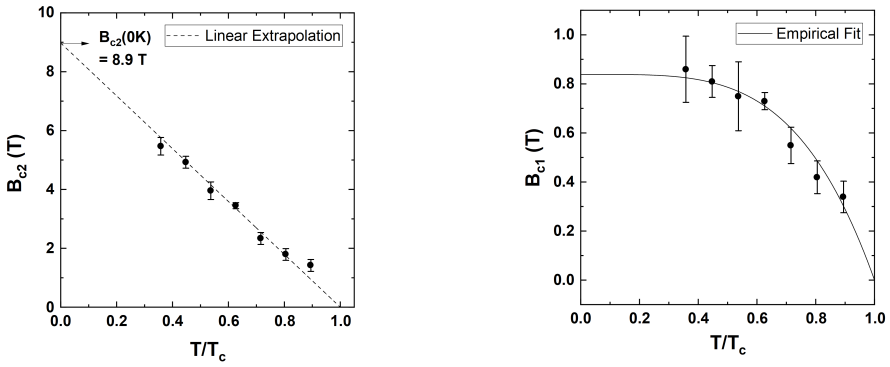

(a) (b)

Figure 5.19: (a) Temperature dependence of the upper critical field values and linear extrapolation for an estimate of the value of $B_{c2}(0)$. (b) Temperature dependence of the upper limit B_{c1} values defined using the resistive transition, which follow the expected temperature dependence from the 2-fluid model, allowing estimation of $B_{c1}(0)$ and $\lambda(0)$.

5.4.2 Evidence for Conventional Superconductivity from the Temperature Dependence of the Upper Critical Field

The temperature dependence of the upper critical field values provides a testing ground for unconventional behaviour in superconducting materials. Typically, unconventional pairing symmetries are implied based on deviation from the usual Ginzburg-Landau theory for *s*-wave Cooper pairs, or by deviation from the extended theory of Werthamer, Helfand and Hohenberg (WHH) that takes into account the effects of orbital de-pairing, spin-paramagnetism, and the spin-orbit interaction on the upper critical field value [99–101]. Notably, spin-triplet pairings with aligned-spin states are found to be more robust against spin-paramagnetism pair breaking effects, where B_{c2} values above the upper limit defined by the WHH formalism are taken as an indication of spin-triplet pairs

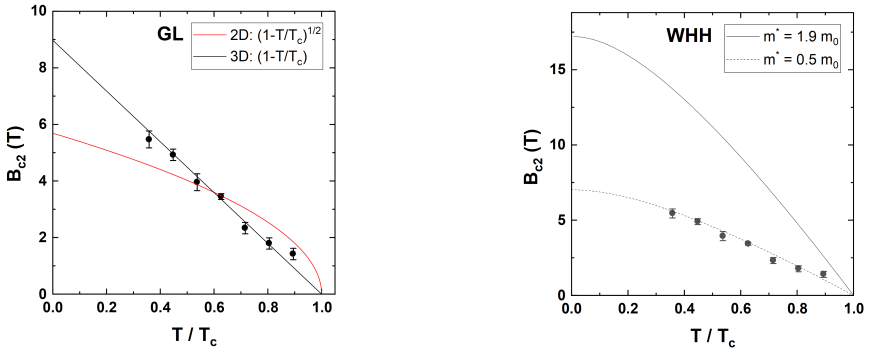

(a) (b)

Figure 5.20: Temperature dependence of B_{c2} with (a) fitting to the 3D and 2D forms of the GL upper critical field dependence on temperature, and (b) upper WHH theory limit for conventional behaviour calculated using the estimated effective mass $m^* \approx 1.9m_0$. Dashed line shows minimum limit of the effective mass able to be explained by conventional behaviour.

and unconventional superconductivity.

First, in the previous section a linear extrapolation of the experimental values of was used to extract the value of $B_{c2}^{\parallel}(0)$, which was essentially found to fit the data well. This linear trend is consistent with the 3D form ($d \gg \xi$) of the Ginzburg-Landau theory for a conventional BCS superconductor:

$$B_{c2}^{\parallel}(T) = \frac{\Phi_0}{2\pi\xi^2}\left(1 - \frac{T}{T_c}\right) \tag{5.4}$$

In the 2D limit of superconductivity ($d < \xi$) a modification to the GL theory is required:

$$B_{c2}^{\parallel}(T) = \frac{\Phi_0}{2\pi\xi d/\sqrt{12}}\left(1 - \frac{T}{T_c}\right)^{1/2} \tag{5.5}$$

and for completeness the fits to both of these forms is shown in Figure 5.20a. Since the mean-free path l is much shorter than the expected coherence length ξ_0, the films are in the dirty limit of superconductivity ensuring that $d \gg \xi$, as confirmed by the clear linear dependence in Figure 5.20a. The full 3D GL fit finds $\xi = 6.1 \pm 0.1$ nm.

In order to properly consider the WHH pair breaking effects, knowledge of the effective mass is required as it appears in the reduced magnetic field term that is solved for numerically for a fixed temperature. Without the ability to directly measure the

effective mass it is estimated from the density of states at the Fermi level, following a reversed calculation applied to $PdPb_2$ [201]. Measurement of the specific heat capacity and subsequent fitting to the conventional Debye formula in $PdPb_2$ yielded a value for the Sommerfield Coefficient γ of 128 J m^{-3} K^{-2}, which was then used to estimate the effective mass according to: $m^* = \frac{3\hbar^2\gamma}{k_B^2 k_F}$, giving $m^* = 2.6m_0$. The Sommerfield coefficient is directly related to the density of states at the Fermi level N_0 by: $\gamma = N_0\frac{\pi^2 k_B^2}{3}$, giving $N_0 = 2.2$ states eV^{-1} unit cell^{-1} [201] in good agreement with the band structure calculations in Figure 5.2b.

Given this agreement and that the band structure for $RhPb_2$ is available, this process is used in reverse to estimate the effective mass: extracting $N_0 = 4$ states eV^{-1} unit cell^{-1} at the predicted Fermi energy, gives $\gamma \approx 170$ J m^{-3} K^{-2}, leading to $m^* \approx 1.9m_0$ for $p = 1.5 \times 10^{23}$ cm^{-3}. Using the WHH theory with this value of m^* gives the curve shown in Figure 5.20b, where the measured values of B_{c2} are clearly far below the limit for conventional s-wave behaviour. The lower limit for conventional behaviour in the WHH theory is determined from a fit to the observed data to be $m^* \approx 0.5m_0$.

The fact that the observed values of B_{c2} are far below the upper limit of the WHH theory implies a strong spin-paramagnetic effect in $RhPb_2$, bolstering the conclusion of spin-singlet pairings. The upper limit for B_{c2} based on the orbital de-pairing and spin-paramagnetic effect is calculated as 2.4 T [240], suggesting a significant recovery of the B_{c2} values due to the strong spin-orbit interaction in the material. We note that the extrapolation of the WHH curve that follows the data gives $\xi_{\mathrm{WHH}} = 6.9$ nm, in reasonable agreement with the GL theory, and also supporting the determination of dirty behaviour.

5.4.3 Other Elements of the Film

To reinforce that the observed downturn in resistivity is arising from $RhPb_2$ it is worth considering the other elements of the film structure. Rh is a Type-I superconductor with an extremely low T_c and B_c in bulk samples of 325 μK and 49 mG respectively [241], so is unlikely to show SC with the T_c observed in thin film form according to Ref. [217]. Ta is a type-I superconductor with bulk T_c and B_c of 4.48 K and 0.09 T respectively [242] [243], however displays a significant suppression of T_c to 500 mK for 50Å thickness, and a slight enhancement of B_c to 0.1 T [223]. The T_c and B_c values

measured in the $RhPb_2$ films are much higher than the expected values for either Ta or Rh at the thickness' grown, so it is unlikely that the onset of SC arises from these layers.

Since the film is slightly Pb-rich, there is likely some residual un-reacted Pb present in the film. A composition of $RhPb_{2.65}$ leads to ≈ 5 Å of Pb remaining for each repeated unit assuming complete reaction of the Rh to form $RhPb_2$. Pb shows bulk-like SC with $T_c \approx 4.3$ K in two atomic layers [244], and substrate induced SC in single atomic layer samples with $T_c \approx 1.7$ K [221], which both rely on pristine ordering of the Pb film. It is unlikely that such high quality ordering of the residual Pb is taking place in the films, especially given the approximate roughness of the interfaces is typically the order of 5 Å.

To reinforce these ideas, a non-annealed film shows no SC down to 380mK in Figure 5.21a, confirming that the individual Ta and Rh layers do not show SC and that the individual Pb layers do not show SC with their maximum thickness before annealing, so the transition is likely not caused by any residual Pb in the samples. Instead, a slight upturn in the resistance is observed at low temperature that is not removed with field, therefore not arising from the Kondo effect due to ferromagnetic impurities [245, 246].

As shown in the previous section films after a short annealing period form an initial Rh_4Pb_5 phase. Figure 5.21b shows the low temperature dependence of the resistivity for one of these films, clearly showing no SC transition down to 380mK. The initial phase shows a similar upturn to the non-annealed films.

5.5 Effect of Annealing Temperature

Since the films show behaviour consistent with the dirty limit of superconductivity, further investigation into the effect of annealing temperature was carried out in attempts to reduce disorder and produce cleaner $RhPb_2$ thin films that may show more intrinsic Type-I superconductivity. Since disorder generally leads to transition broadening effects, it was also anticipated that hotter annealing temperatures should lead to an increase in the observable superconducting fraction of the film by improving the transition sharpness [247].

One further consideration was that a linear extrapolation of the transition onset suggests that the maximum change in resistivity expected is roughly 0.05% by 0 K, which suggests that in a majority of the film there is $RhPb_2$ where the superconductiv-

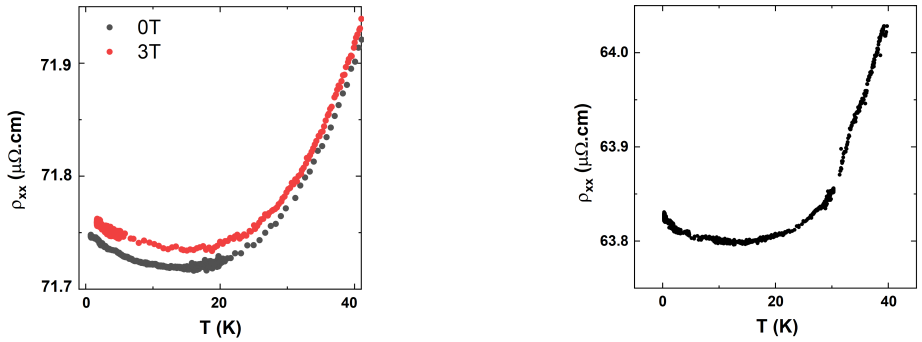

(a) (b)

Figure 5.21: Low temperature transport of control samples with no $RhPb_2$ phase present. No superconductivity is observed down to 380mK in (a) non-annealed films, confirming that the Ta/Rh buffer, Rh cap, and residual Pb are not responsible for the SC, or (b) films after the initial mixing of Pb-Rh-Pb layers that likely form Rh_4Pb_5.

ity is suppressed. Notably, the amount of crystalline $RhPb_2$ seems limited based on the XRD peak area compared to the area of the initial crystalline Rh_4Pb_5 phase, and may suggest significant regions of amorphous $RhPb_2$ or Rh_4Pb_5 where re-crystallisation is unable to complete at a given temperature. Increased annealing temperature rather than time was chosen, since crystallographic diffusion processes usually scale exponentially with temperature [125].

Overall, higher annealing temperatures were found to reduce T_c, making any improvements in the sharpness of the superconducting transition difficult to identify. Structural and electronic characterisation show a reduction of disorder in the films, but the total phase strength remains highest for an annealing temperature of 450°C. The sample discussed in detail so far showed the largest drop in resistivity by 380 mK, hence the detailed consideration in the previous sections.

Since there is evidence for conventional behaviour based on the critical field measurements, evidence for a conventional, dominant electron-phonon scattering mechanism in the films, and disorder is not found to reduce T_c, pointing away from spin-triplet pairing, the changes of T_c are examined within the BCS-Eliashberg framework for conventional phonon-mediated superconductivity, where they are consistent with a reduction of the electron-phonon coupling strength.

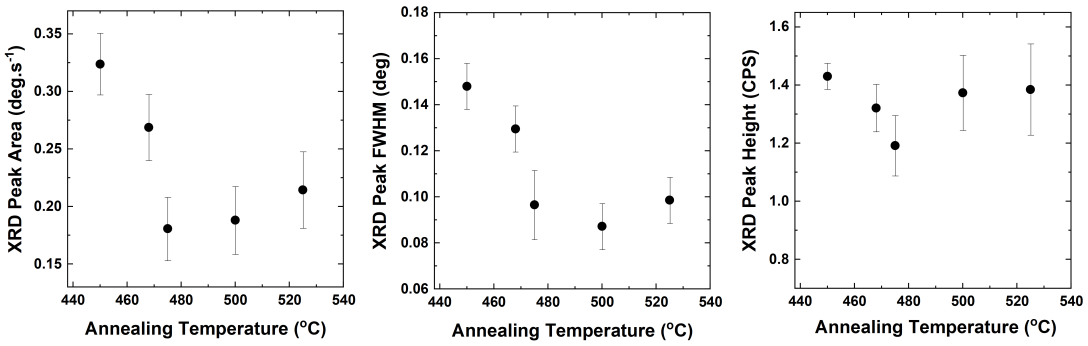

(a) (b) (c)

Figure 5.22: Annealing temperature dependence of the structural parameters of the films determined by XRD. Showing: (a) peak area, (b) peak height, and (c) peak FWHM for the (202) orientation peak of $RhPb_2$.

5.5.1 Structural Changes

A group of films with the composition $RhPb_{2.65}$ were annealed in Ar purged and evacuated quartz tubes for 24 hours at temperatures from 450°C to 600°C: only temperatures in the range 450 to 525°C gave the $RhPb_2$ (2 0 2) textured phase. Above 550°C another recrystallisation of the film was observed where the $RhPb_2$ reacts with the Rh cap and buffer layer to re-form an Rh_4Pb_5 phase in a different orientation.

Figure 5.22 shows the progression of the (202) orientation $RhPb_2$ XRD peak parameters, extracted using Lorentz peak fits, with changing annealing temperature in the range 450 - 525°C. The temperature giving the maximum XRD peak area is found to be 450°C. Higher annealing temperatures lead to narrower XRD peaks, which reflect larger grain sizes and reduced structural disorder. The height of the XRD peaks stays roughly constant for all annealing temperatures.

5.5.2 Normal State Transport

Figure 5.23 summarises the dependence of normal state transport properties on annealing temperature, overall confirming a reduction of disorder with higher annealing temperatures which lead to a reduction of the residual resistivity and increases in the RRR in Figure 5.23d.

Positive correlations of carrier density and perpendicular MR% with annealing tem-

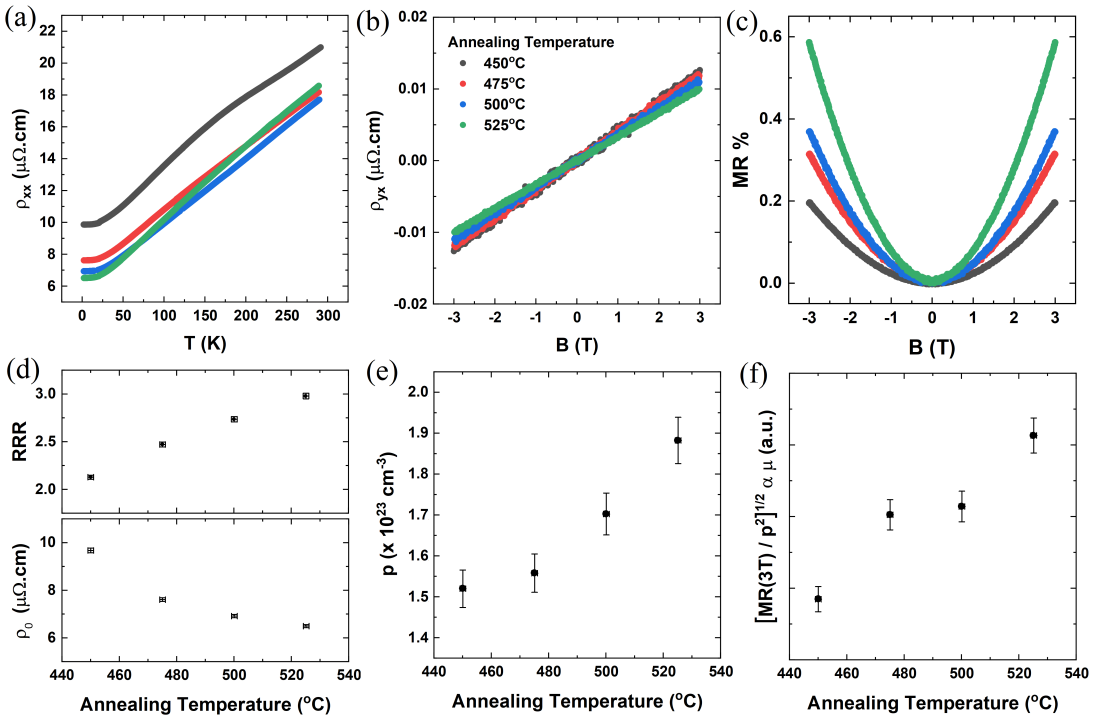

Figure 5.23: Summary of the changing normal state transport properties of the films with changing annealing temperature. Showing: (a) resistivity dependence on temperature, (b) Hall resistivity, (c) perpendicular MR, (d) ρ_0 and the RRR, (e) Hall carrier density and (f) term extracted from the MR $\propto \mu$.

perature are also found. The increase in the MR is related to an increased conductivity with higher annealing temperatures since MR $\propto (\sigma B)^2$ in a single band model [134]. With higher annealing temperatures the mobility also increases due to fewer defects and scattering sites: Figure 5.23f plots the term $\left(\frac{\mathrm{MR\%(3T)}}{p^2}\right)^{1/2} \propto \mu$ showing an overall positive correlation with annealing temperature.

5.5.3 Tuning Critical Temperature

Figure 5.24 shows the low temperature resistivity for each sample, with the annealing temperature labelling each plot, finding that as the annealing temperature is increased

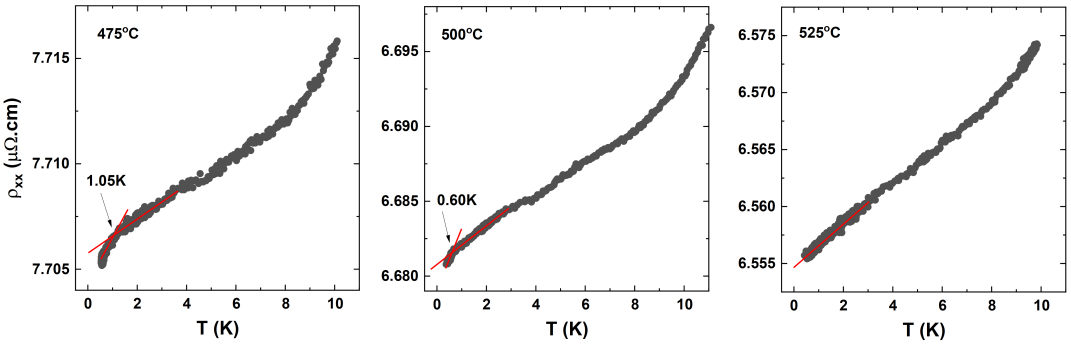

(a) (b) (c)

Figure 5.24: Low temperature resistivity for $RhPb_2$ films annealed at different temperatures: (a) 475°C, (b) 500°C, and (c) 525°C, showing that T_c is reduced with higher annealing temperature. Red lines are a guide to the eye to make the onset of superconductivity more obvious.

from 450°C the downturn in resistance arising from the SC is shifted to lower temperature until it disappears completely in the sample annealed at 525°C. Again T_c refers to the superconducting onset temperature, determined by the intersection of the residual resistivity and the slope of the transition. The reduction of T_c is accompanied by the emergence of broad downturn that starts near to 9K, whose magnitude increases with annealing temperature.

Figure 5.25a summarises the dependence of T_c on annealing temperature. The remaining plots in Figure 5.25 show T_c plotted against the $RhPb_2$ (202) XRD peak FWHM, the residual resistivity ρ_0, and finally the RRR, which all show a positive correlation of T_c with structural disorder.

Typically, unconventional spin-triplet superconductors see a suppression of T_c with increasing levels of disorder [92]. Whilst more robust against non-magnetic disorder on account of the non-trivial spin-momentum locking and topological properties, the unconventional spin-triplet pairings present in TSCs are also expected to show suppressed T_c in the presence of disorder [86, 87].

Importantly then, the *enhancement* of T_c with increasing disorder observed here suggests some convolution of effects: a conventional s-wave pairing in $RhPb_2$, given the upper critical field analysis earlier, which are firmly established to be insensitive to disorder [86, 248, 249], leaving T_c unchanged; and a fundamental modification to the

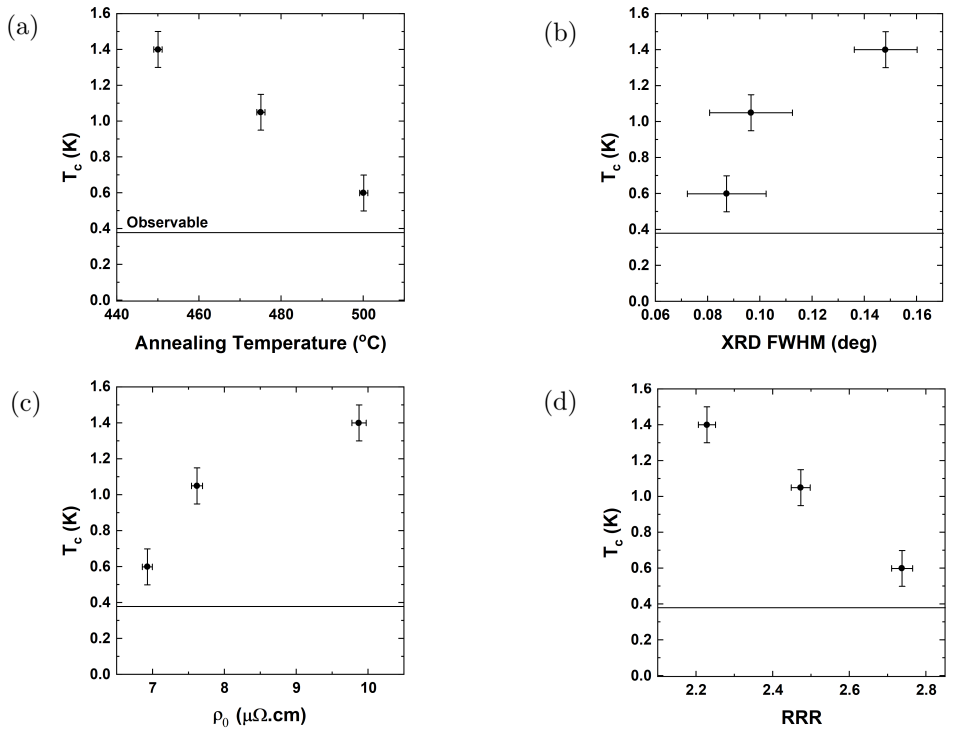

Figure 5.25: The dependence of T_c on material parameters related to the amount of disorder in the thin-films: (a) annealing temperature, (b) $RhPb_2$ (202) XRD peak FWHM, (c) residual resistivity, (d) RRR. All measures suggest a higher T_c for higher disorder levels.

underlying material properties that cause the changes of T_c.

Given the consideration of the resistivity dependence on temperature, the dominant scattering mechanism seems to be electron-phonon, taken with the signatures of conventional s-wave behaviour found so far, the Migdal-Eliashberg theory for electron-phonon mediated superconductivity can be applied to the system, which is an extension of the BCS theory accounting specifically for an attractive interaction mediated by phonons [250].

Specifically, this theory has been used to formulate the McMillan equation describing T_c [251]:

$$T_c = \frac{\Theta_D}{1.45} \exp\left\{ -\frac{1.04\,(1+\lambda_{McM})}{\lambda_{McM} - \mu^*\,(1+0.62\lambda_{McM})} \right\} \tag{5.6}$$

with Debye temperature Θ_D, electron-phonon coupling constant λ_{McM}, and renormalized Coulomb potential μ^*. Usually $0.10 < \mu^* < 0.15$, but is difficult to estimate without first principle calculations and is usually taken as a fixed value for a material system. This means that T_c should scale linearly with Θ_D and approximately exponentially with λ_{McM} for $0.2 < \lambda_{McM} < 0.5$, then linearly for $0.5 < \lambda_{McM} < 1$.

First, the values of $T_c = 1.4$ K and $\Theta_D = 140$ K found for the sample annealed at 450°C can be used to estimate a value of the electron-phonon coupling strength λ_{McM} in equation 5.6, giving $\lambda_{McM} = 0.55 \pm 0.05$. This defines $RhPb_2$ as a moderately-coupled superconductor which matches the behaviour of $PdPb_2$ with a similar value of $\lambda_{McM} = 0.67 \pm 0.08$ [201].

As explored earlier, the electron-phonon coupling constant λ_{BG} appears in the Bloch-Gruneisen formula and so can be extracted from the resistivity dependence on temperature, where the values of λ_{McM} and λ_{BG} should in principle agree [233]. The ability to extract an accurate value of λ_{BG} is dependent on knowledge of the Drude plasma frequency ω_p which is formally a tensor quantity related to the inverse effective mass tensor and is calculated theoretically for particular band structures [233]. To quantitatively estimate λ_{BG} a free-electron value of $\omega_p = \left(\frac{pe^2}{\epsilon_0 m^*}\right)^{1/2}$ with $m^* = 1.9m_0$ estimated earlier is assumed here [47].

Figure 5.26 summarises the annealing temperature dependence of the BG parameters for the samples showing a SC transition above 380mK, extracted from fitting to the resistivity curves for $T \leq 25$ K. We find that the Debye temperature stays approximately constant within the uncertainty, but there are systematic reductions in both the temperature exponent n, and the electron-phonon coupling strength λ_{BG}.

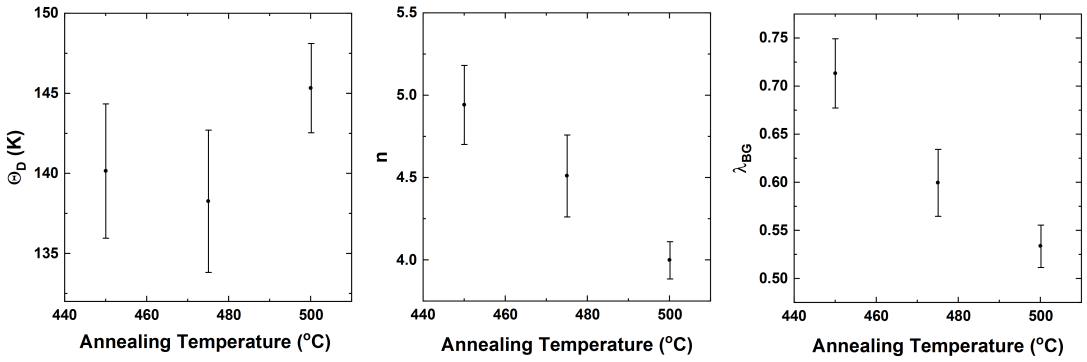

(a) (b) (c)

Figure 5.26: Summary of parameters extracted from Bloch-Gruneisen fitting of the resistivity dependence on temperature, for the samples annealed at different temperatures. (a) Debye Temperature, (b) exponent of the temperature, and (c) the electron-phonon coupling parameter.

The reduction of n likely reflects an increasing dominance of *s-d* scattering to lower temperatures.

The value of λ_{BG} estimated for the sample annealed at 450°C is slightly higher than λ_{McM}, but is in reasonable agreement given the rough estimate for the effective mass. This over estimation of λ_{BG} (and so T_c via equation 5.6) is likely related to the free-electron model estimate of ω_p and further theoretical work in the $RhPb_2$ system is required to properly account for this.

Notably, there is a systematic reduction in the electron-phonon coupling strength with annealing temperature, which is consistent with the reductions of T_c. Quantitatively, the values of T_c predicted using these values of λ_{BG} are over-estimates as mentioned, giving predicted T_c double the observed values. Notably, however, the predicted *changes* of T_c using the McMillan equation are consistent with those observed: a 50% change in T_c is observed between the sample annealed at 450 and 500°C, and 30% between 450 and 475°C, then from the values of Θ_D and λ_{BG} there are 60% and 40% changes predicted respectively using the McMillan equation. In other words, the functional dependence of T_c expected from the McMillan equation for $\lambda_{McM} > 0.5$ is obeyed, strongly suggesting a conventional electron-phonon coupling mechanism.

Specifically, we have: $\lambda_{McM} = \frac{N_0(E_F)\langle g^2\rangle}{M\langle\omega^2\rangle}$ [251], with $N_0(E_F)$ the electronic density of states at the Fermi level, $\langle g^2\rangle$ is the average squared electron-phonon matrix element

(indicative of the energy scale of electron-phonon interaction [251]), M is the atomic mass, and $\langle\omega^2\rangle$ is the squared average phonon frequency.

From the data available here, the p-type carrier density is found to increase slightly with annealing temperature, and the predicted Fermi level position for $RhPb_2$ is close to a sharp peak in the DoS from Figure 5.2a. With an increase in the p-type carrier density the DoS at the Fermi energy would decrease, leading to a reduction in the value of λ_{McM} consistent with the observations. However, it is difficult to say exactly why λ_{McM} is changing with annealing temperature, since the effects of changes in $N_0(E_F)$, $\langle g^2\rangle$ and $\langle\omega^2\rangle$ cannot be separated at present.

Overall, the fact that disorder seems to not suppress the superconducting phase observed in these $RhPb_2$ thin-films suggests a conventional superconducting pairing. Assuming an electron-phonon interaction, in line with the indications of conventional superconductivity observed so far, the changing values of T_c are consistent with changes in the electron-phonon coupling parameter. At present, it is unclear why this parameter is changing, however the slight changes in carrier density observed with increasing annealing temperature may lead to a reduction in the density of states at the chemical potential.

5.6 Effect of Annealing Environment

To characterise whether partial oxidisation during annealing affects the superconducting properties of the film, a $RhPb_{2.65}$ sample was annealed for 24 hours at 450°C in an UHV system with base pressure $\approx 10^{-9}$ mbar that is continually evacuated whilst heating. Partial pressures during annealing were: N, H_2O, $CO_2 \approx 5 \times 10^{-9}$; H $\approx 8\times 10^{-9}$; O $\approx 2\times 10^{-11}$.

First, the structural properties and normal state transport characteristics of the film annealed in UHV are very similar to the sample annealed for 24 hours at 450°C in Ar purged and evacuated quartz tubes, as shown in Figure 5.27. The mean free path l is calculated as before: (5.1 ± 0.1) nm compared to (4.5 ± 0.1) nm for the furnace annealed sample.

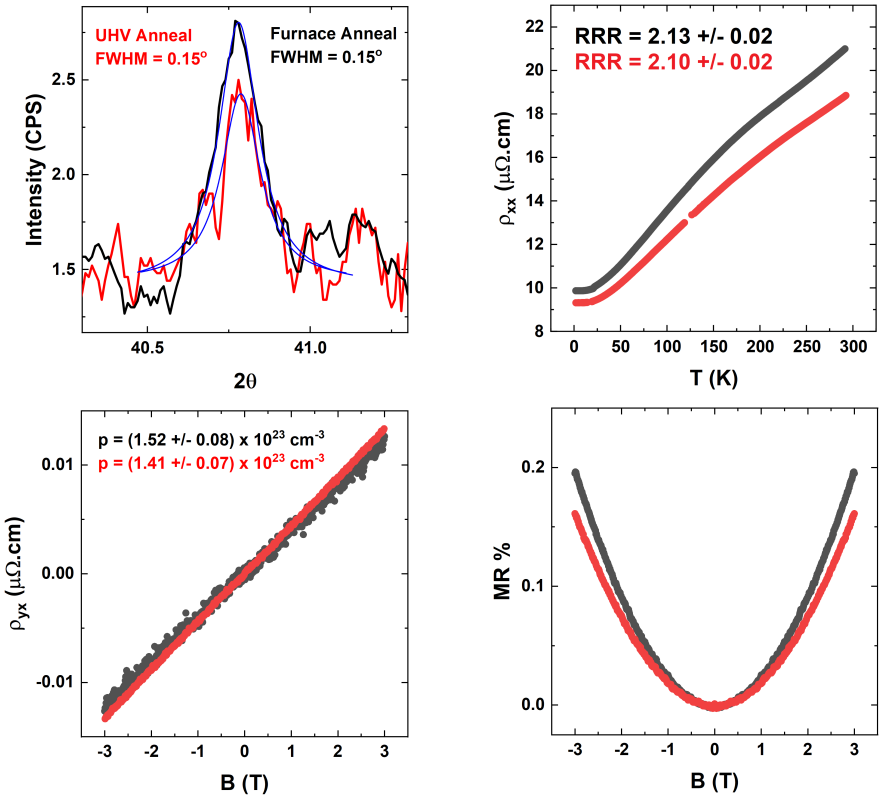

Figure 5.27: Summary of the XRD and normal state transport for a $RhPb_2$ sample annealed in a UHV environment at 450°C for 24 hours.

Figure 5.28a shows the low temperature resistivity: again a clear downturn in resistance is observed with onset temperature 1.3 ± 0.1 K, where T_c is again lowered with field as expected. However, a larger drop in resistivity is observed by 380mK, the percentage change in resistance for the UHV annealed sample is 0.04%, whereas the sample annealed in Ar purged quartz tube has 0.01% decrease.

Figure 5.28b shows the field dependence of the SC transition at different temperatures, with the effective coherence length extracted using the 3D form of the GL equation in Figure 5.28c as $\xi = 5.2 \pm 0.1$ nm, again in agreement with the dirty limit of superconductivity. The superconductivity again more closely follows the 3D form of the Ginzburg-Landau equation, this is confirmed by a lower χ^2 value: 0.35 for 3D curve and 0.39 for 2D curve. The observed values of B_{c2} are also again far below the WHH upper limit for *s*-wave superconductivity found earlier.

The values of B_{c1} following the same extraction method as before follow the expected 2-fluid temperature dependence, finding $B_{c1}(0)$ to be 1.13 ± 0.07 T, leading to a minimum value of the penetration depth $\lambda \approx 9$ nm. The lower limit for κ is then estimated as 1.7, confirming that the dirty $RhPb_2$ films reproducibly show Type-II behaviour.

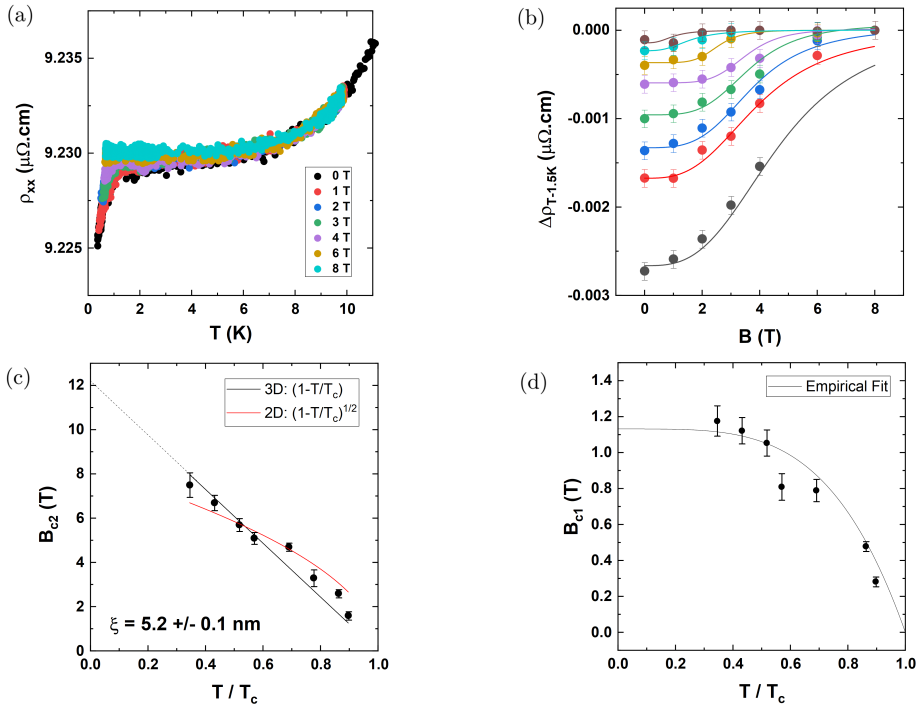

Figure 5.28: Summary of the superconducting properties of $RhPb_2$ film annealed in a UHV environment. (a) A larger drop in resistance is observed relative to samples annealed in Ar purged quartz tubes, (b-d) magnetic properties show similar behaviour to furnace annealed samples with Type-II behaviour.

This sharper superconducting transition arises from a greater volume of material becoming superconducting for the same reduction of temperature. Broadly speaking this means that there is some oxide forming during annealing that replaces or suppresses some amount of the superconducting $RhPb_2$ in the film, and that overall the samples are a mix of superconducting clusters embedded in a matrix of non-superconducting material. Even with the sharper transition, only a total drop in resistance of 0.13%

is expected based on a linear interpolation of the downturn to 0K, signifying that still only a small portion of the $RhPb_2$ has become superconducting.

There is no distinct change in T_c with the annealing environment as there is with annealing temperature, which suggests negligible effects due to increased oxidisation from higher annealing temperature on the changes of T_c found previously. Electron microscopy and chemical analysis of the films grown would be useful in quantifying the amount of oxide forming and it's distribution within these films.

5.7 Summary of Superconducting Parameters

For reference, Table 5.4 summarises the film parameters, annealing conditions, normal state transport, and superconducting parameters for the $RhPb_2$ film discussed in the most detail in this thesis.

5.8 Discussion

First from a materials optimisation perspective, only the onset of superconductivity is observed by a partial reduction of the resistivity in these thin-film $RhPb_2$ samples, and lower temperatures are required to see whether a full transition to zero resistance is present. Extrapolation of the measured downturns seems to suggest not, meaning only small volumes of the film are becoming superconducting. No impurity phases are observed in the XRD of the films, however the increases in the sharpness of the transition found whilst annealing in a UHV environment suggest that some oxide is forming and suppressing portions of the superconducting $RhPb_2$.

Rather limited composition and annealing temperature ranges are found to optimise the phase strength of the thin film $RhPb_2$ system grown in this work. In a separate investigation, using thicker initial layers in the multilayer film to be annealed, no $RhPb_2$ was found to form, and instead Rh_4Pb_5 reproducibly formed after re-crystallisation. This suggests that better initial mixing conditions promote the formation of $RhPb_2$. From this, it is expected that co-deposition in a UHV environment with the capability to anneal in-situ or grow on a hot substrate may provide a stronger $RhPb_2$ phase with less oxidation, ultimately showing thin-films with a larger fraction of superconducting material.

Overall, further work is required to produce cleaner thin-films of $RhPb_2$ that show

Nominal Composition	$RhPb_{2.65}$
Orientation	(202)
Annealing Pressure	$\sim 10^{-2}$ mbar
Annealing Temperature	450 ± 1 °C
Annealing Time	24 hours
Thickness	109.9 ± 0.6 nm
ρ_0	9.69 ± 0.02 $\mu\Omega$.cm
RRR	2.13 ± 0.01
p	1.52 ± 0.05 $\times 10^{23}$ cm^{-3}
μ	4.1 ± 0.1 cm^2/Vs
l	4.5 ± 0.1 nm
m^* [Estimated]	1.9 m_0
T_c [Onset]	1.4 ± 0.1 K
$\Delta\rho/\rho$ by 380mK	0.01 %
ξ_0 [Estimated]	1000 nm
λ_L [Estimated]	20 nm
B_{c2}(0 K)	8.9 ± 0.1 T
ξ(0 K)	6.1 ± 0.1 nm
B_{c1}(0 K) [Upper Limit]	0.84 ± 0.03 T
λ(0 K) [Lower Limit]	13 nm ± 0.5 nm
κ(0 K) [Lower Limit]	2.1 ± 0.1
Θ_D	140 ± 4 K
λ_{BG}	0.71 ± 0.04
λ_{McM}	0.55 ± 0.05

Table 5.4: Summary of the $RhPb_2$ superconducting thin-film's parameters measured and estimated in this work.

a full transition to the superconducting state at easily accessible temperatures. On the other hand, the successful single-crystal growth reported by Mochiku et. al [41] suggests that reactions with quartz crucibles can be avoided by using powdered Rh to initially pre-react with Pb, which may ultimately yield clean-superconducting single crystal samples of $RhPb_2$. If crucible contamination remains an issue, floating zone furnace methods provide an alternative route of synthesis for the TSC candidate $RhPb_2$.

Despite this further work required to produce cleaner samples, the superconductivity that is observed is consistent with the conventional theories for s-wave spin-singlet Cooper pairs where the attractive interaction is mediated by phonons, in overall agreement with the iso-structural material $PdPb_2$ [201]. At present some inconclusiveness in this study exists due to the estimations of the effective mass: experimental verification of $m^* \simeq 1.9m_0$ is therefore important to solidify some of the conclusions presented here.

So far no experimental evidence for the proposed structural polymorph β-$RhPb_2$ has been observed. The XRD peak from the $RhPb_2$ (202) plane remains unchanged with annealing up to 525°C, however the second re-crystallisation into Rh_4Pb_5 observed above 550°C places a limit on the range of investigation for the thin-film structures grown here.

5.9 Further Work

For the work presented in this chapter, it is important to seek experimental verification of some properties in order to solidify some of the arguments presented.

First, the conclusion of conventional behaviour based on the upper critical field analysis relied on an estimated value of the effective mass ($m^* \approx 1.9m_0$), which then allowed calculation of the upper limit of the WHH theory, which the films were far below. A lower limit of the value of the effective mass was proposed based on where the measured critical field values would exceed the WHH limit, which was $m^* \approx 0.5m_0$. This means a 3-4 fold reduction in the effective mass relative to the estimated value is permitted for the conclusions to hold.

This estimation of the effective mass was again taken as a constant within the Bloch-Gruneisen fitting to extract the electron-phonon coupling parameter λ_{BG}, which was found to reduce with annealing temperature and quantitatively account for the changes in T_c between samples. From this, a change in the density of states at the chemical potential was proposed as a possible mechanism for the reduction of λ_{BG} and

so T_c.

To address both the estimated value of m^* and investigate the possibility of a change in the density of states at the chemical potential further, we propose an experiment measuring the temperature dependence of the specific heat capacity for the series of films annealed at different temperatures.

At low temperatures, the total specific heat is modelled using the Debye approximation, which describes the total specific heat as: $c_p(T) = c_{el} + c_{ph} = \gamma_n T + A_3 T^3 + A_5 T^5$, where A_3 and A_5 are coefficients related to the phonon contribution, and $\gamma_n T = N_0 \frac{\pi^2 k_B^2}{3} T$ describes the electronic contribution [47, 96]. After measuring the temperature dependence of c_p the data can be fitted to this equation to extract three parameters.

First and foremost, the effective mass can be estimated given knowledge of γ_n, since $m^* = \frac{3\hbar^2\gamma}{k_B^2 k_F}$ and k_F can be calculated from the measured carrier density [201]. This will provide confirmation of the estimated value and also determine whether any changes are found between samples. This will then confirm the WHH curve and the conclusion of conventional behaviour, and also provide a more reliable value of λ_{BG} by providing a true value of ω_p, though this will still be assumed as a free-electron value. This will then allow confirmation of the trend of λ_{BG} with annealing temperature, to see whether the changes of T_c can still be understood through the MacMillan equation.

As well as this, the co-efficient A_3 can be used to estimate the Debye temperature Θ_D, providing a means of confirming the values determined from the Bloch-Gruneisen fitting [201]. Further, the density of states at the Fermi level can be calculated from γ_n and used to determine if this is the driving factor for the changing value of λ_{BG} [251]. We note that it may still be difficult to measure the specific heat capacity across the superconducting transition since T_c is low, and the transition is small, but if increases of T_c and the total transition are found then specific heat measurements can also be used to further probe for signatures of unconventional superconductivity.

Overall, time constraints and equipment limitations have prevented this investigation, however it is an important and interesting avenue to pursue.

Practically, there exist commercial Physical Property Measurements Systems (PPMS) capable of performing the measurement [96, 252]. The principle of measurement is to apply heat to a sample and sample holder, whilst holding a thermally linked stage at constant temperature: measuring the time-dependence of the temperature of the sample and sample holder when heating and cooling provides the means for calculating

the heat capacity of the sample. Commercial equipment provides many in-built correction algorithms and subtraction methods that are automatically applied to present only the heat capacity of the sample, which would otherwise have to be considered carefully.

Since the thin films of $RhPb_2$ are grown on top of a Si substrate, with the presence of additional Rh and Ta layers, a number of control samples will likely be required in order to isolate the contribution from the $RhPb_2$ film.

5.10 Summary

This chapter presents the successful synthesis of textured, superconducting thin-films of $RhPb_2$, by DC sputtering of repeating multilayer units of Pb-Rh-Pb and using a post growth annealing procedure. Films annealed at 450°C for 5 hours showed a Rh_4Pb_5 phase and no superconductivity, after 24 hours the films re-crystallised and showed XRD peaks in agreement with the (202) orientation of $RhPb_2$, which were confirmed to show the onset of superconducting behaviour at 1.4 K.

The films show transport properties consistent with a single high carrier density band and do not show signatures of the predicted Dirac semi-metal phase. The resistivity dependence on temperature suggests electron-phonon scattering as the dominant scattering mechanism with increasing temperature.

Only the superconducting onset is observed in these films, however consideration of the critical field values confirms that they are below the upper limit defined by the WHH theory, suggesting conventional spin-singlet pairing in the material. The field dependence of the superconductivity shows Type-II behaviour, with an estimated $\xi = 6.1 \pm 0.1$ nm, and $\lambda \approx 13$ nm, giving $\kappa \approx 2.1$ meaning the films are weakly Type-II.

Attempts were made to increase the observable reduction of resistivity from the onset of superconductivity by producing cleaner films, with the ultimate goal of finding a full superconducting transition to zero resistance. First an investigation of the effect of annealing temperature was carried out, where clear trends of reducing disorder were found in the structural and normal state transport properties. This reduction of disorder did not however improve the sharpness of the transition, and instead suppressed T_c, leading to less visible transitions.

Since reductions of disorder should lead to higher critical temperatures for spin-triplet pairings, the changing value of T_c is proposed to occur due to a conventional

superconducting phase in the material with some modification of the underlying properties of the state. Changes in the electron-phonon coupling strength, characterised by Bloch-Gruneisen fitting to the $\rho(T)$ data, are proposed as an explanation for the changes of T_c, based on the MacMillan theory for conventional electron-phonon mediated superconductivity.

A final attempt at increasing the observable superconducting fraction of the film was successful, revealing that UHV environments are beneficial and there may be some oxide formation suppressing the superconducting $RhPb_2$, though no significant quantitative differences in the films properties are observed despite a 4-fold increase in the size of the superconducting transition.

Overall, there still exist some significant barriers to uncovering TSC in a $RhPb_2$ based system: the primary focus for future work in the system should be phase optimisation, where ideally full transitions to zero resistance in clean superconducting films or single-crystals can be found. A future experiment measuring the specific heat capacity of the films grown in this work is proposed as a way of confirming the effective mass required in the WHH theory, and investigating changes in the density of states at the Fermi level as a mechanism for the changing T_c.

Chapter 6

Conclusions

Overall this thesis presents the investigation of two separate materials systems: Sb_2Te_3 and $RhPb_2$. The motivations for studying these materials in particular are based on their attractiveness for future device applications and apparent benefits compared to current materials in the literature.

The key findings in Sb_2Te_3 are: a successful method of controlling the bulk carrier density using excess Te in a modified Bridgman growth, the co-existence of an intrinsic majority hole and impurity minority electron band that govern the semi-classical transport, the emergence of a non-trivial Shubnikov de Haas beating envelope and determination of Dirac-like bulk bands with non-trivial Berry phase, and a confirmation that non-trivial Rashba surface states should be resolved in ~ 50 nm thick samples with $p \geqslant 7.9 \times 10^{19}$ cm^{-3}.

The key findings for $RhPb_2$ are: the successful growth of textured superconducting thin-films, normal state transport consistent with the dominance of a single trivial bulk band, and the determination of conventional superconducting behaviour from the extracted upper critical field values and how T_c is not enhanced with reduced disorder.

The aims of this thesis were to identify, synthesize and optimize topological materials, with the idea to uncover materials systems that present some advantage in terms of applicability. In particular then, the investigation of Sb_2Te_3 provides a clear route of further investigation of device architectures, with confirmation that the Rashba surface states should be accessible in an achievable carrier density range, and confirmation that the Bridgman growth method can effectively control the defect content and therefore chemical potential of single crystals that can be exfoliated to the nano-scale.

We also confirm that superconducting thin films of the TSC candidate $RhPb_2$ can be grown, and uncover some significant sensitivities to the growth and preparation conditions that will be important considerations for any future work in the materials system. Reporting the normal state and superconducting properties here serves as a bench mark for future work given the limited literature so far.

Overall, this work provides context for future studies that should illuminate the non-trivial behaviour in these systems more clearly. As discussed, a key limitation is related to the ability to measure the density of states effective mass in both Sb_2Te_3 and $RhPb_2$, since this would help solidify some estimations of chemical potential positions, and the limits of conventional WHH theory for the superconducting state, respectively.

Future work in these systems should therefore include characterisation of the spe-

cific heat capacity, to place the determined characteristics of these systems on firmer ground, before additional optimisation for device applications through either thickness control in Sb_2Te_3, or further growth optimisation and exploration of the superconducting properties of $RhPb_2$.

Bibliography

[1] A. Kitaev. Periodic table for topological insulators and superconductors. In *2009 AIP Conference Proceedings*, volume **1134**, pages 22 – 30, (2009).

[2] A.P. Schnyder, S. Ryu, A. Furusaki, and A.W.W. Ludwig. Classification of topological insulators and superconductors in three spatial dimensions. *Phys. Rev. B*, **78**: 195125, (2008).

[3] J. C. Y. Teo, L. Fu, and C. L. Kane. Surface states and topological invariants in three-dimensional topological insulators: application to $Bi_{1-x}Sb_x$. *Phys. Rev. B*, **78**: 045426, (2008).

[4] H. Zhang, C.X. Liu, X.L. Qi, X. Dai, Z. Fang, and S.C. Zhang. Topological insulators in Bi_2Se_3, Bi_2Te_3 and Sb_2Te_3 with a single Dirac cone on the surface. *Nat. Phys.*, **5**(6): 438 – 442, 2009.

[5] T.H. Hsieh and L. Fu. Majorana Fermions and Exotic Surface Andreev Bound States in Topological Superconductors: Application to $Cu_xBi_2Se_3$. *Phys. Rev. Lett.*, **108**: 107005, (2012).

[6] F. Wilczek. Majorana returns. *Nat. Phys.*, **5**(9): 614 – 618, (2009).

[7] C.W.J. Beenakker. Search for Majorana fermions in superconductors. *Annu. Rev. Condens. Matter Phys*, **4**: 113 – 136, (2013).

[8] K. L. Wang. Topological insulators: Potential devices and applications. In *2015 IEEE International Magnetics Conference (INTERMAG)*, pages 1–1, 2015.

[9] M.J. Gilbert. Topological electronics. *Commun Phys*, **4**: 70, (2021).

[10] O. Breunig and Y. Ando. Opportunities in topological insulator devices. *Nat Rev Phys*, **4**: 184 – 193, (2022).

[11] D. Aasen, M. Hell, R. V. Mishmash, A. Higginbotham, J. Danon, M. Leijnse, T. S. Jespersen, J. A. Folk, C. M. Marcus, K. Flensberg, and J. Alicea. Milestones Toward Majorana-Based Quantum Computing. *Phys. Rev. X*, **6**: 031016, (2016).

[12] A. Kitaev. Unpaired Majorana fermions in quantum wires. *Physics-Uspekhi*, **44** (10S): 131 – 136, (2001).

[13] C. H. Li, O. M. Erve, J. T. Robinson, Y. Li, L. Li, and B. T. Jonker. Electrical detection of charge-current-induced spin polarization due to spin-momentum locking in Bi_2Se_3. *Nat Nanoech*, **9**: 218 – 224, (2014).

[14] C. H. Li, O. M. Erve, Y. Li, L. Li, and B. T. Jonker. Electrical Detection of the Helical Spin Texture in a p-type Topological Insulator Sb_2Te_3. *Sci Rep*, **6**: 29533, (2016).

[15] J. Tian, I. Miotkowski, S. Hong, and Y.P. Chen. Electrical injection and detection of spin-polarized currents in topological insulator Bi2Te2Se. *Sci Rep*, **5**: 14293, (2015).

[16] F. Yang, S. Ghatak, A. A. Taskin, K. Segawa, Y. Ando, M. Shiraishi, Y. Kanai, K. Matsumoto, A. Rosch, and Y. Ando. Switching of charge-current-induced spin polarization in the topological insulator $BiSbTeSe_2$. *Phys. Rev. B*, **94**: 075304, (2016).

[17] L. Zhao, H. Deng, I. Korzhovska, M. Begliarbekov, Z. Chen, E. Andrade, E. Rosenthal, A. Pasupathy, V. Oganesyan, and L. Krusin-Elbaum. Emergent surface superconductivity in the Topological Insulator Sb_2Te_3. *Nat. Comms.*, **6**: 8279, 2015.

[18] L. Plucinski, A. Herdt, S. Fahrendorf, G. Bihlmayer, G. Mussler, S. Döring, J. Kampmeier, F. Matthes, D. E. Bürgler, D. Grützmacher, S. Blügel, and C. M. Schneider. Electronic structure, surface morphology, and topologically protected surface states of Sb_2Te_3 thin films grown on Si(111). *J. Appl. Phys.*, **113**: 053706, 2013.

[19] C. Pauly, G. Bihlmayer, M. Liebmann, M. Grob, A. Georgi, D. Subramaniam, M. R. Scholz, J. Sanchez-Barriga, A. Varykhalov, S. Blugel, O. Rader, and M. Morgenstern. Probing two topological surface bands of Sb_2Te_3 by spin-polarized photoemission spectroscopy. *Phys. Rev. B*, **86**: 235106, 2012.

[20] C. Seibel, H. Bentmann, J. Braun, J. Minár, H. Maaß, K. Sakamoto, M. Arita, K. Shimada, H. Ebert, and F. Reinert. Connection of a Topological Surface State with the Bulk Continuum in Sb_2Te_3. *Phys. Rev. Lett.*, **114**: 066802, 2015.

[21] C. Seibel, H. Maaß, H. Bentmann, J. Braun, K. Sakamoto, M. Arita, K. Shimada, J. Minár, H. Ebert, and F. Reinert. The Rashba-split surface state of $Sb_2Te_3(0001)$ and its interaction with bulk states. *J. Electron. Spectros. Relat. Phenomena*, **201**: 110 – 114, (2015).

[22] S. Sasaki and T. Mizushima. Superconducting doped topological materials. *Physica C*, **514**: 206 – 217, 2015.

[23] M. Sato and Y. Ando. Topological Superconductors. *Rep. Prog. Phys.*, **80**: 076501, 2017.

[24] L. Fu and C.L. Kane. Superconducting proximity effect and Majorana fermions at the surface of a topological insulator. *Phys. Rev. Lett.*, **100**: 096407, 2008.

[25] V. Mourik, K. Zuo, S. M. Frolov, S. R. Plissard, E. P. A. M. Bakkers, and L. P. Kouwenhoven. Signatures of Majorana Fermions in Hybrid Superconductor-Semiconductor Nanowire Devices. *Science*, **336**(6084): 1003 – 1007, (2012).

[26] F. Pientka, A. Keselman, E. Berg, A. Yacoby, A. Stern, and B. I. Halperin. Topological Superconductivity in a Planar Josephson Junction. *Phys. Rev. X*, **7**: 021032, (2017).

[27] X. Zhang et al. Anomalous Josephson Effect in Topological Insulator-Based Josephson Trijunction. *Chinese Physics Letters*, **39**(1): 017401, (2022).

[28] Tong Zhou, Matthieu C. Dartiailh, William Mayer, Jong E. Han, Alex Matos-Abiague, Javad Shabani, and Igor Žutić. Phase Control of Majorana Bound States in a Topological X Junction. *Phys. Rev. Lett.*, **124**: 137001, (2020).

[29] M. Sakano, K. Okawa, M. Kanou, H. Sanjo, T. Okuda, T. Sasagawa, and K Ishizaka. Topologically protected surface states in a centrosymmetric superconductor β-PdBi2. *Nat. Comms.*, **6**: 8595, (2015).

[30] J. F. Zhang, P. J. Guo, M. Gao, K. Liu, and Z. Y. Lu. β-$RhPb_2$: A topological superconductor candidate. *Phys. Rev. B*, **99**: 045110, (2019).

[31] L.M. Schoop et al. Dirac metal to topological metal transition at a structural phase change in Au_2Pb and prediction of Z(2) topology for the superconductor. *Phys. Rev. B*, **91**: 214517, 2015.

[32] B. Bradlyn, L. Elcoro, J. Cano, M.G. Vergniory, Z. Wang, C. Felser, M.I. Aroyo, and B. Bernevig. Topological quantum chemistry. *Nature*, **547**: 298 – 305, 2017.

[33] F. Tang, H.C. Po, A. Vishwanath, and X. Wan. Comprehensive search for topological materials using symmetry indicators. *Nature*, **566**: 486 – 489, 2019.

[34] T. Zhang, Y. Jiang, Z. Song, H. Huang, Y. He, Z. Fang, H. Weng, and C. Fang. Catalogue of topological electronic materials. *Nature*, **566**: 475 – 479, 2019.

[35] M. G. Vergniory, L. Elcoro, C. Felser, N. Regnault, B. Bernevig, and Z. Wang. A complete catalogue of high-quality topological materials. *Nature*, **566**: 480 – 485, 2019.

[36] F. Tang, H.C. Po, A. Vishwanath, and X. Wan. Efficient topological materials discovery using symmetry indicators. *Nat. Phys.*, **15**: 470 – 476, 2019.

[37] M. M. Hirschmann, A. Leonhardt, B. Kilic, D. H. Fabini, and A. P. Schnyder. Symmetry-enforced band crossings in tetragonal materials: Dirac and Weyl degeneracies on points, lines, and planes. *Phys. Rev. Materials*, **5**: 054202, (2021).

[38] E.E. Havinga, H. Damsma, and J.M. Kanis. Compounds and pseudo-binary alloys with the CuAl2 (C16)-type structure IV. Superconductivity. *Journal of the Less Common Metals*, **27**(3): 281 – 291, (1972).

[39] M.F. Gendron and R.E. Jones. Superconductivity in the $CuAl_2$ (C16) crystal class. *J. Phys. Chem. Solids*, **23**: 405 – 406, 1962.

[40] S. Kobayashi and M. Sato. Topological Superconductivity in Dirac Semimetals. *Phys. Rev. Lett.*, **115**: 187001, (2015).

[41] T Mochiku et al. Redetermination of the crystal structure of $RhPb_2$ from single-crystal X-ray diffraction data, revealing a rhodium deficiency. *Acta Cryst. E*, **77** (12): 1327 – 1329, (2021).

[42] L. Fu and C.L. Kane. Topological Insulators with inversion symmetry. *Phys. Rev. B*, **76**:045302, 2007.

[43] L. Fu, C.L. Kane, and E.J. Mele. Topological Insulators in Three Dimensions. *Phys. Rev. Lett.*, **98**: 106803, 2007.

[44] Y. Ando. Topological Insulator materials. *J. Phys. Soc. Jpn*, **82**: 102001, 2013.

[45] D. J. Griffiths, *Introduction to Elementary Particles* (Harper & Row, New York, 1987), .

[46] S. G. Davison and M. Stęślicka, *Basic Theory of Surface States* (Clarendon Press, Oxford, 1992).

[47] N. W. Ashcroft and N. D. Mermin, *Solid State Physics* (Harcourt Inc., Orlando, 1976).

[48] C.X. Liu, X.L. Qi, H.J Zhang, X.Dai, Z. Fang, and S.C. Zhang. Model Hamiltonian for topological insulators. *Phys. Rev. B*, **82**: 045122, (2010).

[49] L. Fu and E. Berg. Odd-parity topological superconductors: theory and application to $Cu_xBi_2Se_3$. *Phys. Rev. Lett.*, **105**: 097001, 2010.

[50] A. H. Castro Neto, F. Guinea, N. M. R. Peres, K. S. Novoselov, and A. K. Geim. The electronic properties of graphene. *Rev. Mod. Phys.*, **81**: 109 – 162, (2009).

[51] V. Ariel and A. Natan. Electron effective mass in graphene. In *2013 International Conference on Electromagnetics in Advanced Applications (ICEAA)*, pages 696–698, 2013.

[52] S. LaShell, B. A. McDougall, and E. Jensen. Spin Splitting of an Au(111) Surface State Band Observed with Angle Resolved Photoelectron Spectroscopy. *Phys. Rev. Lett.*, **77**: 3419 – 3422, (1996).

[53] D. Hsieh et al. A tunable topological insulator in the spin helical Dirac transport regime. *Nature*, **460**: 1101 – 05, 2009.

[54] G.P. Mikitik and Y.V. Sharlai. Manifestation of Berry's Phase in Metal Physics. *Phys. Rev. Lett.*, **82**: 2147 – 2150, (1999).

[55] A.R. Wright and R.H. McKenzie. Quantum oscillations and Berry's phase in topological insulator surface states with broken particle-hole symmetry. *Phys. Rev. B*, **87**: 085411, (2013).

[56] A. A. Taskin and Y. Ando. Berry phase of nonideal Dirac fermions in topological insulators. *Phys. Rev. B*, **84**: 035301, (2011).

[57] N.P. Armitage, E.J. Mele, and A. Vishwanath. Weyl and Dirac semimetals in three-dimensional solids. *Rev. Mod. Phys.*, **90**: 015001, (2018).

[58] D. Hsieh et al. A topological Dirac insulator in a quantum spin Hall phase (first experimental realization of a 3D Topological Insulator). *Nature*, **452**: 970 – 974, 2008.

[59] D. Hsieh, Y. Xia, L. Wray, D. Qian, A. Pal, J. H. Dil, J. Osterwalder, F. Meier, G. Bihlmayer, C. L. Kane, Y. S. Hor, R. J. Cava, and M. Z. Hasan. Observation of Unconventional Quantum Spin Textures in Topological Insulators. *Science*, **323**(5916): 919 – 922, (2009).

[60] D. Hsieh et al. Observation of Time-Reversal-Protected Single-Dirac-Cone Topological-Insulator States in Bi_2Te_3 and Sb_2Te_3. *Phys. Rev. Lett.*, **103**: 146401, (2009).

[61] J. Zhang et al. Band structure engineering in $(Bi_{1-x}Sb_x)_2Te_3$ ternary topological insulators. *Nat. Comms.*, **2**: 574, 2011.

[62] C. Drasar, P. Lostak, and C. Uher. Doping and Defect Structure of Tetradymite-Type Crystals. *J. Electron. Mater.*, **39**: 2162, 2010.

[63] J.G. Analytis, J.H. Chu, Y. Chen, F. Corredor, R.D. McDonald, Z.X. Shen, and I.R. Fisher. Bulk Fermi surface coexistence with Dirac surface state in Bi_2Se_3: a comparison of photoemission and Shubnikov-de Haas measurements. *Phys. Rev. B*, **81**: 205407, (2010).

[64] K. Eto, Z. Ren, A.A. Taskin, K. Segawa, and Y. Ando. Angular-dependent oscillations of the magnetoresistance in Bi_2Se_3 due to the three-dimensional bulk Fermi surface. *Phys. Rev. B*, **81**: 195309, 2010.

[65] J.G. Analytis et al. Two-dimensional surface state in the quantum limit of a topological insulator. *Nat. Phys.*, **6**: 960 – 964, 2010.

[66] J.G. Checkelsky, Y.S. Hor, M.H. Liu, D.X. Qu, R.J. Cava, and N.P. Ong. Quantum Interference in Macroscopic Crystals of Nonmetallic Bi2Se3. *Phys. Rev. Lett.*, **103**: 246601, 2009.

[67] A.A. Taskin, Z. Ren, S. Sasaki, K. Segawa, and Y. Ando. Observation of Dirac Holes and Electrons in a Topological Insulator. *Phys. Rev. Lett.*, **107**: 016801, 2011.

[68] Y.S. Kim, M. Brahlek, N. Bansal, E. Edrey, G.A. Kapilevich, K. Iida, M. Tanimura, Y. Horibe, S.W. Cheong, and S. Oh. Thickness-dependent bulk properties and weak anti-localization effect in topological insulator Bi_2Se_3. *Phys. Rev. B*, **84**: 073109, 2011.

[69] A. A. Taskin and Y. Ando. Quantum oscillations in a topological insulator $Bi_{1-x}Sb_x$. *Phys. Rev. B*, **80**: 085303, (2009).

[70] A. A. Taskin, K. Segawa, and Y. Ando. Oscillatory angular dependence of the magnetoresistance in a topological insulator $Bi_{1-x}Sb_x$. *Phys. Rev. B*, **82**: 121302, (2010).

[71] A. A. Taskin, S. Sasaki, K. Segawa, and Y. Ando. Manifestation of Topological Protection in Transport Properties of Epitaxial Bi_2Se_3 Thin Films. *Phys. Rev. Lett.*, **109**: 066803, (2012).

[72] J. Chen, H. J. Qin, F. Yang, J. Liu, T. Guan, F. M. Qu, G. H. Zhang, J. R. Shi, X. C. Xie, C. L. Yang, K. H. Wu, Y. Q. Li, and L. Lu. Gate-Voltage Control of Chemical Potential and Weak Antilocalization in Bi_2Se_3. *Phys. Rev. Lett.*, **105**: 176602, (2010).

[73] G. Bergmann. Weak localization in thin films: a time-of-flight experiment with conduction electrons. *Physics Reports*, **107**(1): 1 – 58, (1984).

[74] G. Bergmann. Weak anti-localization - An experimental proof for the destructive interference of rotated spin-1/2. *Solid State Comms.*, **42**: 815 – 817, (1982).

[75] H.Z. Lu and S.Q. Shen. Weak localization and weak anti-localization in topological insulators. *Proc. SPIE 9167, Spintronics*, **VII**: 91672E, (2014).

[76] W.Y. Shan, H.Z. Lu, and S.Q. Shen. Spin-orbit scattering in quantum diffusion of massive dirac fermions. *Phys. Rev. B*, **86**: 125303, (2012).

[77] B. L. Altshuler, A.G. Aronov, A. I. Larkin, , and D. E. Klmel'nitskii. Anomalous magnetoresistance in semiconductors. *JETP*, **54**: 411, (1981).

[78] D. Shoenberg, *Magnetic Oscillations in Metals* (Cambridge University Press, Cambridge, 1984).

[79] I.A. Luk'yanchuk and Y. Kopelevich. Dirac and Normal Fermions in Graphite and Graphene: Implications of the Quantum Hall Effect. *Phys. Rev. Lett.*, **97**: 256801, (2006).

[80] M. Tinkham, *Introduction to Superconductivity* (Dover Publications Inc., New York, 2004).

[81] Y. Maeno et al. Evaluation of spin-triplet superconductivity in Sr_2RuO_4. *J. Phys. Soc. Jpn*, **81**: 011009, (2012).

[82] T.M. Rice and M. Sigrist. Sr_2RuO_4: an electronic analogue of 3He? *J. Phys.: Condens. Matter*, **7**(47): L643, (1995).

[83] A.P. Mackenzie and Y. Maeno. The superconductivity of Sr_2RuO_4 and the physics of spin-triplet pairing. *Reviews of Modern Physics*, **75**: 657 – 712, (2003).

[84] J.F. Annet. *Supercondcutivity, Superfluids and Condensates*, Oxford: Oxford University Press, 2004.

[85] R. Balian and N.R. Werthamer. Superconductivity with Pairs in a relative p wave. *Phys. Rev.*, **131**: 1553, 1963.

[86] K. Michaeli and L. Fu. Spin-Orbit Locking as a Protection Mechanism of the Odd-Parity Superconducting State against Disorder. *Phys. Rev. Lett.*, **109**: 187003, 2012.

[87] D. C. Cavanagh and P. M. R. Brydon. Robustness of unconventional s-wave superconducting states against disorder. *Phys. Rev. B*, **101**: 054509, (2020).

[88] D. J. Griffiths, *Introduction to Quantum Mechanics* (Pearson, New Jersey, 2005), .

[89] H. Wei, S. P. Chao, and V. Aji. Odd-parity superconductivity in Weyl semimetals. *Phys. Rev. B*, **89**: 014506, (2014).

[90] M. R. Norman. The Challenge of Unconventional Superconductivity. *Science*, **332**(6026): 196–200, 2011.

[91] A. P. Mackenzie, R. K. W. Haselwimmer, A. W. Tyler, G. G. Lonzarich, Y. Mori, S. Nishizaki, and Y. Maeno. Extremely Strong Dependence of Superconductivity on Disorder in Sr_2RuO_4. *Phys. Rev. Lett.*, **80**: 161 – 164, (1998).

[92] M. Sigrist and K. Ueda. Phenomenological theory of unconventional superconductivity. *Rev. Mod. Phys.*, **63**: 239 – 311, 1991.

[93] S. Kashiwaya and Y. Tanaka. Tunnelling effects on surface bound states in unconventional superconductors. *Rep. Prog. Phys*, **63**: 1641, (2000).

[94] S. Kashiwaya, Y. Tanaka, M. Koyanagi, and K. Kajimura. Theory for tunneling spectroscopy of anisotropic superconductors. *Phys. Rev. B*, **53**: 2667, 1996.

[95] H. Padamsee, J.E. Neighbor, and C.A. Shiffman. Quasiparticle phenomenology for thermodynamics of strong-coupling superconductors. *J. Low Temp Phys*, **12**, year = (1973),: 387 – 411.

[96] M. Kriener, K. Segawa, Z. Ren, S. Sasaki, and Y. Ando. Bulk Superconducting Phase with a Full Energy Gap in the Doped Topological Insulator $Cu_xBi_2Se_3$. *Phys. Rev. Lett.*, **106**: 127004, 2011.

[97] D. Das et al. Probing the superconducting gap structure in the noncentrosymmetric topological superconductor ZrRuAs. *Phys. Rev. B*, **103**: 144516, (2021).

[98] S. Sasaki, K. Segawa, and Y. Ando. Superconductor derived from a topological insulator heterostructure. *Phys. Rev. B*, **90**: 220504, (2014).

[99] A. Kolapo, T. Li, P. Hosur, and J.H. Miller Jr. Possible transport evidence for three-dimensional topological superconductivity in doped β-$PdBi_2$. *Sci. Rep.*, **9**: 12504, 2019.

[100] T. V. Bay, T. Naka, Y. K. Huang, H. Luigjes, M. S. Golden, and A. de Visser. Superconductivity in the Doped Topological Insulator $Cu_xBi_2Se_3$ under High Pressure. *Phys. Rev. Lett.*, **108**: 057001, 2012.

[101] K. Kirshenbaum, P. S. Syers, A. P. Hope, N. P. Butch, J. R. Jeffries, S. T. Weir, J. J. Hamlin, M. B. Maple, Y. K. Vohra, and J. Paglione. Pressure-Induced Unconventional Superconducting Phase in the Topological Insulator Bi_2Se_3. *Phys. Rev. Lett.*, **111**: 087001, 2013.

[102] H. Keller. Muon-spin rotation experiments in high-T_c superconductors and related materials. *IBM Journal of Research and Development*, **33**(3): 314 – 323, (1989).

[103] H. Leng, D. Cherian, Y. K. Huang, J.-C. Orain, A. Amato, and A. de Visser. Muon spin rotation study of the topological superconductor $Sr_xBi_2Se_3$. *Phys. Rev. B*, **97**: 054503, (2018).

[104] J. A. Krieger et al. Superconducting Properties of Cu Intercalated Bi_2Se_3 Studied by Muon Spin Spectroscopy. In *Proceedings of the 14th International Conference on Muon Spin Rotation, Relaxation and Resonance (μSR2017).*

[105] T. Hashimoto, K. Yada, A. Yamakage, M. Sato, and Y. Tanaka. Bulk Electronic State of Superconducting Topological Insulator. *J. Phys. Soc. Jpn*, **82**(4): 044704, (2013).

[106] T. Hashimoto, K. Yada, A. Yamakage, M. Sato, and Y. Tanaka. Effect of Fermi surface evolution on superconducting gap in superconducting topological insulator. *Superconductor Science and Technology*, **27**(10): 104002, (2014).

[107] Y. Nagai, H. Nakamura, and M. Machida. Rotational isotropy breaking as proof for spin-polarized Cooper pairs in the topological superconductor $Cu_xBi_2Se_3$. *Phys. Rev. B*, **86**: 094507, 2012.

[108] R. Tao, Y. Yan, X. Liu, Z. W. Wang, Y. Ando, Q. Wang, T. Zhang, and D. Feng. Direct Visualization of the Nematic Superconductivity in $Cu_xBi_2Se_3$. *Phys. Rev. X*, **8**: 041024, (2018).

[109] S. Yonezawa, K. Tajiri, S. Nakata, et al. Thermodynamic evidence for nematic superconductivity in $Cu_xBi_2Se_3$. *Nature Phys*, **13**: 123 – 126, (2017).

[110] N. R. Werthamer, E. Helfand, and P. C. Hohenberg. Temperature and Purity Dependence of the Superconducting Critical Field, H_{c2}. III. Electron Spin and Spin-Orbit Effects. *Phys. Rev.*, **147**: 295 – 302, (1966).

[111] N. Toyota, A. Inoue, T. Fukase, et al. Upper critical field and related properties of superconducting amorphous alloys Zr-Si. *J Low Temp Phys*, **55**: 393 – 410, (1984).

[112] T. P. Orlando, E. J. McNiff, S. Foner, and M. R. Beasley. Critical fields, Pauli paramagnetic limiting, and material parameters of Nb_3Sn and V_3Si. *Phys. Rev. B*, **19**: 4545 – 4561, 1979.

[113] L. J. Neuringer and Y. Shapira. Effect of Spin-Orbit Scattering on the Upper Critical Field of High-Field Superconductors. *Phys. Rev. Lett.*, **17**: 81 – 84, (1966).

[114] K. Scharnberg and R. A. Klemm. p-wave superconductors in magnetic fields. *Phys. Rev. B*, **22**: 5233 – 5244, (1980).

[115] S. Sasaki, M. Kriener, K. Segawa, K. Yada, Y. Tanaka, M. Sato, and Y. Ando. Topological Superconductivity in $Cu_xBi_2Se_3$. *Phys. Rev. Lett.*, **107**: 217001, 2011.

[116] S. Sasaki, Z. Ren, A.A. Taskin, K. Segawa, L. Fu, and Y. Ando. Odd-Parity Pairing and Topological Superconductivity in a Strongly Spin-Orbit Coupled Semiconductor. *Phys. Rev. Lett.*, **109**: 217004, 2012.

[117] H. Zhang, C. Liu, S. Gazibegovic, et al. Retraction Note: Quantized Majorana conductance. *Nature*, **591**: E30, (2021).

[118] A. Yamakage et al. Anomalous Josephson current in superconducting topological insulator. *Phys. Rev. B*, **87**: 100510, 2013.

[119] L.P. Rokhinson, X. Liu, and J.K. Furdyna. The fractional a.c. Josephson effect in a semiconductor-superconductor nanowire as a signature of Majorana particles. *Nature Physics*, **8**: 795 – 799, (2012).

[120] Bouman D. van Woerkom D.J. et al. Laroche, D. Observation of the 4π-periodic Josephson effect in indium arsenide nanowires. *Nat Commun*, **10**: 245, (2019).

[121] A. Mzerd et al. Effect of Heat Treatment on Some of the Electrical Properties of Sb_2Te_3 Single Crystals Grown by the Bridgman Method. *Physica Status Solidi a*, **141**: 183 – 90, 1994.

[122] M.P. Deshpande, N.N. Pandya, and M.N. Parmar. Transport property measurements of Bi_2Se_3 crystal grown by Bridgman method. *Turkish Journal of Physics*, **33**: 139 – 148, 2009.

[123] P.W. Bridgman. Certain Physical Properties of Single Crystals of Tungsten, Antimony, Bismuth, Tellurium, Cadmium, Zinc, and Tin. *Proceedings of the American Academy of Arts and Sciences*, **60**(6): 305 – 83, 1925.

[124] D. Depla and S. Mahieu and J. E. Greene, "Sputter deposition processes", in *Handbook of deposition technologies for films and coatings: science, applications and technology*, edited by P.M. Martin (William Andrew, Oxford, 2010).

[125] M. Ohring *Materials Science of Thin Films* (Harcourt Inc., San Diego, 2002).

[126] Potenza, A. (2006) *Structural, Electronic and Magnetic Properties of Superconductor/Ferromagnet Multilayers*. PhD thesis, University of Leeds.

[127] J. Daliant and A. Gibaud, *X-ray and Neutron Reflectivity: Principles and Applications* (Springer, Berlin, 2009).

[128] J. W. Ekin, *Experimental Techniques for Low Temperature Measurements* (Oxford University Press, Oxford).

[129] Batley, J. T. (2015) *Spin Transport in Lateral Spin Valves*. PhD thesis, University of Leeds.

[130] Vaughan, M. T. (2020) *Thin Films Containing Heavy Group V Elements as Systems for Topological Materials*. PhD thesis, University of Leeds.

[131] R. Drabble and R. Wolfe. Anisotropic Galvanomagnetic Effects in Semiconductors. *Proc. Phys. Soc. B*, **69**: 1101, 1956.

[132] L.J. Van der Pauw. A Method of Measuring the Resistivity and Hall Coefficient on Lamellae of Arbitrary Shape. *Philips Technical Review*, **20**: 220 – 224, 1958.

[133] F.S. Oliveira, R.B. Cipriano, F.T. da Silva, E.C. Romao, and C.A.M. dos Santos. Simple analytical method for determining electrical resistivity and sheet resistance using the Van der Pauw procedure. *Sci. Rep.*, **10**: 16379, (2020).

[134] A. B. Pippard, *Magnetoresistance in Metals* (Cambridge University Press, Cambridge, 1989).

[135] C. Kittel, *Introduction to Solid State Physics* (John Wiley & Sons Inc., New York, 1996).

[136] S. Zhang, Q. Wu, Y. Liu, and O. V. Yazyev. Magnetoresistance from Fermi surface topology. *Phys. Rev. B*, **99**: 035142, 2019.

[137] E.N. Adams and T.D. Holstein. Quantum theory of transverse galvano-magnetic phenomena. *J. Phys. Chem. Solids*, **10**(4): 254 – 276, (1959).

[138] P.N. Argyres. Quantum Theory of Transport in a Magnetic Field. *Phys. Rev.*, **117**: 315 – 328, (1960).

[139] S. Das Sarma and F. Stern. Single-particle relaxation time versus scattering time in an impure electron gas. *Phys. Rev. B*, **32**: 8442–8444, 1985.

[140] A Isihara and L Smrcka. Density and magnetic field dependences of the conductivity of two-dimensional electron systems. *Journal of Physics C: Solid State Physics*, **19**(34): 6777–6789, (1986).

[141] J.A. Woollam. Graphite Carrier Locations and Quantum Transport to 10 T (100 kG). *Phys. Rev. B*, **3**: 1148 – 1159, (1971).

[142] J. Xiong, Y. Luo, Y.H. Khoo, S. Jia, R.J. Cava, and N.P. Ong. High-field Shubnikov–de Haas oscillations in the topological insulator Bi_2Te_2Se. *Phys. Rev. B*, **86**: 045314, 2012.

[143] P. Sessi, O. Storz, T. Bathon, S. Wilfert, K. A. Kokh, O. E. Tereshchenko, G. Bihlmayer, and M. Bode. Scattering properties of the three-dimensional topological insulator Sb_2Te_3: coexistence of topologically trivial and nontrivial surface states with opposite spin-momentum helicity. *Phys. Rev. B*, **93**: 035110, 2016.

[144] P. D. C. King, R. C. Hatch, M. Bianchi, R. Ovsyannikov, C. Lupulescu, G. Landolt, B. Slomski, J. H. Dil, D. Guan, J. L. Mi, E. D. L. Rienks, J. Fink, A. Lindblad, S. Svensson, S. Bao, G. Balakrishnan, B. B. Iversen, J. Osterwalder, W. Eberhardt, F. Baumberger, and Ph. Hofmann. Large Tunable Rashba Spin Splitting of a Two-Dimensional Electron Gas in Bi_2Se_3. *Phys. Rev. Lett.*, **107**: 096802, 2011.

[145] G. Engels, J. Lange, Th. Schäpers, and H. Lüth. Experimental and theoretical approach to spin splitting in modulation-doped $In_xGa_{1-x}As$/InP quantum wells for B→0. *Phys. Rev. B*, **55**: R1958 – R1961, (1997).

[146] J. Nitta, T.i Akazaki, H. Takayanagi, and T. Enoki. Gate Control of Spin-Orbit Interaction in an Inverted $In_{0.53}Ga_{0.47}As/In_{0.52}Al_{0.48}As$ Heterostructure. *Phys. Rev. Lett.*, **78**: 1335 – 1338, (1997).

[147] D. Grundler. Large Rashba Splitting in InAs Quantum Wells due to Electron Wave Function Penetration into the Barrier Layers. *Phys. Rev. Lett.*, **84**: 6074 – 6077, 2000.

[148] Quantum materials for spin and charge conversion. *npj Quantum Mater.*, **3**(1): 27, 2018.

[149] A Manchon, H C Koo, J Nitta, S M Frolov, and R A Duine. New perspectives for Rashba spin-orbit coupling. *Nat. Mater.*, **14**(9): 871 – 882, (2015).

[150] P. Gambardella and I. M. Miron. Current-induced spin-orbit torques. *Philos. Trans. Royal Soc. A*, **369**: 3175 – 3197, (2011).

[151] S. Hong, V. Diep, S. Datta, and Y. P. Chen. Modeling potentiometric measurements in topological insulators including parallel channels. *Phys. Rev. B*, **86**: 085131, (2012).

[152] A. von Middendorff, K. Dietrich, and G. Landwehr. Shubnikov de Haas effect in p-type Sb_2Te_3. *Solid State Commun.*, **13**: 443 – 446, 1973.

[153] V.A. Kulbachinskii, N. Miura, H. Nakagawa, C. Drashar, and P. Lostak. Influence of Ti doping on galvanomagnetic properties and valence band energy spectrum of $Sb_{2-x}Ti_xTe_3$ single crystals. *J. Phys.: Condens. Matter*, **11**: 5273, 1999.

[154] J. Horak, M. Matyas, and L. Tichy. Lattice Defects in Manganese-Doped Sb_2Te_3 Crystals. *Phys. Stat. Sol*, **27**: 621, 1975.

[155] J. Horak, P. Lostak, C. Drasar, J.S. Dyck, Z. Zhou, and C. Uher. Defect structure of $Sb_{2-x}Mn_xTe_3$ single crystals. *J. Solid State Chem.*, **178**(9): 2907 – 2912, (2005).

[156] J. Horak, P.C. Quayle, J.S. Dyck, C. Drasar, P. Lostak, and C. Uher. Defect structure of $Sb_{2-x}Cr_xTe_3$ single crystals. *J. Appl. Phys.*, **103**: 013516, 2008.

[157] J. Horak, P. Lostak, and M. Matyas. Point Defects in Sn-Doped Sb_2Te_3 Single Crystals. *Phys. Stat. Sol. (b)*, **129**: 381, 1985.

[158] Y. Jiang et al. Fermi-Level Tuning of Epitaxial Sb_2Te_3 Thin Films on Graphene by Regulating Intrinsic Defects and Substrate Transfer Doping. *Phys. Rev. Lett.*, **108**: 066809, 2012.

[159] T. L. Anderson and H. B. Krause. Refinement of the Sb_2Te_3 and Sb_2Te_2Se structures and their relationship to nonstoichiometric $Sb_2Te_{3-y}Se_y$ compounds. *Acta Cryst.*, **B30**: 1307 – 1310, (1974).

[160] N.Sakai, T.Kajiwara, K.Takemura, S.Minomura, and Y.Fujii. Pressure-induced phase transition in Sb_2Te_3. *Solid State Comms.*, **40**(12): 1045 – 1047, (1981).

[161] S V Eremeev, M G Vergniory, T V Menshchikova, A A Shaposhnikov, and E V Chulkov. The effect of van der Waal's gap expansions on the surface electronic structure of layered topological insulators. *New J. Phys.*, **14**: 113030, (2012).

[162] X. Zhang, Z. Zeng, C. Shen, Z. Zhang, Z. Wang, C. Lin, and Z. Hu. Investigation on the electrical transport properties of highly (00l)-textured Sb_2Te_3 films deposited by molecular beam epitaxy. *Journal of Applied Physics*, **115**: 024307, (2014).

[163] C R M Grovenor. Grain boundaries in semiconductors. *J. Phys. C: Solid State Phys.*, **18**: 4079, (1985).

[164] Q. Yuan, Q. Nie, and D. Huo. Preparation and characterization of the antimony telluride hexagonal nanoplates. *Current Applied Physics*, **9**: 224 – 226, (2009).

[165] D. Das et al. Defect induced structural and thermoelectric properties of Sb_2Te_3 alloy. *Journal of Applied Physics*, **118**: 045102, (2015).

[166] Y. Takagaki, A. Giussani, K. Perumal, R. Calarco, and K.J. Friedland. Robust topological surface states in Sb_2Te_3 layers as seen from the weak antilocalization effect. *Phys. Rev. B*, **86**: 125137, 2012.

[167] C. Weyrich and T. Merzenich and J. Kampmeier and I. E. Batov and G. Mussler and J. Schubert and D. Grützmacher and T. Schäpers. Magnetoresistance oscillations in MBE-grown Sb_2Te_3 thin films. *Appl. Phys. Lett.*, **110**: 092104, 2017.

[168] Z. Ren, A.A. Taskin, S. Sasaki, K. Segawa, and Y. Ando. Large bulk resistivity and surface quantum oscillations in the topological insulator Bi_2Te_2Se. *Phys. Rev. B*, **82**: 241306, 2010.

[169] R. Singha, A. Pariari, B. Satpati, and P. Mandal. Large nonsaturating magnetoresistance and signature of non-degenerate Dirac nodes in ZrSiS. *Proc. Natl. Acad. Sci. U.S.A*, **114**: 2468, 2017.

[170] V.A. Kulbachinskii, Z. M. Dashevskii, M. Inoue, M. Sasaki, H. Negishi, W. X. Gao, P. Lostak, J. Horak, and A. de Visser. Valence band changes in $Sb_{2-x}In_xTe_3$ and $Sb_2In_yTe_{3-y}$ by transport and Shubnikov-de Haas effect measurements. *Phys. Rev. B*, **52**: 10915, 1995.

[171] F.X. Xiang, M. Veldhorst, S.X. Dou, and X.L. Wang. Multiple Fermi pockets revealed by Shubnikov-de Haas oscillations in WTe_2. *EPL*, **112**: 37009, (2015).

[172] J. Jiang, F. Tang, X. C. Pan, H. M. Liu, X. H. Niu, Y. X. Wang, D. F. Xu, H. F. Yang, B. P. Xie, F. Q. Song, P. Dudin, T. K. Kim, M. Hoesch, P. Kumar Das, I. Vobornik, X. G. Wan, and D. L. Feng. Signature of Strong Spin-Orbital Coupling in the Large Nonsaturating Magnetoresistance Material WTe_2. *Phys. Rev. Lett.*, 115:166601, 2015.

[173] D.Bercioux and P. Lucignano. Quantum transport in Rashba spin-orbit materials: a review. *Rep. Prog. Phys*, **78**(10): 106001, 2015.

[174] A. K. Okazaki, S. Wiedmann, S. Pezzini, M. L. Peres, P. H. O. Rappl, and E. Abramof. Shubnikov–de Haas oscillations in topological crystalline insulator SnTe(111) epitaxial films. *Phys. Rev. B*, **98**: 195136, (2018).

[175] L.M. Roth and P.N. Argyres, in *Semiconductors and Semimetals*, edited by R. K. Williardson and A. C. Beer (Academic Press, New York, 1966).

[176] F. Arnold et al. Quasi-two-dimensional Fermi surface topography of the delafossite $PdRhO_2$. *Phys. Rev. B*, **96**: 075163, 2017.

[177] F. Arnold, A. Isidori, E. Kampert, B. Yager, M. Eschrig, and J. Saunders. Charge Density Waves in Graphite: Towards the Magnetic Ultraquantum Limit. *Phys. Rev. Lett.*, **119**: 136601, 2017.

[178] H. Murakawa, M. S. Bahramy, M. Tokunaga, Y. Kohama, C. Bell, Y. Kaneko, N. Nagaosa, H. Y. Hwang, and Y. Tokura. Detection of Berry's Phase in a Bulk Rashba Semiconductor. *Science*, **342**(6165): 1490–1493, 2013.

[179] S.Q. Shen. Spin Hall effect and Berry phase in two-dimensional electron gas. *Phys. Rev. B*, **70**: 081311, (2004).

[180] M.C. Chang. Effect of in-plane magnetic field on the spin Hall effect in a Rashba-Dresselhaus system. *Phys. Rev. B*, 71:085315, 2005.

[181] I.A. Luk'yanchuk and Y. Kopelevich. Phase Analysis of Quantum Oscillations in Graphite. *Phys. Rev. Lett.*, 93:166402, 2004.

[182] D. P. A. Holgado, K. Bolanos, S. de Castro, H.S.A. Monteiro, F.S. Pena, A.K. Okazaki, C.I. Fornari, P.H.O. Rappl, E. Abramof, D.A.W. Soares, and M.L. Peres. Shubnikov-de Haas oscillations and Rashba splitting in Bi_2Te_3 epitaxial film. *Appl. Phys. Lett.*, 117(10):102108, 2020.

[183] S. Li, Z.M. Yu, Y. Yao, and S.A. Yang. Type-II topological metals. *Front. Phys.*, **15**: 43201, (2020).

[184] H. Huang, S. Zhou, and W. Duan. Type-II Dirac fermions in the $\mathbf{PtSe_2}$ class of transition metal dichalcogenides. *Phys. Rev. B*, **94**: 121117, (2016).

[185] T. R. Chang et al. Type-II Symmetry-Protected Topological Dirac Semimetals. *Phys. Rev. Lett.*, **119**: 026404, (2017).

[186] Amit, R. K. Singh, N. Wadehra, S. Chakraverty, and Y. Singh. Type-II Dirac semimetal candidates $A\mathrm{Te}_2$ (A = Pt, Pd): A de Haas-van Alphen study. *Phys. Rev. Materials*, 2:114202, 2018.

[187] L. An, X. Zhu, Y. Qian, C. Xi, W. Ning, H. Weng, and M. Tian. Signature of Dirac semimetal states in gray arsenic studied by de Haas–van Alphen and Shubnikov–de Haas quantum oscillations. *Phys. Rev. B*, **101**: 205109, (2020).

[188] Y. Jiang et al. Landau Quantization and the Thickness Limit of Topological Insulator Thin Films of Sb_2Te_3. *Phys. Rev. Lett.*, **108**: 016401, 2012.

[189] S. Perraud, K. Kanisawa, Z. Z. Wang, and T. Fujisawa. Direct Measurement of the Binding Energy and Bohr Radius of a Single Hydrogenic Defect in a Semiconductor Quantum Well. *Phys. Rev. Lett.*, **100**: 056806, (2008).

[190] B. I. Shklovskii and A. L. Efros, *Electronic Properties of Doped Semiconductors* (Springer-Verlag, Berlin, 1984).

[191] S. Liu, H. D. Drew, A. Illiades, and S. Hadjipanteli. Shubnikov–de Haas effect in a metallic impurity band. *Phys. Rev. B*, 45:1155–1158, 1992.

[192] T. Jungwirth, Jairo Sinova, A. H. MacDonald, B. L. Gallagher, V. Novák, K. W. Edmonds, A. W. Rushforth, R. P. Campion, C. T. Foxon, L. Eaves, E. Olejník, J. Mašek, S.-R. Eric Yang, J. Wunderlich, C. Gould, L. W. Molenkamp, T. Dietl, and H. Ohno. Character of states near the Fermi level in (Ga,Mn)As: Impurity to valence band crossover. *Phys. Rev. B*, 76:125206, 2007.

[193] L. Fu and C. L. Kane. Topological insulators with inversion symmetry. *Phys. Rev. B*, **76**: 045302, 2007.

[194] A. Jain et al. The Materials Project: A materials genome approach to accelerating materials innovation. *APL Materials*, **1**(1): 011002, (2013).

[195] E.E. Havinga, H. Damsma, and P. Hokkeling. Compounds and pseudo-binary alloys with the CuAl2(C16)-type structure I. Preparation and X-ray results. *Journal of the Less Common Metals*, **27+**, year = (1972),(2):169 – 186.

[196] Y. Li et al. Large spin to charge conversion in the topological superconductor $\beta-PdBi_2$ at room temperature. *Phys. Rev. B*, **102**: 014420, (2020).

[197] H. Okamoto. The Bi-Pd (Bismuth-Palladium) System. *JPE*, 15:191 – 194, 1994.

[198] S. Das, Amit, A. Sirohi, L. Yadav, S. Gayen, Y. Singh, and G. Sheet. Conventional superconductivity in the type-II Dirac semimetal $PdTe_2$. *Phys. Rev. B*, **97**: 014523, (2018).

[199] Amit and Y. Singh. Heat capacity evidence for conventional superconductivity in the type-II Dirac semimetal $PdTe_2$. *Phys. Rev. B*, **97**: 054515, (2018).

[200] Y. Li et al. Nontrivial superconductivity in topological $MoTe_{2-x}S_x$ crystals. *Proc. Natl. Acad. Sci. U.S.A*, **115**(38): 9503–9508, (2018).

[201] Arushi, K. Motla, A. Kataria, S. Sharma, J. Beare, M. Pula, M. Nugent, G. M. Luke, and R. P. Singh. Type-I superconductivity in single-crystal Pb_2Pd. *Phys. Rev. B*, **103**: 184506, (2021).

[202] Y. J. Uemura, V. J. Emery, A. R. Moodenbaugh, M. Suenaga, D. C. Johnston, A. J. Jacobson, J. T. Lewandowski, J. H. Brewer, R. F. Kiefl, S. R. Kreitzman, G. M. Luke, T. Riseman, C. E. Stronach, W. J. Kossler, J. R. Kempton, X. H. Yu, D. Opie, and H. E. Schone. Systematic variation of magnetic-field penetration depth in high-T_c superconductors studied by muon-spin relaxation. *Phys. Rev. B*, 38:909–912, 1988.

[203] Y. J. Uemura, G. M. Luke, B. J. Sternlieb, J. H. Brewer, J. F. Carolan, W. N. Hardy, R. Kadono, J. R. Kempton, R. F. Kiefl, S. R. Kreitzman, P. Mulhern, T. M. Riseman, D. Ll. Williams, B. X. Yang, S. Uchida, H. Takagi, J. Gopalakrishnan, A. W. Sleight, M. A. Subramanian, C. L. Chien, M. Z. Cieplak, Gang Xiao, V. Y. Lee, B. W. Statt, C. E. Stronach, W. J. Kossler, and X. H. Yu. Universal Correlations between T_c and $\frac{n_s}{m^*}$ (Carrier Density over Effective Mass) in High-T_c Cuprate Superconductors. *Phys. Rev. Lett.*, 62:2317–2320, 1989.

[204] Y. J. Uemura, L. P. Le, G. M. Luke, B. J. Sternlieb, W. D. Wu, J. H. Brewer, T. M. Riseman, C. L. Seaman, M. B. Maple, M. Ishikawa, D. G. Hinks, J. D. Jorgensen, G. Saito, and H. Yamochi. Basic similarities among cuprate, bismuthate, organic, Chevrel-phase, and heavy-fermion superconductors shown by penetration-depth measurements. *Phys. Rev. Lett.*, 66:2665–2668, 1991.

[205] M. G. Vergniory et al. All topological bands of all nonmagnetic stoichiometric materials. *Science*, **376**(6595): eabg9094, (2022).

[206] Max Planck Institute. (2019, Febuary 27). *Topological Material Database*. Retrieved from https://topologicalquantumchemistry.org.

[207] J. L. Jorda L. Schellenberg and J. Muller. The Rhodium-Silicon Phase Diagram. *Journal of the Less-Common Metals*, 109:261 – 274, 1985.

[208] A. A. Nayeb-Hashemi and J. Brian Clark. The Mgâ^'Pb (Magnesium-Lead) system. *Bulletin of Alloy Phase Diagrams*, 6:56–66, 1985.

[209] H. Okamoto. Pb-Zr (Lead-Zirconium). *Journal of Phase Equilibria and Diffusion*, 32:568 – 569, 2011.

[210] V. G. Khoruzhaya, K. E. Kornienko, P. S. Martsenyuk, and T. Ya. Velikanova. Phase equilibria in the system Al-Rh. *Powder Metallurgy and Metal Ceramics*, 45:251 – 258, 2006.

[211] H. Okamoto, *Pb (Lead) Binary Alloy Phase Diagrams* (ASM International, Ohio, 1988).

[212] S. P. Ong, L. Wang, B. Kang, and G. Ceder. Li-Fe-P-O2 Phase Diagram from First Principles Calculations. *Chemistry of Materials*, **20**(5): 1798 – 1807, (2008).

[213] A. Jain et al. Formation enthalpies by mixing GGA and GGA + U calculations. *Physical Review B*, **84**(4): 045115, (2011).

[214] A. J. Drew, M. W. Wisemayer, D. O. G. Heron, S. Lister, S. L. Lee, A. Potenza, C. H. Marrows, R. M. Dalgliesh, T. R. Charlton, and S. Langridge. Using spin-polarized neutron reflectivity to probe mesoscopic vortex states in a Pb thin-film superconductor. *Phys. Rev. B*, 80:134510, 2009.

[215] H. P. Klug. A redetermination of the lattice constant of lead. *J. Am. Chem. Soc.*, **68**: 1493, (1946).

[216] H. P. Singh. Determination of thermal expansion of germanium, rhodium and iridium by X-rays. *Acta Crystallogr.*, **24A**(a): 469, (1968).

[217] Y Ivry et al. Universal scaling of the critical temperature for thin films near the superconducting-to-insulating transition. *Phys. Rev. B*, **90**: 214515, Dec (2014).

[218] M. S. M. Minhaj, S. Meepagala, J. T. Chen, and L. E. Wenger. Thickness dependence on the superconducting properties of thin Nb films. *Phys. Rev. B*, 49:15235–15240, 1994.

[219] B. Abeles, Roger W. Cohen, and G. W. Cullen. Enhancement of superconductivity in metal films. *Phys. Rev. Lett.*, 17:632–634, 1966.

[220] J. Noffsinger and M. L. Cohen. Superconductivity in monolayer Pb on Si(111) from first principles. *Solid State Communications*, **151**(6): 421–424, (2011).

[221] T. Zhang, P. Cheng, W.J. Li, Y.J. Sun, G. Wang, X.G. Zhu, K. He, L. Wang, X. Ma, X. Chen, Y. Wang, Y. Liu, H.Q. Lin, J.F. Jia, and Q.K. Xue. Superconductivity in one-atomic-layer metal films grown on Si(111). *Nat. Phys.*, 6: 104 – 108, 2010.

[222] S. Dutta et al. Thickness dependence of the resistivity of platinum-group metal thin films. *Journal of Applied Physics*, 122(2):025107, 2017. doi: 10.1063/1.4992089.

[223] S. Park, J. Shin, and E. Kim. Scaling analysis of field-tuned superconductor-insulator transition in two-dimensional tantalum thin films. *Scientific Reports*, 7: 42969, 2017.

[224] M. T. Janish, W. M. Mook, and C. B. Carter. Nucleation of fcc Ta when heating thin films. *Scripta Materialia*, **96**: 21 – 24, (2015).

[225] L. Marot, G. De Temmerman, V. Thommen, D. Mathys, and P. Oelhafen. Characterization of magnetron sputtered rhodium films for reflective coatings. *Surface and Coatings Technology*, 202(13):2837–2843, 2008.

[226] Y. Xu, M. Yamazaki, and P. Villars. Inorganic Materials Database for Exploring the Nature of Material. *Jpn. J. Appl. Phys.*, **50**: 11RH02, (2011).

[227] M. Gurvitch. Universal disorder-induced transition in the resistivity behavior of strongly coupled metals. *Phys. Rev. Lett.*, 56:647–650, 1986.

[228] A. H. Wilson and R. H. Howard. The electrical conductivity of the transition metals. *Proceedings of the Royal Society of London. Series A. Mathematical and Physical Sciences*, 167(931):580 – 593, 1938. doi: 10.1098/rspa.1938.0156.

[229] G.K White and S.B. Woods. Electrical and Thermal Resistivity of the Transition Elements at Low Temperatures. *Philos. Trans. R. Soc A*, **251**(995): 273 – 302, (1959).

[230] Z. Ren, L. Gamperle, A. Fete, C. Senatore, and D. Jaccard. Evolution of T^2 resistivity and superconductivity in Nb_3Sn under pressure. *Phys. Rev. B*, 95: 184503, 2017.

[231] X. Lin, B. Fauqué, and K. Behnia. Scalable T^2 resistivity in a small single-component Fermi surface. *Science*, **349**(6251): 945 – 948, (2015).

[232] C.Y. Allison, C.B. Finch, M.D. Foegelle, and F.A. Modine. Low-temperature electrical resistivity of transition-metal carbides. *Solid State Communications*, 68 (4):387–390, 1988.

[233] P. B. Allen, "Boltzmann Theory and Resistivity of Metals," in *Quantum Theory of Real Materials*, edited by J. R. Chelikowsky and S. G. Louie (Kluwer, Boston, 1996), .

[234] P. B. Allen, "Electron-Phonon Coupling Constants", in *Handbook of Superconductivity*, edited by C.P. Poole Jr. (Academic Press, San Diego, 2000), .

[235] G. Grimvall, *The Electron - Phonon Interaction in Metals* (Oxford - North Holland, Amsterdam, 1981), .

[236] O. Gunnarsson, M. Calandra, and J. E. Han. Colloquium: Saturation of electrical resistivity. *Rev. Mod. Phys.*, 75:1085–1099, 2003.

[237] P. B. Allen. Metals with small electron mean-free path: saturation versus escalation of resistivity. *Physica B: Condensed Matter*, **318**(1): 24 – 27, (2002). The Future of Materials Physics: A Festschrift for Zachary Fisk.

[238] B.L. Brandt, R.D. Parks, and R.D. Chaudhari. Intermediate state of thin superconductors. *J Low Temp Phys*, 4:41 – 63, 1971.

[239] C. S. L. Chun, G. G. Zheng, J. L. Vincent, and I. K. Schuller. Dimensional crossover in superlattice superconductors. *Phys. Rev. B*, **29**: 4915–4920, (1984).

[240] Y. Fang et al. Unconventional superconductivity in $Cu_xBi_2Se_3$ from magnetic susceptibility and electrical transport. *New J. Phys.*, **22**: 053026, (2020).

[241] Ch. Buchal, F. Pobell, R. M. Mueller, M. Kubota, and J. R. Owers-Bradley. Superconductivity of Rhodium at Ultralow Temperatures. *Phys. Rev. Lett.*, 50: 64–67, 1983.

[242] B. T. Matthias, T. H. Geballe, and V. B. Compton. Superconductivity. *Rev. Mod. Phys.*, 35:1–22, 1963.

[243] J. Eisenstein. Superconducting Elements. *Rev. Mod. Phys.*, 26:277–291, 1954.

[244] S. Qin, J. Kim, Q. Niu, and C.K. Shih. Superconductivity at the Two-Dimensional Limit. *Science*, 324(5932):1314–1317, 2009.

[245] G. Gruner and A. Zawadowski. Magnetic impurities in non-magnetic metals. *Rep. Prog. Phys.*, **37**: 1497, (1974).

[246] M. T. Béal-Monod and R.A. Weiner. Negative Magnetoresistivity in Dilute Alloys. *Phys. Rev.*, **170**: 552 – 559, (1968).

[247] J.E. Hirsch and F. Marsiglio. Unusual width of the superconducting transition in a hydride. *Nature*, **596**: E9 – E10, (2021).

[248] P.W. Anderson. Theory of dirty superconductors. *J. Phys. Chem. Solids*, **11**: 26 – 30, 1959.

[249] A. V. Balatsky, I. Vekhter, and Jian-Xin Zhu. Impurity-induced states in conventional and unconventional superconductors. *Rev. Mod. Phys.*, 78:373–433, May 2006.

[250] J. P. Carbotte. Properties of boson-exchange superconductors. *Rev. Mod. Phys.*, 62:1027–1157, 1990.

[251] W. L. McMillan. Transition Temperature of Strong-Coupled Superconductors. *Phys. Rev.*, 167:331–344, 1968.

[252] Quantum Deisgn *Heat Capacity and Helium-3 Application Notes* (Quantum Deisgn, San Diego, 2019).